Doklady Physics, Vol. 49, No. 8, 2004, pp. 441–446. Translated from Doklady Akademii Nauk, Vol. 397, No. 4, 2004, pp. 467–473.

PHYSICS

Mechanism of the Electric Charging of Soot Particles upon the Combustion of Hydrocarbon Fuels

A. M. Savel'ev, A. M. Starik*, N. S. Titova, and Academician O. N. Favorskiĭ

Received March 18, 2004

INTRODUCTION

Mechanisms of the formation of various nanoparticles, as well as their structure and properties, have attracted considerable attention in recent years. Soot particles formed upon the combustion or pyrolysis of various hydrocarbon fuels are typical representatives of such particles. Their emission into the atmosphere changes both the radiation balance and climate of the Earth [1]. They are very important for the formation of vapor trails behind aircrafts [2].

The adsorption properties, capability to form cloud condensation nuclei, and clusterization of nanoparticles, as well as their optical properties and morphology of aggregates formed due to the coagulation of these particles, considerably depend on the presence of charge on them [3–6]. However, it was thought until recently that soot particles formed upon the combustion or pyrolysis of hydrocarbons are neutral, which follows from the commonly accepted hypothesis of the formation of soot particles in flames from neutral polyene molecules or polyaromatic hydrocarbons [7].

Calcote and Keil [8] hypothesized that positively charged soot particles are formed by clustering heavy hydrocarbon ions. However, recent experimental data obtained in propane diffusion flame show that the combustion of hydrocarbons in air is accompanied by the formation of particles charged both positively and negatively up to ten elementary charges, as well as neutral particles [5]. Neither the ion hypothesis of the formation of soot particles nor the polyaromatic or polyene model of their formation can explain this fact. As will be shown below, this fact is explained by the interaction of ions, which are formed in the high-temperature flame zone, with soot particles.

KINETICS OF THE INTERACTION BETWEEN IONS AND SOOT PARTICLES

Recent measurements [6] showed that soot produced in the combustion chambers of jet engines has large conductivity close to the conductivity of semiconductors and even metals. Conducting particles are polarized in an electric field created by an ion. In this case, polarization interaction must be taken into account in addition to Coulomb interaction [9]. Since ions produced upon the combustion of hydrocarbon fuels have unit charge [10], the potential of the interaction between the ion and a soot particle has the form

$$\varphi(r) = \frac{Pe^2}{r} - \frac{e^2a^3}{2r^2(r^2-a^2)}. \quad (1)$$

Here, P is the product of the charges of the ion and particle, r is the distance between the ion and soot particle, e is the elementary charge, and a is the radius of the soot particle. The fundamental difference of the interaction described by potential (1) from Coulomb interaction is that the soot particle can capture the ion at distances $r_\Delta > a$. This distance is usually called the capture sphere radius. If the ion approaches the soot particle at a distance smaller than r_Δ, its trajectory has the spiral form.

In flames and the combustion chambers of various power devices with temperature $T_c \le 2000$ K and pressure $P_c \le 0.1$ MPa, the parameters are usually $\sum_l n_l \approx N_S$ and $a < \lambda$, where n_l and N_S are the densities of lth-type ions and soot particles, respectively, and λ is the mean free path of the ion. In this case, lth-type ions interact with the soot particle in the kinetic regime [9]. In this case, the coefficient of the attachment of the ion to the particle, $\beta_l^{(P)}$, is expressed in terms of the interaction cross section $\sigma_l^P(V)$ through the usual relation

$$\beta_l^{(P)} = \int_0^\infty \sigma_l^{(P)}(V) V f_M(V) dV, \quad (2)$$

where $f_M(V)$ is the Maxwell distribution function of ions over velocities.

Baranov Central Institute of Aviation Motors, ul. Aviamotornaya 2, Moscow, 111116 Russia

** e-mail: star@ciam.ru*

1028-3358/04/4908-0441$26.00 © 2004 MAIK "Nauka/Interperiodica"

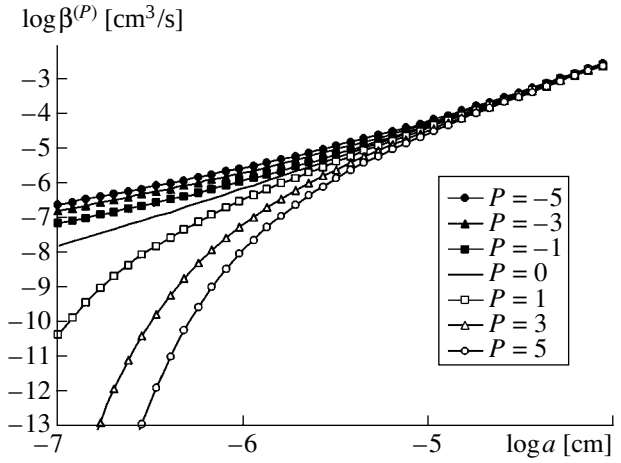

Fig. 1. Attachment coefficients $\beta^{(P)}$ for the NO^+ ion vs. the soot particle radius a for various P values and T_c = 1600 K.

The shortest distance r_a between the ion with mass m and velocity V and the soot particle is related to the impact parameter b as

$$b^2 = r_a^2\left[1 - \frac{2\varphi(r_a)}{mV^2}\right]. \quad (3)$$

In terms of the new variables $B_\Delta = \frac{b}{a}$, $\Delta = \frac{r_a}{a}$, and $Y = \frac{e^2}{amV^2}$, relation (3) for potential (1) takes the form

$$B_\Delta^2 = \Delta^2 - 2PY\Delta + Y(\Delta^2 - 1)^{-1}. \quad (4)$$

The capture sphere radius r_Δ is defined as the point of the minimum of the function $B_\Delta^2(\Delta)$ for $\Delta > 1$ and determined from the equation

$$\Delta^5 - PY\Delta^4 - 2\Delta^3 + 2PY\Delta^2 + (1 - Y)\Delta - PY = 0. \quad (5)$$

Determining the solution of Eq. (5) as $\Delta_P = \frac{r_\Delta}{a} = f(a, P, m, V)$, we find the cross section for the ion–particle interaction as

$$\sigma^{(P)} = \pi a^2 B_\Delta^2(\Delta_P).$$

Figure 1 shows the attachment coefficient for the NO^+ ion, which is present in the products of the combustion of any hydrocarbon fuels in air, as a function of the particle radius for various values of the parameter P and T_c = 1600 K. It is seen that $\beta^{(P)}$ value is large even for the similarly charged ion and particle and P = 5, especially for large particles (a > 50 nm); i.e., a rather large charge can be accumulated on soot particles. This effect is attributed to the appearance of the induced charge on a conducting particle due to its polarization. For pure Coulomb interaction, the maximum charge on the particle is obviously equal to $|q| = e$.

The characteristic charging time for the neutral particle with a = 20 nm to charge $q = \pm e$ is equal to $\tau_{ch} = (\beta_{(0)}N_t)^{-1} = 10^{-2}$ s for the total ion density $N_t = \sum_l n_l = 10^9$ cm^{-3} and T_c = 1600 K. This time approximately corresponds to the time of the residence of a gas in the combustion chambers of jet engines. Let us estimate the coagulation time for charged soot particles of various polarities when an increase in the coagulation constant due to electrostatic forces is maximal. The coagulation coefficient $K_{1,2}^{LQ}$ for particles that have radii a_1 and a_2 and opposite charges L and Q (particles attract each other) is determined by the expression [11]

$$K_{1,2}^{LQ} = \frac{K_{1,2}}{W_{1,2}^{LQ}}, \quad W_{1,2}^{LQ} = \frac{1 - \exp(-\nu)}{\nu},$$

$$\nu = \frac{LQe^2}{(a_1 + a_2)kT_c},$$

where k is Boltzmann's constant. For $a_1 = a_2$ = 20 nm and $|L| = |Q|$ = 5, the correction factor $(W_{1,2}^{LQ})^{-1}$ does not exceed 10 in the range T_c = 1500–2200 K. Since the Brownian coagulation constant for uncharged particles with a = 20 nm is equal to $K_{1,2} \approx 5 \times 10^{-9}$ cm^3 s^{-1} and the soot particle density is equal to $N_S = 10^7$ cm^{-3}, the characteristic coagulation time for particles with $|L| = |Q| = 5$ is equal to $\tau_c = (K_{1,2}^{LQ}N_S)^{-1} \approx 2$ s. We consider cases, where the time of the residence of the gas in a reactor is $\tau_{res} \le 0.1$ s, i.e., $\tau_{ch} \le \tau_{res} < \tau_c$. For this reason, the coagulation effect on the formation of the charge distribution function of particles is ignored.

FORMULATION OF THE PROBLEM AND A MATHEMATICAL MODEL

The diffusion combustion regime is characteristic for flames and the combustion chambers of power devices. In this case, soot particles are formed in the fuel-enriched zone (equivalent fuel/air ratio $\phi \approx 3$ and T_c = 1500–1800 K). Downstream of this zone, there is a zone with higher temperature $T_c \approx$ 2100–2400 K, where $\phi \approx$ 1.2–1.5. Further downstream, the temperature of the gas decreases to 1800 or 1300 K due to the mixing of combustion products with atmospheric air. The density of soot particles in various systems varies in the range $N_S = 7 \times 10^6$–2×10^8 cm^{-3}, and their distribution over the radius satisfies the lognormal law

$$N_S(a) = \frac{N_S}{\sqrt{2\pi}a\ln\sigma}\exp\left[-\frac{1}{2}\left(\frac{\ln a - \ln\bar{a}}{\ln\sigma}\right)^2\right].$$

The usual values for flames and combustion chambers are $\sigma = 1.56$ and $\bar{a} = 25$ nm [7].

To simulate the processes of the formation of soot and ions and their interaction in diffusion flames or combustion chambers, it is necessary to jointly solve hydrodynamic equations (usually, in the Navier–Stokes approximation), chemical kinetic equations, and equations describing the formation of soot particles and their interaction with ions. However, it is impossible to solve this problem even by using supercomputers. Therefore, considerable simplifications are required. We will consider only the formation of ions in various chemical and plasma-chemical reactions [12] and their interaction with a polydisperse ensemble of soot particles that are formed by the initial time in the closed adiabatic reactor.

Since soot particles with a given radius a can differ in the accumulated charge q, the description of the evolution of the soot-particle ensemble requires the introduction of the countable distribution function $f(a, q)$, which is conveniently represented as

$$f(a, q) = \sum_{j=1}^{Q} \varphi_j(a)\delta(q - q_j).$$

Here, $\varphi_j(a) = N_j f(a/q_i)$, N_j is the density of particles with charge q_j, Q is the number of possible values of the charge accumulated on soot particles ($Q = 2|P| + 1$), and $f(a/q_i)$ is the conditional probability that a particle with charge q_j has radius a.

Let us represent the continuous function $\varphi_j(a)$ by the superposition of the δ functions

$$\varphi_j(a) = \sum_{\gamma=1}^{\Gamma} N_{j\gamma}\delta(a - a_\gamma),$$

where $N_{j\gamma}$ is the density of particles with radius a_γ and charge q_j. In this case, the kinetic equation that describes change in the density of $j\gamma$th-fraction particles ($j = 1, 2, \ldots, Q, \gamma = 1, 2, \ldots, \Gamma$) due to the interaction with ions in the adiabatic reactor with ideal mixing can be represented in the form

$$\frac{dN_{j\gamma}}{dt} = \sum_{k=1}^{Q}\sum_{l=1}^{M} \theta_{jkl}\beta_l^{(k)}(a_\gamma, m_l, q_k)N_{k\gamma}n_l - N_{j\gamma}\sum_{l=1}^{M}\beta_l^{(k)}(a_\gamma, m_l, q_k)n_l, \quad (6)$$

where

$$\theta_{jkl} = \begin{cases} 1, & q_k + p_l = q_j, \\ 0, & q_k + p_l \neq q_j, \end{cases}$$

$$p_l = +1; -1,$$

and M is the number of components including ions and electrons.

Equations (6) (their number is equal to $Q \times \Gamma$) must be supplemented by balance equations for time variations of the density of various ions and neutral components that represent plasma-chemical reactions and the attachment of ions to soot particles. It is convenient to represent these equations in the form

$$\frac{dn_l}{dt} = Q_l^{\text{ch}} + Q_l^{\text{at}}, \quad (7)$$

$$\frac{dn_i}{dt} = Q_i^{\text{ch}}, \quad (8)$$

where

$$Q_i^{\text{ch}} = \sum_{q=1}^{M_1} S_{iq}, \quad S_{iq} = (\alpha_{iq}^- - \alpha_{iq}^+)[R_q^+ - R_q^-],$$

$$R_q^{+(-)} = k_{+(-)q}\prod_{i=1}^{n_q^{+(-)}} n_i^{\alpha_{iq}^{+(-)}},$$

$$Q_l^{\text{at}} = -n_l\sum_{k=1}^{Q}\sum_{\gamma=1}^{\Gamma}\beta_l^{(k)}(a_\gamma, m_l, q_k)N_k.$$

Here, n_i is the density of the ith neural component of a mixture in the gas phase ($i = 1, 2, \ldots, M_1$), α_{iq}^+ and α_{iq}^- are the stoichiometric coefficients of the qth reaction, $n_q^{+(-)}$ is the number of components involved in the (+) direct and (–) inverse reactions, and $k_{+(-)q}$ are the rates of these reactions.

Equations (6)–(8) are numerically solved jointly with the energy equation including the enthalpies of neutral and charged gas components by using an implicit second-order finite difference scheme. Analysis shows that the convergence of the solution of Eqs. (6) in integral characteristics such as the total particle number with charge q_j and the average radius of particles with charge q_j is achieved for the fraction number $\Gamma = 40$. At the same time, to ensure conver-

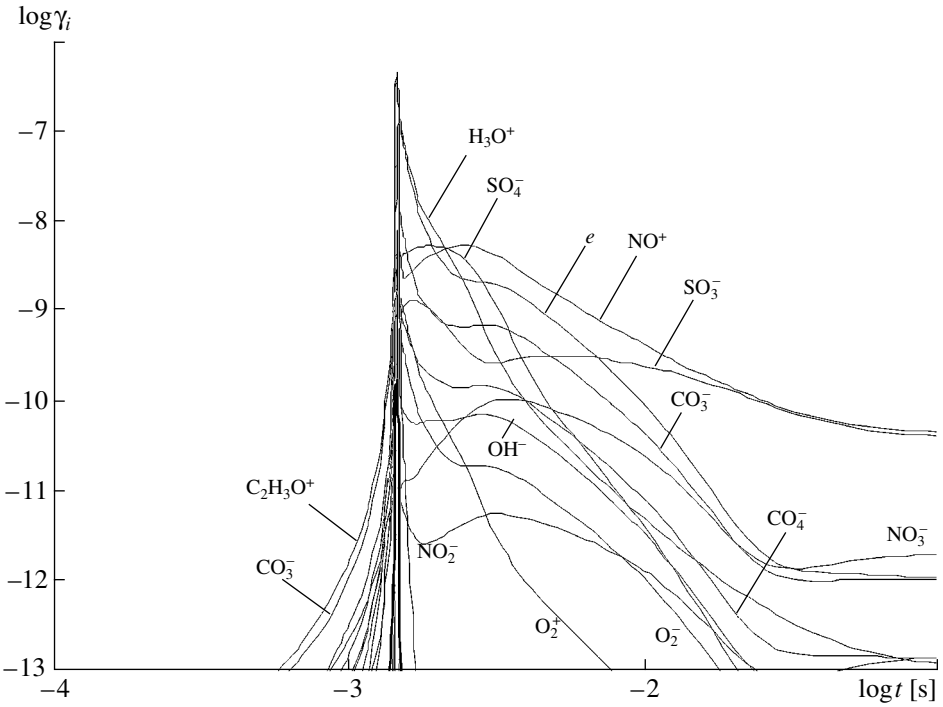

Fig. 2. Time dependence of the mole fractions of various ions and electrons upon the volume reaction in the mixture of destruction products i-C_8H_{18} + air + H_2S with T_{0c} = 1250 K, P_{0c} = 0.1 MPa, ϕ = 0.5, and [S] = 0.04% in the absence of soot particles.

gence in the number of particles with charge q_j and radii smaller than a_γ, discretization with $\Gamma = 80$ is necessary.

FORMATION OF THE ENSEMBLE OF CHARGED PARTICLES

As an example, we analyze the oxidation of the products of the destruction of i-C_8H_{18} with a small H_2S admixture in air in the adiabatic reactor of ideal mixing with T_{0c} = 1250 K and P_{0c} = 0.1 MPa. This mixture simulates fuels containing a small amount of sulfur quite well [12].

Figure 2 shows the calculated time variation in the densities of various ions and electrons in a volume reaction in the mixture with ϕ = 0.5 for a sulfur content of [S] = 0.04% in a fuel in the absence of soot particles. It is seen that the maximum density of ions and electrons is reached at the time $t = 2 \times 10^{-3}$ s, which corresponds to the maximum temperature of the gas after ignition (T_{max} = 2258 K). In this case, the maximum density is realized for ions H_3O^+ and electrons ($n_e = N_{H_3O^+} \approx 2 \times 10^{12}$ cm^{-3}). With an increase in t, the density of these particles decreases sharply due to the nonresonant charge-exchange reaction, dissociation ionization, and binary ion (electron)–molecule reactions. The NO^+ and SO_3^- ions dominate in the gas. Their density is equal to 2×10^8 cm^{-3} at t = 0.1 s. Thus, initially neutral soot particles in the gas are charged due to the interaction first with electrons and H_3O^+ ions and then (for $t > 10^{-2}$ s) with NO^+ and SO_3^- ions. Since the electron is much lighter than any ion, the coefficient of the attachment of electrons to soot particles is much larger than for ions. Therefore, most soot particles are negatively charged immediately after reaching T_{max} ($t = 2 \times 10^{-3}$ s). In this case, rather large negative charge $q \approx 30e$ can be accumulated even on moderate-size particles ($a \approx 20$ nm). The average charge of the entire ensemble of soot particles is also negative. Further, negatively charged particles, particularly with large charge q, are neutralized due to the interaction with positive ions H_3O^+ and NO^+. In addition, a noticeable number of positively charged soot particles appear.

Figure 3 shows the charge distribution of soot particles with radii smaller than a certain value at time t = 0.1 s upon the volume reaction in the mixture with ϕ = 0.5, [S] = 0.04%, and $N_S = 8 \times 10^6$ cm^{-3}. In this case, the gas temperature at the exit from the reactor reaches 2100 K and the maximum densities of positive N^+ and negative N^- ions are equal to 8×10^7 and 5×10^7 cm^{-3}, respectively. At any time, the plasma in the reactor is quasi-neutral; i.e.,

$$\sum_l n_l^+ - \sum_k n_k^- - n_e^- + \sum_p (q_p N_S^+(q_p) - q_p N_S^-(q_p)) = 0,$$

where $N_S^+(q_p)$ and $N_S^-(q_p)$ are the densities of positively and negatively charged soot particles with charge q_p,

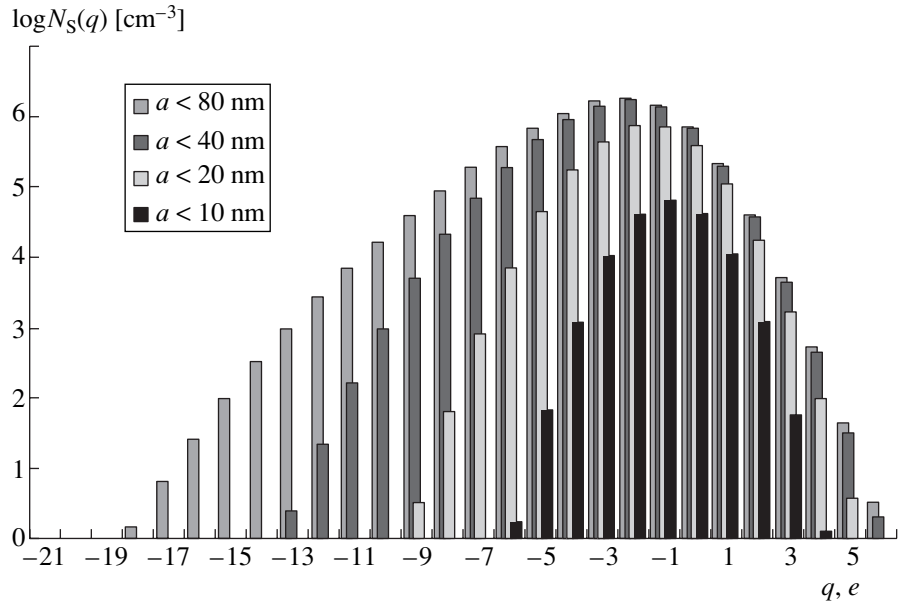

Fig. 3. Charge distribution of soot particles with radii smaller than a certain fixed value at time $t = 0.1$ s upon the volume reaction in the mixture of destruction products i-C_8H_{18} + air + H_2S with $T_{0c} = 1250$ K, $P_{0c} = 0.1$ MPa, $\phi = 0.5$, [S] = 0.04%, and $N_S = 8 \times 10^6$ cm^{-3}.

respectively. It is seen that small particles with $a <$ 10 nm can accumulate negative charge $q \le 5e$ and positive charge $q \le 3e$. At the same time, negative charge on relatively large particles can reach even $17e$. Under these conditions, the number of negatively charged particles (~85%) is much larger than the number of positively charged particles (~5%). This asymmetry arises because the mass of negatively charged electrons is lower than the mass of positive ions NO^+ and H_3O^+ and, therefore, the attachment coefficient of these ions is smaller.

When ϕ decreases to 0.25, the electron density in the plasma decreases, which reduces the asymmetry of the charge distribution function of particles (the number of positively charged particles increases significantly). This tendency also remains for the larger density of soot particles ($N_S = 8 \times 10^7$ cm^{-3}). However, since the total rate

$$W_l = \sum_{\gamma=1}^{\Gamma} \sum_{k=1}^{Q} \beta_l^{(k)} N_{k\gamma}$$

of the withdrawal of ions of a given type (electrons) from the gas phase on the surface of soot particles is higher in this case, a significant difference between the time profiles of N^+ and N^- arises. The density of positive ions becomes much higher than the density of negative ions (by a factor of 60 at $t = 0.1$ s). The interaction of ions with particles reduces the ion density with time. The degree of this decrease increases with N_S. This behavior is illustrated in Fig. 4, which shows $N^{+(-)}(t)$ for the total density of soot particles $N_S = 0$, 8×10^6, and 8×10^7 cm^{-3}. Since soot particles are virtually always produced in flames and the combustion chambers of jet engines, the comparison of the results of numerical simulation with measurements of the densities of positive and negative ions in such objects requires the inclusion of the interaction of ions with soot particles.

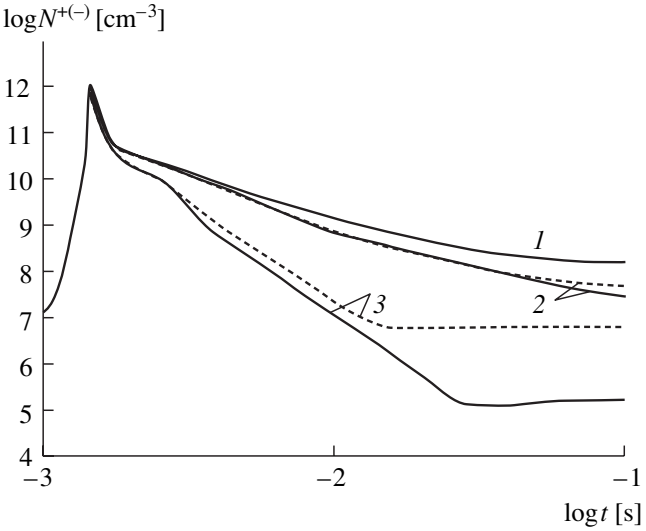

Fig. 4. Time dependence of the densities of (dotted lines) positive N^+ and (solid lines) negative N^- ions (electrons) upon the volume reaction in the mixture of destruction products i-C_8H_{18} + air + H_2S with $T_{0c} = 1250$ K, $P_{0c} = 0.1$ MPa, $\phi = 0.5$, [S] = 0.04%, and $N_S = (1)$ 0, (2) 8×10^6, and (3) 8×10^7 cm^{-3}.

Thus, the above analysis shows that the interaction of ions and electrons with soot particles produced upon the combustion of hydrocarbon fuels leads to the accumulation of both positive and negative charges on particles. Relatively large particles with radii $a \geq 40$ nm can acquire charge $q = 10–12e$, and small particles with $a \leq 10$ nm can be charged only to $q = (3–5)e$. The charge distribution function of particles and the relative fraction of positively and negatively charged particles depend on the combustion conditions (they determine the densities of ions, electrons, and soot particles). The interaction of soot particles with ions, as well as plasma-chemical reactions, is an effective mechanism of decreasing the ion density in flames and the combustion chambers of power devices.

ACKNOWLEDGMENTS

This work was supported in part by the Russian Foundation for Basic Research (project nos. 02-01-00703 and 04-03-33162), the Council of the President of the Russian Federation for Support of Young Russian Scientists and Leading Scientific Schools (project no. NSh-1574.2003.1), and the US Civilian Research and Development Foundation for the Independent States of the Former Soviet Union (grant no. RC1-2327-MO-02).

REFERENCES

1. P. Chylek, G. B. Lesins, G. Videen, *et al.*, J. Geophys. Res. **101** (D18), 23365 (1996).
2. O. B. Popovicheva, A. M. Starik, and O. N. Favorskiĭ, Izv. Akad. Nauk, Fiz. Atmos. Okeana **36** (12), 31 (2000).
3. H. X. Zhang, C. M. Sorensen, E. R. Ramer, *et al.*, Langmuir **4**, 867 (1988).
4. M. Smith, K. Lee, and T. Matsoukas, J. Nanoparticle Res. **1**, 185 (1999).
5. A. A. Onischuk, S. de Stasio, V. V. Karasev, *et al.*, J. Aerosol Sci. **34**, 383 (2004).
6. O. B. Popovicheva, N. M. Persiantseva, A. M. Starik, and E. E. Loukhovitskaya, J. Environ. Monitor. **5**, 265 (2003).
7. *Soot Formation in Combustion*, Ed. by H. Bockhrom (Springer-Verlag, Heidelberg, 1994).
8. H. F. Calcote and D. G. Keil, Pure Appl. Chem. **62**, 815 (1990).
9. W. A. Hoppel and G. M. Frick, Aerosol. Sci. Technol. **5**, 1 (1986).
10. A. B. Fialkov, Prog. Energy Combust. Sci. **23**, 399 (1997).
11. J. H. Seinfeld and S. P. Pandis, *Atmospheric Chemistry and Physics* (Willey, New York, 1998).
12. A. M. Starik, A. M. Savel'ev, N. S. Titova, and U. Schumann, Aerospace Sci. Technol. **6**, 63 (2002).

Translated by R. Tyapaev

Doklady Physics, Vol. 49, No. 8, 2004, pp. 447–450. Translated from Doklady Akademii Nauk, Vol. 397, No. 6, 2004, pp. 758–761.

PHYSICS

Simulation of Intramolecular-Transformation Kinetics and Complex-System Spectra with Allowance for Isomeric Transitions

Corresponding Member of the RAS L. A. Gribov, V. I. Baranov, and M. V. Zavaliĭ

Received April 5, 2004

Advantages of photochemistry are associated with the production of new materials and primarily with the possibility of optical control of proceeding chemical reactions. Despite all the achievements of photochemistry and accumulated experimental data, there exists a critical area significantly hampering progress in this field. All spectral methods of investigating substances are indirect. Therefore, the determination of an unambiguous physical correlation between the parameters of molecular models and directly measured spectral representations is urgent. This determination is based on solving direct and inverse spectral problems. These problems have been thoroughly studied in normal spectroscopy. However, not only the excitation method and the time dependence of the spectral pattern but also the transformation of the initial object should be additionally considered in photochemistry. It is evident that both the interpretation and prediction of proceeding photochemical reactions are impossible without numerical simulation.

In this study, we develop the theory of the process under consideration, calculation algorithms, and computer codes, which makes it possible to perform computer experiments aimed at the interpretation of dynamic processes at the level of the comprehensive description of molecular models under various photoexcitation conditions. Previously, we developed a database for simulating molecular spectra with the time resolution corresponding to short-pulse photoexcitation [1, 2]. In the present study, we consider the possibility of light-induced isomer–isomer transformations including multistage photochemical processes. It was shown in [3] that the isomer–isomer transition state can be adequately described by the model where a single common level with the stationary energy E_{ev} is introduced for a pair of resonating isomer levels with energies $E_{ev}^{(1)} = E_{ev}^{(2)} = E_{ev}$ and wave functions ψ_1 and ψ_2. The square of the modulus of the wave function of this common level is

$$|\psi(t)|^2 = \psi_1^2 \cos^2 \omega t + \psi_2^2 \sin^2 \omega t.$$

Here, $\omega = \frac{2}{\pi\hbar} E_{ev} S_{ev}^{(1,2)}$ is the quantum-beat frequency and $S_{ev}^{(1,2)}$ is the overlap integral of the functions ψ_1 and ψ_2. The entire process of dissipating the electromagnetic energy introduced into the system can be described by a set of first-order linear differential equations. In these equations, the ordinary probabilities of vibronic transitions, which are multiplied by factors oscillating with time (for transitions involving isomer–isomer levels), stand as the coefficients of level populations.

The algorithm and program package were developed with allowance for the high dimensionality of the problem ($\geq 10^4$ equations). The most efficient method for solving this set of equations, especially with time-dependent coefficients, is numerical integration [4]. Compared to the program package developed for the case of a single molecule [1, 2], the algorithm for the multi-isomeric case was significantly revised to perform calculations within realistic time intervals. The most important improvement was the generalization of the calculation procedure for the multi-isomeric case, since the problem under solution is complicated not only quantitatively (increase in the time consumption by several orders of magnitude) but also qualitatively (more complicated interrelation of the equations and the wide spread of time parameters). Based on the developed theory, an efficient algorithm was realized for automatically constructing and analyzing the set of equations, as well as rejecting those of them that do not affect the process dynamics or the final result due to the physical features of the specific molecular model (low-probable and forbidden transitions, inactive levels, etc.). In addition, an algorithm of automatically choosing the integration step for solving the set of equations was developed with due regard to all time characteristics of the specific molecular model. The choice of the

Vernadsky Institute of Geochemistry and Analytical Chemistry, Russian Academy of Sciences, ul. Kosygina 19, GSP-1 Moscow, 119991 Russia
e-mail: gribov@geokhi.ru, baranov@geokhi.ru, zavalii_maksim@mail.ru

1028-3358/04/4908-0447$26.00

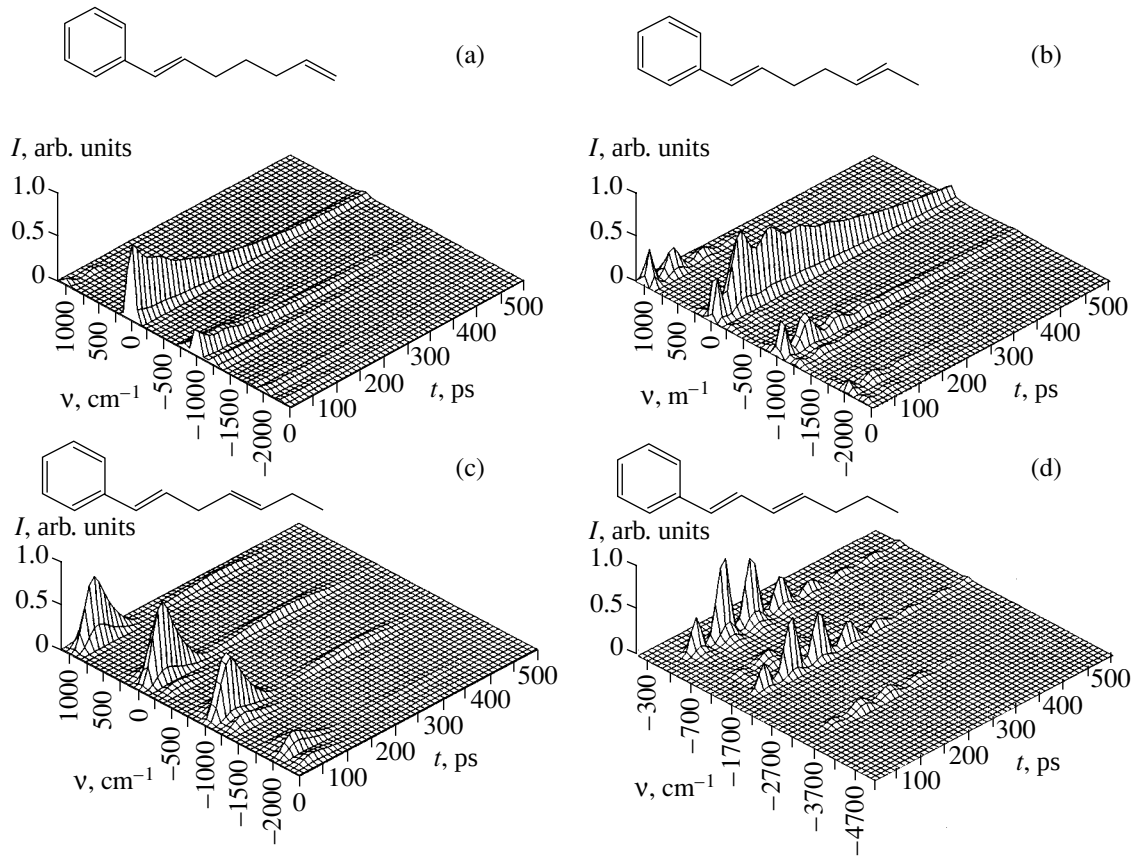

Fig. 1. Fluorescence dynamic spectra of heptadienyl benzene isomers in the case of the broadband excitation of isomer 1. The frequencies are given with respect to the 0–0 transitions for isomers (a) 1, (b) 2, (c) 3, and (d) 4.

integration step is complicated because significantly different (by a factor of 10 or higher) exponential times of state relaxations and quantum-beat periods are possible (and, as a rule, realized) in the problem under consideration. The resulting code allows us to simulate the dynamic vibronic spectra of complex molecules in the real-time scale (minutes) for various excitation conditions with isomeric transitions taken into account. The numbers of isomeric forms and resonating levels are not limited.

When the quantum-beat period is an order of magnitude shorter than the spectrum decay time, the problem becomes much more difficult, so that the time of calculations on a personal computer becomes unacceptably long for the large number (>10) of isomeric transitions. Therefore, a program package for an MBC-1000 supercomputer was developed. This required solving new problems associated with parallel calculations and storage of intermediate data in the computer memory. An algorithm based on parallel solutions of subproblems for each isomeric form on its own processor turned out to be the most efficient and optimal with respect to the time spent. By virtue of the features of both the problem and molecular model, this allowed us to minimize the expectation time required by the processors for necessary information exchange between them (isomers). During the calculation process, special data structures that are stored in the memory of the multiprocessor computer and then transmitted as a common packet from the random-access memory to the fixed storage were used. Thereby, a long-time procedure of data storage in the external memory of the supercomputer was excluded, and the time of the data transmission process was optimized. The calculation time is independent of the isomer number and, e.g., for large molecules (more than 50 atoms), is shorter than 60 minutes.

The program package was tested in several model calculations, e.g., for isomer–isomer transformation of heptadienyl benzene such as hepta-1,6-dienyl benzene ⟷ hepta-1,5-dienyl benzene ⟷ hepta-1,4-dienyl benzene ⟷ hepta-1,3-dienyl benzene (isomers 1, 2, 3, and 4, respectively). The kinetics of isomeric transformations and its spectral manifestations as a function of initial conditions (excitation character, initial isomeric form, its excited state, etc.) were studied. The goal of this study was, first, to verify the code in the case of actual objects and, second, to elucidate a number of general rules. We wished to clarify the following questions. What is the ratio of the total probabil-

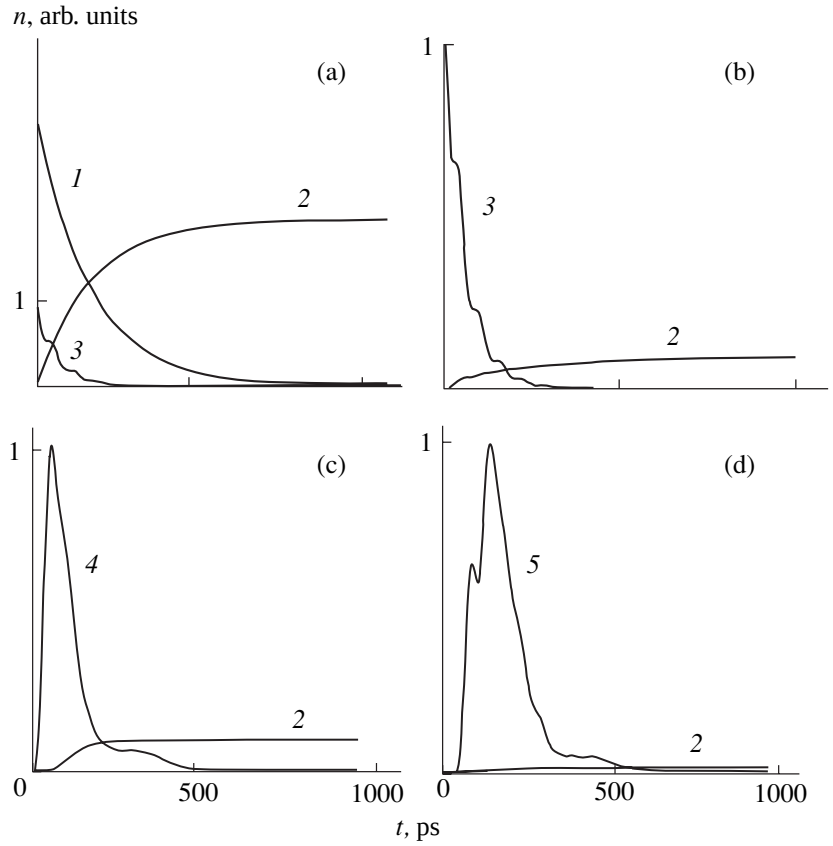

Fig. 2. Time dependences of level populations for heptadienyl benzene isomers (a) 1, (b) 2, (c) 3, and (d) 4 in the case of broadband excitation of isomer 1: (*1*) first excited purely electron state of isomer 1; (*2*) ground state of the isomers; resonance levels of isomers (*3*) 1 and 2, (*4*) 2 and 3, and (*5*) 3 and 4. Populations are normalized to their maximum values for the corresponding resonance levels.

ity of isomeric transitions to the frequency of quantum beats for which observations of isomer fluorescence spectra of the intensity comparable with that of isomer 1 are possible? Under what conditions are quantum beats in the spectrum vibration structure observed and what are their features? What are the time and quantitative characteristics of isomer formation? The features of chain isomer–isomer rearrangement processes were of special interest.

Some results of the computer experiments for heptadienyl benzene are presented below. Based on the analysis of vibronic states, the corresponding vibrational sublevels of the first excited electron state were chosen as isomeric resonating states. For the isomer-1 broadband excitation model, the initial populations of the vibrational sublevels of the first excited state were taken to be proportional to the corresponding probabilities of electron-vibrational transitions in the case of absorption of the incident radiation.

The calculated intensities for the isomer spectra are presented in Fig. 1, and the dynamics of the isomeric-level population is shown in Fig. 2. The results of the model calculations, in particular, indicate the following properties.

For vibronic spectra, the time dependence of the vibrational-structure intensity depends substantially on the relation between the probabilities of vibronic and isomeric (i.e., characterized by the parameter ω) transitions. The prediction of these properties and features is impossible without model calculations due to the complicated hierarchy of transitions and couplings between level sets. The luminescence spectrum maximum is shifted in time due to the gradual production of new (with respect to the initial ones) isomeric molecular forms. The beating effect in both the luminescence spectra and changes in level populations is observed. Therefore, their time dependence is no longer of a simple exponential character. The fine time dependence (oscillations) of both the spectra and level populations becomes significantly more complicated in the isomer series. For example, isomer 1 manifests only oscillations at a frequency ω_1 (Fig. 1a), whereas isomer 4 exhibits those at frequencies ω_1, ω_2, and ω_3 (see Fig. 1d). The level population plots (Fig. 2) demonstrate the dynamics of molecular transitions into isomeric forms 2, 3, and 4. Because of isomeric transitions, the processes occurring not only immediately in a particular isomeric form but also in all other forms of the isomeric chain under consideration noticeably

affect the form of the time dependence of the population level for the given isomer. This effect is most pronounced for isomers far from the initial one. For example, the population dynamics of isomer 4 (Fig. 2d) is determined by the probabilities of all isomeric transitions, which leads, in particular, to the appearance of several maxima in the resonating-level population curve.

The final total populations and maximum intensities in isomer spectra are significantly different for different isomers. Their relative values for the specific model calculation are (intensities) 1, 10^{-1}, 8×10^{-4}, and 2×10^{-7} and (populations, where the fraction of molecules that were not initially excited is ignored) 1, 10^{-1}, 7×10^{-4}, and 1×10^{-7} for isomers 1, 2, 3, and 4, respectively. In the case of overlapping bands, the spectra of final isomeric forms (3, 4) can be so weak that they become unobservable. For the high probabilities of optical transitions, the state populations for isomeric forms 3 and 4 decrease dramatically in isomer series; i.e., isomerization decreases rapidly in the isomeric series. The noticeable concentrations of the final isomeric form and its spectral manifestations are possible at the low probabilities (oscillator strengths of electron transitions) of excited-level luminescence of intermediate forms. In this case, smallness is of critical importance with respect to quantum-beat frequencies rather than to the absolute value. This property can be realized for highly allowed transitions. Nevertheless, in the properly organized spectral experiments (choice of excitation and observation conditions, etc.), the isomerization effect and its dynamics can be detected even for the aforementioned cases difficult for observation.

The developed program package provides for the simulation of intramolecular-transformation kinetics and corresponding dynamic spectra on a personal computer and supercomputer in real time. This ensures conditions for the comprehensive study and prediction of the physicochemical laws of fast processes involving the transformation and transmission of energy and information inside the intramolecular space by complex systems with allowance for isomer–isomer transformations. In addition, the optimal setting of a full-scale experiment can be chosen by using model calculations, which is extremely important, e.g., in designing the molecular elements of nanotechnology devices for information processing.

ACKNOWLEDGMENTS

This work was supported by the Russian Foundation for Basic Research (project no. 04-03-32086) and the Council of the President of the Russian Federation for Support of Young Russian Scientists and Leading Scientific Schools (project no. NSh-1186.2003.3).

REFERENCES

1. S. A. Astakhov and V. I. Baranov, Opt. Spektrosk. **90**, 237 (2001) [Opt. Spectrosc. **90**, 199 (2001)].
2. S. A. Astakhov, V. I. Baranov, and L. A. Gribov, J. Mol. Struct. **655**, 97 (2003).
3. L. A. Gribov, *From Theory of Spectra to Theory of Chemical Transformations* (Editorial URSS, Moscow, 2001).
4. V. I. Baranov, M. V. Zavaliĭ, and L. A. Gribov, Zh. Prikl. Spektrosk. **70**, 626 (2003).

Translated by G. Merzon

Doklady Physics, Vol. 49, No. 8, 2004, pp. 451–455. Translated from Doklady Akademii Nauk, Vol. 397, No. 6, 2004, pp. 762–766.

PHYSICS

Central Manifold and the Problems of the Chapman–Enskog Projection for the Boltzmann–Peierls Equation

P. A. Zakharchenko* and E. V. Radkevich**

Presented by Academician A.M. Dykhne March 10, 2004

Received March 10, 2004

The Chapman–Enskog projection is analyzed on examples of nonlinear diffusion and the so-called second sound [4–9, 13].

HYDRODYNAMIC APPROXIMATION

It is well known that systems of Grad's moments [1, 2] can be treated not only as approximations of kinetic equations but also as extensions or smoothing of limiting systems and their first approximations obtained phenomenologically (e.g., systems of Euler gasdynamic equations and systems of Navier–Stokes or Navier–Stokes–Fourier hydrodynamic equations).

The derivation of hydrodynamic equations from microscopic description (inclusion of hydrodynamic equations into the hierarchy of moment systems) is a classical problem of physical kinetics. The famous Chapman–Enskog method [3] provides solutions of the Boltzmann kinetic equation as formal power series in a small parameter $\varepsilon = \mathrm{Kn}^{-1}$, where Kn is the Knudsen number. This parameter presents the ratio of the mean free path of a particle to the variation scale of hydrodynamic quantities—density, mean velocity, and temperature. The truncation of the Chapman–Enskog series on the ε^0-order terms leads to Euler hydrodynamics. Navier–Stokes hydrodynamics is obtained as the first correction ε^1. So-called Barnet and super-Barnet hydrodynamics correspond to ε^2 and ε^3, respectively.

Post-Navier–Stokes terms are introduced to extend hydrodynamic description beyond the scope of the strict hydrodynamic limit $\varepsilon \ll 1$. However, even in the simplest regime of one-dimensional linear deviation from the global-equilibrium state [14], the system of Barnet hydrodynamic equations breaks the basic physical conditions of the derivation of the Boltzmann equation. Indeed, rather short acoustic waves are unstable (so-called ultraviolet catastrophe) and increase rather than decrease with time, which contradicts the *H* theorem, according to which any quite small perturbation must decay. Moreover, this situation is not improved in the next, super-Barnet, approximation. The ultraviolet catastrophe, which is manifested in low-order truncations of the Chapman–Enskog expansion, leads to very serious difficulties in the problem of the extension of hydrodynamic description to far nonequilibrium domains (see [1, 3]).

The Euler and Navier–Stokes approximations remain basic approximations of hydrodynamic description. Therefore, the problem of their extension is one of the central open problems of kinetic theory. What happens in the Chapman–Enskog approximation of kinetic equations? The reference to the asymptotic character of this method is unconvincing. Any divergences of reasonable asymptotic methods usually reflect deeper characteristic properties of models and their structures described by these methods.

NONEQUILIBRIUM VARIABLES

The aim of this work is to analyze the properties of the Chapman–Enskog projection [3] for the moment approximations of kinetic equations [1, 2], primarily the so-called diffusion mode [4–9, 13] of the Boltzmann–Peierls kinetic equation. One of the basic problems of the moment theory of nonequilibrium thermodynamic processes is associated with the specific difficulties of mixed problems for moment systems. Some unknowns of a problem—nonequilibrium variables (higher order moments)—have no intuitive physical meaning. Such variables cannot be determined from experimental data [1, 15]. What do Cauchy data and, the more so, boundary data mean for these variables? This circumstance should be taken into account when formulating a mixed problem in the structure of boundary conditions. What are physically correct boundary conditions in this case?

Moscow State University,
Vorob'evy gory, Moscow, 119992 Russia
** e-mail: hekex@mail.ru*
*** e-mail: evrad@land.ru*

1028-3358/04/4908-0451$26.00

Comparative analysis of exact solutions of the Cauchy problem of kinetic equations and their moment approximations shows that a rather large number of nonequilibrium variables are required for a reasonably small discrepancy. In particular, no less than the 40-moment approximation of the Boltzmann–Peierls kinetic equation is required to adequately describe thermal processes in crystals [9]. The number of boundary conditions presenting the behavior of nonequilibrium variables near the boundary is small. The temperature jump on a wall and slipping velocity are possible for a rarefied gas. Boundary conditions describing these phenomena were first proposed in [15]. However, these conditions are insufficient for the formulation of full-scale boundary value problems. The problems arising when simulating processes near the boundary are primarily associated with both the behavior of nonequilibrium variables in this domain and the role of nonequilibrium variables in the stability of processes at large times. In addition, these problems are associated with analysis of the conditions of the stability of the passage from the mixed problem of the moment approximation of the Boltzmann kinetic equation to the mixed problem for the system of Euler gas-dynamic equations in the limit $\mathrm{Kn} \longrightarrow \infty$ or $t \longrightarrow \infty$.

As was noted above, it is impossible to experimentally control the initial and boundary values for higher moments, which we called nonequilibrium, in contrast to the basic conservative quantities (hydrodynamic quantities) having physical interpretation. An approach proposed by Chapman and Enskog (see [3]) enables one to remain in the framework of the initial and boundary conditions only for conservative variables, because the concept of the approach is to find the operator dependence of nonequilibrium variables on the basic conservative quantities, i.e., to find the projection from the phase space of moment approximations onto the phase space of conservative variables. The initial and boundary conditions in the phase space of the basic variables are required for the Chapman–Enskog projection of the moment system.

BOLTZMANN–PEIERLS EQUATION

The phonon-gas model [1] makes it possible to describe heat transfer in a crystal. This transfer can be treated as the transfer of particles (phonons) similar to the transfer process in an ordinary gas but with some differences. The most important differences from the ordinary gas are as follows.

(i) Phonons can appear and disappear upon interaction. The phonon-number distribution in time and space is determined by the local temperature at a point (x, t).

(ii) In the interaction of phonons, energy is conserved, whereas momentum is not generally conserved. For this reason, phonons are called quasiparticles.

The following three mechanisms of energy transfer exist in the phonon gas.

(i) Energy is transferred by ballistic phonons, which do not interact when moving in the crystal, and energy is conserved.

(ii) Energy is transferred by the so-called second sound if there is the interaction of phonons upon which the quasimomentum is conserved. This mechanism is similar to a sound wave in the ordinary gas, which propagates with the conservation of the energy and momentum of colliding particles (due to this similarity, this transfer mechanism is called the second sound).

(iii) Energy is transferred by diffusion upon scattering on lattice defects and impurities in the crystal, where the quasimomenta of phonons are not conserved upon interaction in most cases (it is an analogue of ordinary heat transfer, which is damped in a very short time).

MOMENT APPROXIMATION

As was mentioned above, Chapman and Enskog proposed an approach, the so-called Chapman–Enskog projection, enabling one to remain in the framework of the initial and boundary conditions only for basic variables. The concept of the approach is to find the operator dependence of nonequilibrium variables on the basic variables. In particular, for the Cauchy problem for the one-dimensional three-moment system of the phonon gas

$$\partial_t \tilde{e} + \partial_x p = 0, \quad \tilde{e} = \frac{e}{c^2}, \tag{1}$$

$$\partial_t p + \alpha_1 \partial_x e + \partial_x N + \frac{1}{\tau_R} p = 0, \tag{2}$$

$$\partial_t N + \alpha_2 \partial_x p + \frac{1}{\tau} N = 0, \quad \frac{1}{\tau} = \frac{1}{\tau_N} + \frac{1}{\tau_R}, \tag{3}$$

with one basic (thermodynamic) variable e, the conditions of the representation

$$p = q(\partial_x)e, \quad N = \mu(\partial_x)e$$

are analyzed. Here and in Eqs. (1)–(3), $\tau_R > 0$ and $\tau_N > 0$ are the relaxation times of the R and N normal processes, respectively [8]; $\alpha_1 = \frac{c^2}{3}$; $\alpha_2 = \frac{4c^2}{15}$; c is the Debye velocity [8]; and μ and q are pseudodifferential operators whose orders are no more than zero.

CHAPMAN–ENSKOG PROJECTION

Let us determine the classical Chapman–Enskog projection for system (1)–(3). To this end, we consider

the system at large times; i.e., a small parameter $\varepsilon > 0$ is introduced as

$$\partial_t \tilde{e} + \partial_x p = 0, \tag{4}$$

$$\partial_t p + \alpha_1 \partial_x e + \partial_x N + \frac{1}{\varepsilon}\frac{1}{\tau_R} p = 0, \tag{5}$$

$$\partial_t N + \alpha_2 \partial_x p + \frac{1}{\varepsilon}\frac{1}{\tau} N = 0. \tag{6}$$

The Chapman–Enskog expansion is sought in the form

$$\begin{aligned} p &= \varepsilon q_1(\partial_x)e + \varepsilon^2 q_2(\partial_x)e + \ldots, \\ N &= \varepsilon \mu_1(\partial_x)e + \varepsilon^2 \mu_2(\partial_x)e + \ldots. \end{aligned} \tag{7}$$

Substituting Eq. (7) into (4)–(6) and equating terms containing the same ε powers to zero, we arrive at the first operator relations

$$q_1 = -\tau_R \alpha_1 \partial_x,$$

$$q_3 = -\tau \partial_x \mu_2 + \partial_x q_1^2 = -(\tau^2 \tau_R \alpha_2 \alpha_1 + \alpha_1^2 \tau_R^2)\partial_x^2.$$

From these relations, the so-called Navier–Stokes and post-Navier–Stokes approximations of the Boltzmann–Peierls equation follow in the form

$$\partial_t e = \varepsilon \tau_R \alpha_1 \partial_x^2 e,$$

$$\partial_t e = \varepsilon \tau_R \alpha_1 \partial_x^2 e + \varepsilon^3 (\tau^2 \tau_R \alpha_2 \alpha_1 + \alpha_1^2 \tau_R^2)\partial_x^3 e,$$

respectively. The first approximation is stable, and the second and higher approximations are unstable, whereas moment system (1)–(3) is stable. Indeed, its dispersion equation

$$\omega\left(\omega - \frac{i}{\tau}\right)\left(\omega - \frac{i}{\tau_R}\right) - \xi^2\left((\alpha_1 + \alpha_2)\omega - \alpha_1 \frac{i}{\tau}\right) \tag{8}$$

$$= P_0 - i\gamma_1 P_1 - \gamma_2 P_2 = 0,$$

where

$$P_0 = \omega(\omega^2 - (\alpha_1 + \alpha_2)\xi^2),$$

$$P_1 = \omega^2 - \alpha_1 \tau_R (\tau + \tau_R)^{-1} \xi^2, \quad P_2 = \omega,$$

$$\gamma_1 = \frac{\tau + \tau_R}{\tau \tau_R}, \quad \gamma_2 = \frac{1}{\tau \tau_R},$$

satisfies the following conditions of the stability of hyperbolic bundles [8, 9]: first, the polynomials P_0, P_1, and P_2 of the bundle are hyperbolic and, second, the roots of the neighboring polynomials of the bundle strictly separate each other. Such a situation often occurs in quantum and statistical physics. For the approximation to be stable, many expansion terms must usually be taken. The question is how many terms must be taken?

REGULAR EXPANSION. QUANTIZATION

We analyze the regular expansion of the form

$$e = e_0 + \varepsilon e_1 + \ldots, \quad p = \varepsilon p_1 + \ldots, \quad N = \varepsilon N_1 + \ldots.$$

We substitute these sums into Eqs. (4)–(6). The first 20 terms of the expansion are grouped into the expressions

$$p_\varepsilon = \partial_x q_N(-\varepsilon^2 \partial_x^2)e_\varepsilon, \quad N_\varepsilon = \partial_x^2 \mu_{N-1}(-\varepsilon^2 \partial_x^2)e_\varepsilon, \tag{9}$$

where q_N and μ_N are the Taylor series of the pseudodifferential operators $q(-\partial_x^2)$ and $\mu(-\partial_x^2)$ of orders –2 and 0, respectively. Thus, quantization is seen in the explicit form: the order of the moment corresponds to the order of the Chapman–Enskog projection operator. Let us show that relations (9) are realized.

CHAPMAN–ENSKOG PROJECTION OF THE DIFFUSION TYPE

We now consider the following Chapman–Enskog projection for system (1)–(3):

$$p = \partial_x q(-\partial_x^2)e, \quad N = \partial_x^2 \mu(-\partial_x^2)e,$$

which is called the diffusion projection. We set $M(\xi^2) = \xi^2 \mu(\xi^2)$ and $Q(\xi^2) = \xi^2 q(\xi^2)$. Then, the following equations for the projection operators are obtained from the Fourier transforms of Eqs. (2) and (3):

$$\begin{aligned} M &= -\alpha_2 Q\left(Q + \frac{1}{\tau}\right)^{-1}, \\ Q\left(Q + \frac{1}{\tau_R}\right)\left(Q + \frac{1}{\tau}\right) &+ \xi^2\left((\alpha_1 + \alpha_2)Q + \alpha_1 \frac{1}{\tau}\right) = 0. \end{aligned} \tag{10}$$

Substitution $Q = i\omega$ obviously converts Eq. (10) to dispersion polynomial (8). The condition of existence of a real solution of the equation for the diffusion generating function Q [$Q(0) = 0$] is very simple:

$$\frac{\tau}{\tau_R} > \frac{\alpha_1}{\alpha_1 + \alpha_2}. \tag{11}$$

Here, we took into account that $\tau_R > \tau$ due to physical reasons. Condition (11) determines the window of admissible parameters τ_R and τ for which the diffusion projection exists. Then, the Cauchy problem for the projection of system (1)–(3) (factor system for the diffusion Chapman–Enskog projection) can be written as

$$\partial_t \tilde{e}(t, \xi) - Q(-\partial_x^e)\tilde{e} = 0, \quad \tilde{e}|_{t=0} = \tilde{e}_0(x). \tag{12}$$

The stability of this equation follows from the properties of the generating function Q.

DIFFUSION MODE

Now, the general results for the diffusion mode can be formulated.

Lemma (on the factorization of the dispersion polynomial). *The dispersion polynomial of the multidimensional* ($d = 2$ *and* 3) *system of moments to the order* $2M + 1 \geq 3$ *inclusively has a dispersion polynomial of the one-dimensional system of moments of the same order as a multiplier.*

For example, for the following two-dimensional system of moments up to the third order inclusively

$$\partial_t \tilde{e} + \partial_{x_k} p_k = 0,$$

$$\partial_t p_j + \alpha_1 \partial_{x_j} \tilde{e} + \partial_{x_k} N_{\langle jk \rangle} + \frac{1}{\tau_R} p_j = 0,$$

$$\partial_t N_{\langle ij \rangle} + \frac{3}{4}\alpha_2 \partial_{x_j} p_{<i} + \frac{1}{\tau} N_{\langle ij \rangle} = 0, \quad i, j = 1, 2, 3,$$

the polynomial of the dispersion equation ($d = 3$)

$$\left(\omega - \frac{i}{\tau}\right)\left(\left(\omega - \frac{i}{\tau}\right)\left(\omega - \frac{i}{\tau_R}\right) - \frac{3}{4}\alpha_2 |\xi|^2\right)$$

$$\times \left(\omega\left(\omega - \frac{i}{\tau}\right)\left(\omega - \frac{i}{\tau_R}\right) - \alpha_2 |\xi|^2 \omega - \left(\omega - \frac{i}{\tau}\right)\alpha_1 |\xi|^2\right) = 0$$

has dispersion polynomial (8) of system (1)–(3) as a multiplier.

Theorem (on the existence of the diffusion mode). *For a multidimensional* ($d = 2$ *and* 3) *system of moments up to the order* $2M + 1 \geq 3$ *inclusively, the necessary and sufficient condition of the existence of the Chapman–Enskog projection of the form*

$$p_j = \partial_{x_j} q_j(\nabla_x)\tilde{e}, \quad j = 1, 2, 3,$$

$$N_{i_1, i_2, \ldots, i_k} = \partial_{x_{i_1}} \partial_{x_{i_2}} \ldots \partial_{x_{i_k}} q_{i_1, i_2, \ldots, i_k}(\nabla_x)\tilde{e}, \qquad (13)$$

$$i_1, i_2, \ldots, i_k = 1, 2, 3, \quad 2 \leq k \leq M,$$

with smooth symbols $q_{i_1, i_2, \ldots, i_k}(\xi)$, *where* $\xi \in R^d$, *of the order* $M - k$, *where* $k = 1, 2, \ldots, M$, *is the existence of the root branch* $Q(|\xi|^2)$ *of the dispersion equation for the one-dimensional diffusion system of moments of the same order* M; *i.e.,* $Q(\lambda)$ *is a function that is bounded and negative on the semiaxis* $\lambda > 0$ [$Q < 0$ *is the condition of the dissipation of projection equation* (12)] *and is such that* $Q(0) = 0$ *and* $Q'(0) < 0$. *In addition,*

$$Q(|\xi|^2) = \xi_1^2 q_1(|\xi|^2) + \xi_2^2 q_2(|\xi|^2) + \xi_3^2 q_3(|\xi|^2).$$

The system of generating functions $Q_{i_1, i_2, \ldots, i_k}(\xi) = \prod_{s=1}^{k} \xi_{i_s}^2 q_{i_1, i_2, \ldots, i_k}(\xi)$ *satisfies an analogue of system* (10) *having the only smooth solution for* $\forall |\xi| \geq 0$.

STRUCTURE OF THE CHAPMAN–ENSKOG PROJECTION FOR THE BOLTZMANN–PEIERLS EQUATION

Our investigations show that there are only two irreducible Chapman–Enskog projections: the diffusion projection of $\tilde{e}$ onto the phase space and the projection of the second sound onto the phase space of $\tilde{e}$ and p. An open question is whether the solutions of the Cauchy problem that are determined by the irreducible Chapman–Enskog projections, for example, in the one-dimensional case for the diffusion mode

$$\tilde{e}, p = p(\tilde{e}), \quad N = N(\tilde{e}), \ldots$$

and the second sound mode

$$\tilde{e}, p, N = N(\tilde{e}, p), \quad N_1 = N_1(\tilde{e}, p), \ldots,$$

are solutions of the Cauchy problem for the moment approximation of the general kinetic equation. This is a problem for future investigation. We think that this provide the ground for interesting mathematical formulations of new, undoubtedly urgent, problems.

What conclusions can be made for other kinetic equations, e.g., the Boltzmann and Fokker–Planck equations?

(i) The proposed approach is universal. Indeed, the regular asymptotic behavior implies a quantization of the moment hierarchy that enables one to formulate the operator ansatz of the Chapman–Enskog projection. The basic problems are as follows. The first problem is to describe the class of irreducible projections and, thereby, to separate the corresponding solutions of the hierarchy of moment systems that describe the basic processes of the moment approximation of the kinetic equation. The second problem is to determine to what extent the class of irreducible projections separates general solutions.

(ii) From the construction of the Chapman–Enskog projection, the cause of the instability of post-Navier–Stokes approximations (so-called ultraviolet catastrophe) is clear. Generating functions as solutions of polynomial bundles are kink functions that are poorly approximated for high frequencies by their Taylor expansion at zero.

(iii) The projection of mixed problems for moment systems onto the phase space of conservative quantities provides a mixed problem for first-order pseudodifferential hyperbolic systems with relaxation depending on conservative quantities. For such problems, correct

boundary conditions are physically meaningful, because they are expressed in terms of only conservative variables that can be determined from experimental data.

REFERENCES

1. I. Müller and T. Ruggeri, *Extended Thermodynamics* (Springer-Verlag, Berlin, 1993).
2. C. D. Levermore, J. Stat. Phys. **83**, 1021 (1996).
3. S. Chapman and T. G. Cowling, *Mathematical Theory of Nonuniform Gases* (Cambridge Univ. Press, Cambridge, 1970; Inostrannaya Literatura, Moscow, 1960).
4. R. Peierls, Ann. Phys. **3**, 1055 (1929).
5. R. A. Guver and J. A. Krumhans, Phys. Rev. **148**, 766 (1966).
6. J. Ranninger, Phys. Rev. B **5**, 3315 (1972).
7. T. Dedeurwaerdere, J. Cases-Vázquez, D. Jou, and G. Lebon, Phys. Rev. E **53**, 498 (1996).
8. W. Dreyer and H. Struchtrup, Continuum Mech. Thermodyn. **5**, 3 (1993).
9. W. Dreyer, M. Herrmann, M. Kunik, and Sh. Qamar, Preprint No. ISSN 0946-8633, WIAS (Weierstrass Institute for Applied Analysis and Stochastic, Berlin, 2003).
10. E. V. Radkevich, Contemp. Math. Fundam. Directions **3**, 5 (2003).
11. L. R. Volevich and E. V. Radkevich, Differents. Uravneniya **39** (4), 1 (2003).
12. P. A. Zakharchenko and E. V. Radkevich, Dokl. Akad. Nauk **395** (1), 36 (2004) [Dokl. Phys. **49**, 139 (2004)].
13. I. V. Karlin and A. N. Gorban, Ann. Phys. (Leipzig) **11**, 783 (2002).
14. A. V. Bobylev, Stat. Fiz. **5** (80) (1982).
15. H. Struchtrup and W. Weiss, Continuum Mech. Thermodyn. **12**, 1 (2000).

Translated by R. Tyapaev

Doklady Physics, Vol. 49, No. 8, 2004, pp. 456–461. Translated from Doklady Akademii Nauk, Vol. 397, No. 4, 2004, pp. 474–480.

TECHNICAL PHYSICS

New Method of the Synthesis of Multiband Fractal Antenna Arrays Based on a Family of Atomic Functions

V. F. Kravchenko* and V. M. Masyuk**

Presented by Academician Yu.V. Gulyaev March 5, 2004

Received March 5, 2004

INTRODUCTION

A new method of designing two-dimensional multiband antenna arrays with the application of fractal geometry is proposed. The method is based on the ideas and results presented in [1–5]. The feature of this approach is the synthesis of tunable two-dimensional multiband arrays that have the properties of the self-similarity of fractal radiation patterns with the required width of the main lobe and the preset level of side lobes in the absence of diffraction maxima in a given frequency band. The two-dimensional directional radiation pattern of self-similar fractal multiband arrays is constructed on the basis of a new class of atomic fractal functions (windows) [2]. The basic properties of variants of such windows and their efficiency are analyzed. The physical characteristics of the proposed windows are compared with those of known Blackman, Blackman–Harris, Kaiser–Bessel, and Chebyshev windows [2, 6–8].

PLANE FRACTAL ARRAYS

Let us consider an equidistant square plane fractal array. Its factor is written in the form [2, 6]

$$F(u,\nu) = \sum_{m=-N}^{M}\sum_{n=-N}^{N} I_{mn} e^{jmkd(u-u_0)} e^{jnkd(\nu-\nu_0)}, \quad (1)$$

where

$$u = \sin\theta\cos\varphi, \quad \nu = \sin\theta\sin\varphi, \quad u_0 = \sin\theta_0\cos\varphi_0,$$
$$\nu_0 = \sin\theta_0\sin\varphi_0.$$

Institute of Radio Engineering and Electronics, Russian Academy of Sciences, ul. Mokhovaya 18, Moscow, 103907 Russia

** e-mail: kr@pochta.ru*

*** e-mail: masyuk77@mail.ru*

If $I_{mn} = I_m I_n$, expression (1) for this plane array factor can be reduced to the following product of two of its linear factors:

$$F(u,\nu) = F_x(u)F_y(\nu),$$

where

$$F_x(u) = \sum_{m=-N}^{N} I_m e^{jmkd(u-u_0)}, \quad F_y(u) = \sum_{n=-N}^{N} I_n e^{jnkd(\nu-\nu_0)}.$$

For a symmetric fractal array, $I_{-m} = I_m$ and $I_{-n} = I_n$. Expressions for the directivity factor can be written as

$$F_x(u) = \sum_{m=0}^{N} \varepsilon_m I_m \cos[mkd(u-u_0)], \quad (2)$$

$$F_y(\nu) = \sum_{n=0}^{N} \varepsilon_n I_n \cos[nkd(\nu-\nu_0)]. \quad (3)$$

Thus, the sequence of self-similar plane fractal arrays is formed as was done in [6] for linear fractal arrays. The resulting directional pattern formed by this set of sequentially defined plane arrays has the form

$$F_P(u,\nu) = \sum_{p=1}^{P}\sum_{m=0}^{N}\sum_{n=0}^{N} \varepsilon_m\varepsilon_n I_{pmn}$$
$$\times \cos[mkds^{p-1}(u-u_0)]\cos[nkds^{p-1}(\nu-\nu_0)], \quad (4)$$

where

$$I_{pmn} = \left(\frac{1}{\gamma s}\right)^{p-1} I_{mn} = \left(\frac{1}{\gamma s}\right)^{p-1} I_m I_n,$$
$$I_q = \left(\frac{kd}{\pi}\right)\int_0^{\frac{\pi}{kd}} f(\omega)\cos[qkd\omega]d\omega, \quad q = m \text{ or } q = n. \quad (5)$$

This synthesis procedure provides inequidistant plane arrays that have two-dimensional fractal direc-

1028-3358/04/4908-0456$26.00

Table 1. Fourier transforms of atomic functions

Atomic function	Fourier transform
up(ω)	$I_q = \prod_{k=1}^{\infty} \frac{\sin\left(\frac{qkd\Delta}{2} \cdot 2^{-k}\right)}{\frac{qkd\Delta}{2} \cdot 2^{-k}}$
$up_m(\omega)$	$I_q(up_m) = \prod_{k=1}^{\infty} \frac{\sin^2\left(\frac{mqkd\Delta}{2}\frac{1}{(2m)^2}\right)}{\frac{mqkd\Delta}{2}\frac{1}{(2m)^k}\sin^2\left(\frac{qkd\Delta}{2}\frac{1}{(2m)^2}\right)}$ or a fast recursive algorithm of calculation of $I_q = \prod_{k=1}^{\infty} \frac{2\sin^2\left(\frac{qkd\Delta}{2} \cdot \frac{1}{2}\right)}{m\frac{qkd\Delta}{2}\sin\left(\frac{qkd\Delta}{2}\frac{1}{2m}\right)} I_q\left(\frac{q}{2m}\right)$ values
$fup_N(\omega)$	$I_q = \left(\frac{\sin\left(\frac{qkd\Delta}{2} \cdot \frac{1}{2}\right)}{\frac{qkd\Delta}{2} \cdot \frac{1}{2}}\right)^N \prod_{k=1}^{\infty} \frac{\sin\left(\frac{qkd\Delta}{2} \cdot 2^{-k}\right)}{\frac{qkd\Delta}{2} \cdot 2^{-k}}$
$\Xi_n(\omega)$	$I_q = \prod_{k=1}^{\infty}\left(\frac{\sin\frac{qkd\Delta}{2}(n+1)^{-k}}{\frac{qkd\Delta}{2}(n+1)^{-k}}\right)^n$
$g_k(\omega)$	$I_q = \prod_{j=1}^{\infty} \frac{\frac{k^2}{1-\cos(2k/3)}\left[\cos(qkd\Delta \cdot 3^{-j}) - \cos\frac{2k}{3}\right]}{k^2 - \left(\frac{qkd\Delta}{2}\right)^2 \cdot 9^{1-j}}$
$g_{k,h}(\omega)$	$I_q = \prod_{j}^{\infty} \frac{\frac{k^2}{1-\cos(2kh/3)}\left[\cos(qkd\Delta \cdot 3^{-j}) - \cos\frac{2kh}{3}\right]}{k^2 - \left(qkd\Delta \cdot \frac{1}{2}\right)^2 \cdot 9^{1-j}}$
$h_a(\omega)$	$I_q = \prod_{k=1}^{\infty} \frac{\sin\left(\frac{qkd\Delta}{2}a^{-k}\right)}{a \cdot 2^{-k}}$

tional radiation patterns and are based on the construction of generator functions $f(\omega)$.

SYNTHESIS OF FRACTAL ARRAYS WITH NEW WEIGHT FUNCTIONS (WINDOWS)

We consider the method of synthesizing fractal directional radiation patterns with weight functions (windows) whose proper choice can provide multiband sparse arrays of minimal physical size. The following requirements are imposed on window functions: the low level of side lobes and fast spectral transform. The advantage of such functions is that, when they are used to synthesize the directional patterns of antennas, the further currents of elements decrease rapidly with the distance from the center. Due to this property, effective rarefaction methods can be developed, which can be applied to significantly reduce the number of elements and the physical size of resulting arrays. A wide class of weight functions (windows, see Table 1) proposed and justified in [2] satisfies these criteria. We analyze the following types of weight functions (windows, see Tables 2 and 3): square, Blackman, Blackman–Harris, Kaiser–Bessel, Chebyshev, Kravchenko, Kravchenko–

Table 2. Basic physical parameters of new Kravchenko windows and classical windows

Weight functions (windows)	Equivalent noise band, bin	Correlation between overlapping sections (50% overlapping), %	Scalloping loss, dB	Maximum transform losses, dB	Maximum side-lobe level, dB	6-dB-level band, bin	Coherent amplification
Classical window functions							
Square	1.0000	50.0000	3.9210	3.9210	–13.2660	2.4064	1.0000
Blackman	1.7620	8.0396	1.0550	3.5151	–58.1156	4.6123	0.4116
Four-term Blackman–Harris	2.0044	3.7602	0.8256	3.8453	–98.7893	5.2139	0.3588
Chebyshev	1.6572	11.0562	1.1978	3.3916	–70.0002	4.2112	0.4375
Kaiser–Bessel $a = 3$, $\Delta = \frac{2}{3}$	1.8385	16.4114	0.9751	3.6198	–70.0117	4.8128	0.3930
Kravchenko windows							
Kravchenko $g_4(x)$up(x), $\Delta = 1.1$	1.8718	4.1630	0.9194	3.6421	–17.1507	4.8128	0.3916
Kravchenko $h_{2.5}(x)$, $\Delta = 1.1$	2.1378	0.6894	0.6883	3.9879	–19.0105	5.4145	0.5000
Kravchenko $g_{2.9}(x)$, $\Delta = 1$	1.6919	9.1688	1.1055	3.3893	–22.6008	4.4118	0.500
Kravchenko $g_{2.5}(x)$, $\Delta = 1.1$	1.7404	7.8201	1.0462	3.4527	–25.5553	4.4118	0.5000
Kravchenko $g_2(x)$, $\Delta = 1$	1.7939	6.6272	0.9896	3.5276	–29.8546	4.6123	0.5000
Kravchenko $g_{2.8}^2(x)$, $\Delta = 1$	2.1839	1.2173	0.6689	4.0612	–29.9830	5.6150	0.4351
Kravchenko Ξ_2, $\Delta = 1$	1.8947	4.9477	0.9005	3.6759	–34.0299	4.8128	0.5000
Kravchenko–Bernstein fup$_2(x)$Br$^2(x)$, $\Delta = 1$	1.7393	8.5152	1.0775	3.4812	–45.7415	4.4118	0.4203
Kravchenko–Gauss (fup$_2(x)$G$(2, x)$)	1.5327	15.6455	1.4128	3.2673	–46.2344	2.0213	0.4675
Kravchenko $\text{fup}_2^4(x)$, $\Delta = 0.86$	1.9861	4.2488	0.8517	3.8318	–51.5653	5.0134	0.3610
Kravchenko Ξ_4, $\Delta = 1$	2.3517	0.9064	0.5972	4.3111	–57.9777	6.0161	0.5000
Kravchenko–Chebyshev fup$_4(x)$Cheb$(3, x)$	1.6932	10.1129	1.1569	3.4441	–65.4653	2.2234	0.4248
Kravchenko–Gauss (fup$_2(x)$G$(3, x)$, $\Delta = 1$	1.9643	4.7297	0.8781	3.8101	–68.8390	2.6276	0.3614
Kravchenko $\Xi_7(x)$, $\Delta = 1$	2.9010	0.0754	0.3974	5.0228	–96.0956	7.4198	0.5000

Gauss, Kravchenko–Kaiser, and Kravchenko–Chebyshev. According to [2], the Fourier transforms of atomic functions are known in an explicit form. Excitation currents I_{pmn} for a plane array can be easily calculated by expressions given in Table 1. Analysis of the physical results (Tables 2 and 3) shows that weight functions (windows) differ from each other in the main-lobe width and level of side lobes. It is worth noting that correlation between overlapping sections, as well as maximum transformation losses, strongly affects the synthesis of a fractal directional pattern. The quality of the separation of bands depends on the rate of decreasing side lobes. In contrast to classical windows (Blackman, Blackman–Harris, Kaiser–Bessel, Chebyshev), Kravchenko weight functions (windows) have an infinite decreasing rate due to the properties of atomic functions [2]. This behavior makes it possible to weaken side lobes at the edges of the fractal antenna and to reduce the mutual effect of neighboring frequencies.

NUMERICAL EXPERIMENT

Effect of the Level of Side Lobes on the Directional Radiation Pattern

Figure 1 exemplifies a synthesized directional radiation pattern for the Kravchenko window [based on the convolution $\Xi_3(\omega) \cdot \Xi_3(\omega)$] with a side-lobe level of –91 dB for a plane four-band fractal array ($s = 3$). Figure 1 shows the directional radiation pattern for the upper frequency band. For comparison, we present another Kravchenko window ($g_{2.5}$) with a side-lobe

level of –25.5 dB (Tables 2 and 3). The experimental parameters—$N = 45$, $s = 3$, $P = 4$, $\Delta = 1$, and $\gamma = 4$—were identical for both cases.

According to Fig. 1 and Tables 2 and 3, when a window with the high relative level of side lobes is used, the radiation of elements from high-level subarrays ($P = 3$ and 4) is disguised by the side lobes of low-level subarrays ($P = 1$ and 2). In this case, the self-similar structure of the radiation characteristic is distorted. This effect prevents the synthesis of multiband fractal arrays with numerous bands. Analysis of the application of other weight functions with various levels of side lobes, various widths of the mean beam, and various correlation levels of overlapping sections shows that Kravchenko windows having an infinite rate of decreasing side lobes are preferable. They provide arrays with numerous bands (Fig. 1). The unique properties of new windows make it possible to widely vary the parameter Δ, which simplifies the synthesis of the fractal directional pattern.

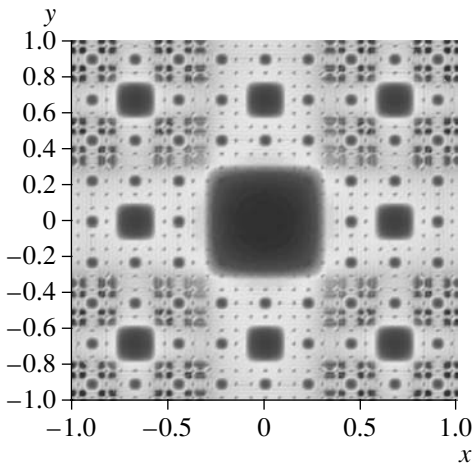

Fig. 1. Directional pattern (contour map) of a fractal antenna array for the Kravchenko window $\Xi_3(\omega) \cdot \Xi_3(\omega)$.

Band Switching Scheme

Let us analyze an algorithm developed according to [6] and atomic function theory [2], where a band-switching scheme for fractal arrays is important. According to [6], the problem of multiband arrays is that the switch from the highest band to the lowest one significantly worsens their physical parameters. This is associated with the fact that the relative intervals between array elements are different for different bands. In particular, Werner *et al.* [6] analyzed a fractal array with four bands and Lamé coefficient $s = 3$. Let the minimum distance between its elements be $d_0 = \frac{\lambda_0}{2}$ for the highest frequency band ($f = f_0$). For the next band $\left(f = f_1 = \frac{f_0}{3} \right)$, the minimum distance between elements $d_1 = \frac{\lambda_1}{6}$. Similarly, for the third $\left(f = f_2 = \frac{f_0}{9} \right)$ and fourth $\left(f = f_3 = \frac{f_0}{27} \right)$ bands, $d_2 = \frac{\lambda_2}{18}$ and $d_3 = \frac{\lambda_3}{54}$, respectively. As is seen (in practice), significant correlation due to the closeness of elements, particularly in

Table 3. New convolution-based Kravchenko windows

Weight functions (windows)	Equivalent noise band, bin	Correlation between overlapping sections (50% overlapping), %	Scalloping loss, dB	Maximum transform losses, dB	Maximum side-lobe level, dB	6-dB-level band, bin	Coherent amplification
Kravchenko $g_{3,\,h=5}(x) \cdot \mathrm{kaiser}(x)$, $\Delta = 1$	1.6054	12.2874	1.2346	3.2904	–24.0945	4.4118	0.4923
Kravchenko $g_4(x) \cdot \mathrm{kaiser}(x)$, $\Delta = 1.15$	2.2129	1.3960	0.6637	4.1133	–36.0898	6.0161	0.3353
Kravchenko–Chebyshev $\mathrm{fup}_4(x) \cdot \mathrm{Cheb}(3, x)$	1.7621	7.6239	1.0367	3.5131	–36.0002	4.6122	0.419
Kravchenko $g_{3,\,h=1}(x) \cdot \Xi_2(x)$, $\Delta = 1$	2.3681	0.7595	0.5846	4.3286	–49.3037	6.4171	0.3068
Kravchenko–Kaiser $g_{4,\,h=6}(x) \cdot k(x)$, $\Delta = 1$	1.9432	4.7094	0.8813	3.7664	–53.3040	5.2139	0.3706
Kravchenko–Kaiser $g_2(x) \cdot k(x)$, $\Delta = 1.15$	2.4348	0.6683	0.5596	4.4242	–62.8746	6.6177	0.2965
Kravchenko–Kaiser $h_{2.5}(x) \cdot k(x)$, $\Delta = 1.15$	2.6448	0.2193	0.4725	4.6965	–60.6313	7.2193	0.2737
Kravchenko $\Xi_3(x) \cdot \Xi_3(x)$	2.8294	0.1073	0.4172	4.9342	–91.4690	7.6203	0.2528
Kravchenko–Kaiser $\Xi_4(x) \cdot k(x)$, $\Delta = 1.15$	2.7361	0.1870	0.4472	4.8184	–104.5104	7.4198	0.2623

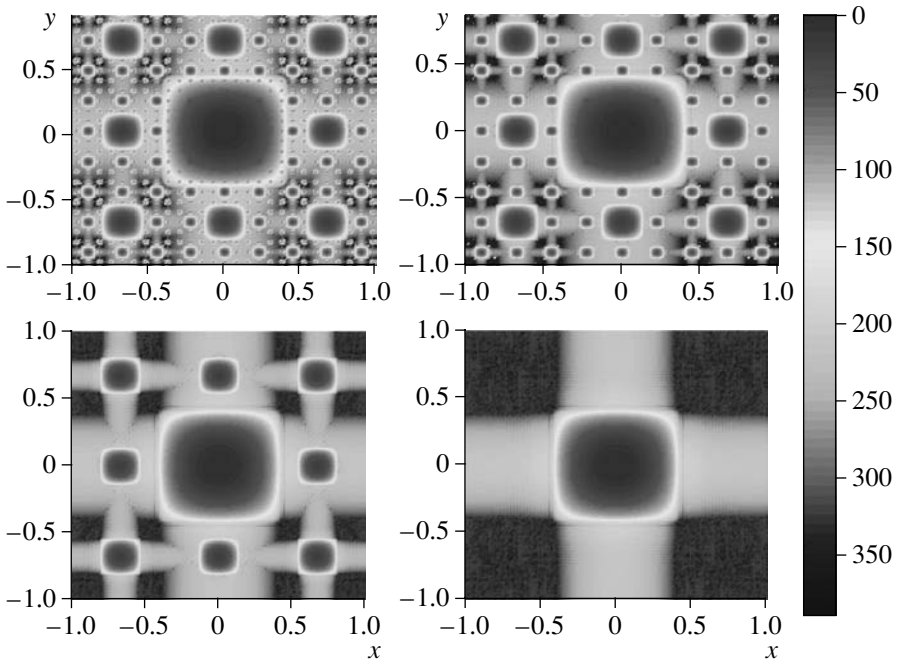

Fig. 2. Contour map of the directional pattern of a four-band fractal antenna array for the Kravchenko window $\Xi_7(\omega)$.

the lowest frequency band, is inherent in such fractal arrays. To overcome this problem, a band switching scheme implying the step-by-step turning off of higher frequency subbeams is introduced in [6] and in this work. The unique properties of the self-similarity of fractal arrays under study are used to physically realize such an approach. In this case, it is necessary to use the minimum number of elements that are turned on or off when bands are switched. Therefore, the method of designing a multiband array begins with the choice of the corresponding coefficient s and the necessary number P of frequency bands. The centers of individual bands of the fractal array are located at

$$f_0, \frac{f_0}{s}, \frac{f_0}{s^2}, \ldots, \frac{f_0}{s^{P-1}}.$$

For the highest frequency band ($f = f_0$), all subarrays are excited. When the array is switched to the second band $\left(f = \frac{f_0}{s}\right)$, the first subarray ($P = 1$) is turned off. When the array is switched to the third band $\left(f = \frac{f_0}{s^2}\right)$, the first and second subarrays ($P = 1$ and 2) are turned off. This process is repeated to the lowest frequency band $\left(f = \frac{f_0}{s^{P-1}}\right)$. In this case, all subarrays, except the last channel, are turned off. Let us apply the method of synthesizing a multiband directional radiation pattern based on Kravchenko weight functions [2] to particular examples. Let it be required to synthesize a multiband fractal array with band central frequencies f_0, $\frac{f_0}{3}$, $\frac{f_0}{9}$, and $\frac{f_0}{27}$. In this case, the Lamé coefficient $\Xi_7(\omega)$, and the number of given bands is equal to $P = 4$. The chosen Kravchenko window based on the function $\Xi_7(\omega)$ ensures a side-lobe level of –96 dB. For this window and $\Delta = 1$, the width of the beam for one cascade is no more than 11.8° at a level of –3 dB. The width of the beam depends on the number of bands and band number. However, for $\gamma s > 6$–10, further cascades introduce insignificant changes into the characteristics of the main lobe. For all further calculations, we take $\gamma = 4$, for which the level of the main lobe of the next cascade with respect to the preceding one is equal to –21.6 dB. In practice, due to the effect of side lobes and the finite number of elements of the fractal antenna array, the value is rather lower and lies from –16 to –20 dB. The taken value $\gamma = 4$ is convenient for analysis, because the side-lobe level of the last cascade with respect to the first one is equal to –80 dB for $P = 4$. The interval between elements in highest frequency band of the array ($f = f_0$) is equal to $d_0 = \frac{\lambda_0}{2}$. Figure 2 shows the contours of the directional pattern for each band. Such switching scheme provides the half-wavelength interval between the active elements of the fractal array.

Array Rarefaction Algorithm

The properties of weight functions used to synthesize self-similar fractal directional radiation patterns can be used to construct rarefaction algorithms. Such a procedure includes the minimization of the size of the antenna array and reduction of the number of its elements. We consider the stages of a rarefaction algorithm used for multiband fractal arrays of the types under consideration. It follows from Eq. (4) that inequidistant fractal arrays can be aligned in a string consisting of P equidistant subarrays with equivalent current distributions. The rarefaction algorithm is applicable to each subarray. In this case, the self-similarity properties of subarrays remain. This is a feature of the method. The algorithm is organized as follows. Currents of elements on each of P subarrays are normalized such that their values smaller than the preset value ε vanish. Then, the constructed subarrays are summarized to obtain a sparse fractal multiband array. The choice of the parameter ε for each particular case is individually determined by a compromise between the accuracy of the synthesized directional radiation pattern and physical sizes (number of elements) of the array. Typical ε values considered in [6] and in this work lie in the range 0–20%. For $\varepsilon \longrightarrow 20\%$, fractal arrays with fewer elements are obtained. In this case, synthesized arrays have maximum errors.

As an example, we consider the synthesis of the directional pattern of the fractal antenna array with the use of the Kravchenko window $\Xi_7(\omega)$. The synthesized fractal array consists of four 91×91 subarrays ($N = 45$). The resulting fractal multiband plane array has 26272 elements. Applying the rarefaction procedure when choosing different ε values, the number of elements can be considerably reduced to 2176 with some distortions. The number of elements can be reduced to 662 with a loss of the accuracy of the directional pattern. Figure 3 shows the diagonal section of the directional pattern (over the $x = y$ straight line in the xy plane) of the sparse array ($N = 816$ and $\varepsilon = 10\%$) with four bands. The rarefaction procedure makes it possible to synthesize arrays with large numbers of side lobes and noticeable distortions in subarrays for the maximum band. However, the characteristics of the main beam, as well as the maximum level of side lobes, change slightly.

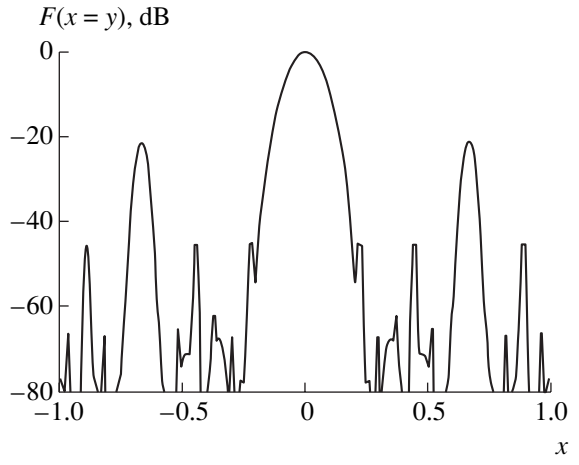

Fig. 3. Section of the directional pattern over the $x = y$ straight line in the xy plane for a sparse array based on the Kravchenko window $\Xi_7(\omega)$ for $D = 816$ and $\varepsilon = 10\%$.

CONCLUSIONS

A new method of designing multiband arrays based on the synthesis of fractal directional patterns has been proposed and justified. New synthesized Kravchenko windows constructed on the basis of the theory of atomic functions whose Fourier transforms can be obtained in an explicit form and that have a low level of side lobes upon insignificant losses of the transform was shown to be preferable over the known transforms. This approach can be applied to the development of a new type of multiband fractal antenna arrays. The results were reported in part in the 4th International Conference on Theory and Engineering of Antennas [10].

ACKNOWLEDGMENTS

We are grateful to Academician Yu.V. Gulyaev, Corresponding Members of the RAS L.D. Bakhrakh and V.I. Pustovoĭt, and Prof. Ya.S. Shifrin for stimulating discussions.

REFERENCES

1. V. F. Kravchenko, Dokl. Akad. Nauk **386** (1), 754 (2002) [Dokl. Phys. **47**, 605 (2002)].
2. V. F. Kravchenko and V. M. Masyuk, Antenny, No. 10 (65), 3 (2002).
3. V. F. Kravchenko, in *Lectures on Atomic Function Theory and Applications* (Radiotekhnika, Moscow, 2003).
4. V. F. Kravchenko and M. A. Basarab, *Boolean Algebra and Approximation Methods in Boundary Problems of Electrodynamics* (Fizmatlit, Moscow, 2004).
5. V. M. Masyuk, Electromagn. Waves Electron. Syst. **7** (9), 26 (2003).
6. D. H. Werner, M. A. Gingrich, and P. L. Werner, IEEE Trans. Antennas Propag. **51**, 1486 (2003).
7. E. Ya. Remez, *General Methods of Chebyshev Approximation* (Izd. Akad. Nauk USSR, Kiev, 1957).
8. L. R. Rabiner and B. Gold, *Theory and Application of Digital Signal Processing* (Prentice-Hall, Englewood Cliffs, New York, 1975).
9. V. F. Kravchenko, in *Proceedings of the 4th International Conference on Antenna Theory and Techniques, Sevastopol, 2003*, Vol. 1, pp. 183–189.
10. V. M. Masyuk, in *Proceedings of the 4th International Conference on Antenna Theory and Techniques, Sevastopol, 2003*, Vol. 1, pp. 220–223.

Translated by R. Tyapaev

Doklady Physics, Vol. 49, No. 8, 2004, pp. 462–465. Translated from Doklady Akademii Nauk, Vol. 397, No. 5, 2004, pp. 615–618.

TECHNICAL PHYSICS

A New Method for Self-Compensation of Radar-Pulse Distortions in the P–VHF Bands for Space Synthetic Aperture Radars

O. V. Goryachkin

Presented by Academician Yu.V. Gulyaev March 18, 2004

Received March 18, 2004

INTRODUCTION

Problems of implementing space synthetic aperture radars (SARs) for remote sounding of the Earth's surface that operate in frequency bands unused so far in space radar have been discussed in the last few years. These SARs operate in the upper part of the decimeter band and in meter (i.e., P, UHF, and VHF) bands. The necessity of installing such SARs aboard spacecrafts is currently due to diversified practical needs associated with radar cartography and geodesy, subsurface sounding, and various business applications of sounding of the Earth's surface.

However, a number of factors prevent the space installation of SARs operating in the P band and, especially, in the VHF band [1–6]. One of the basic factors is significant distortions of a SAR sounding signal in the atmosphere due to the altitude dependence of the refraction index in the troposphere and ionosphere, as well as to polarization dispersion [1, 2].

One of the most promising methods of overcoming the consequences of these effects is the compensation of distortions in the process of autofocusing radar images [5]. However, well-known autofocusing algorithms stably operate only with radar-image fragments containing bright point targets. In this study, a method for the self-compensation of radar-image distortions in SARs is proposed. The method is based on the direct extraction of the SAR sounding signal, which is distorted by the effect of the propagation medium or processing channel, from a radio hologram. Furthermore, the extracted signal is used in the processing procedure for determining the distance to the signal source. In this case, the quality of the algorithm is independent of the radar-image content.

Volga State Academy of Telecommunication and Informatics, ul. L'va Tolstogo 23, Samara, 443010 Russia
e-mail: gor@mail.radiant.ru

A MODEL OF A REFLECTED SIGNAL OF THE SPACE SAR

The reflected signal of the space SAR can be written as

$$\dot{S}(t, kT) = \iint \dot{K}_A(kT, \theta, \sigma)\dot{K}_R(t - \Delta t(kT - \theta, \sigma)) \times \dot{\xi}(\theta, \sigma) g_R(\sigma) g_A(kT - \theta, \sigma) d\theta d\sigma + \dot{v}(t, kT). \quad (1)$$

Here,

$$\dot{K}_R(t) = \frac{1}{2\pi}\int_{-\infty}^{\infty} \dot{h}(j\omega)\dot{K}_a(j\omega)\dot{K}_h(j\omega)\exp(j\omega t)d\omega,$$

$$\dot{K}_A(kT, \theta, \sigma) = \exp(j\omega_0(\Delta t(kT - \theta, \sigma) + \delta(kT, \theta, \sigma))),$$

$\dot{\xi}(\theta, \sigma)$ is the reflection coefficient of the underlying surface; $\dot{h}(j\omega)$ is the complex envelope of the sounding signal; $\dot{K}_a(j\omega)$ describes the refraction of the sounding signal in the regular atmosphere; $\dot{K}_h(j\omega)$ is the transfer characteristic of the processing channel; $\Delta t(kT - \theta, \sigma)$ is the regular part of the signal time delay in the atmosphere; $\delta(kT, \theta, \sigma)$ is the fluctuation component of the signal time delay in the turbulent atmosphere; t and kT are coordinates (the time delay and sounding-signal number); θ and σ are the time coordinates of an underlying-surface element (its azimuth and distance); and g_A and g_R are the real functions describing signal modulation due to the antenna directivity pattern of the SAR. This model includes all major effects resulting in distortions of a radar signal propagating through the Earth's atmosphere. In particular, distortions arising in the process of the propagation of broadband signals through the Earth's atmosphere are described by the transfer function $\dot{K}_a(j\omega)$. Problems associated with both this effect and the transfer-function model were discussed in [1, 2]. Due to the effect of dispersion distortions in the propagation medium on the distance res-

1028-3358/04/4908-0462$26.00 © 2004 MAIK "Nauka/Interperiodica"

olution of SARs using broadband signals, the shape of the reflected pulse differs from the expected one. Therefore, in the case of the optimal reception of such a signal, the duration of the convolution defining the distance resolution increases at the output of a matched filter. Since $\tau = \Delta t(kT - \theta, \sigma)$ is a monotonic function of the variable σ within the existence interval, employing formula (1) and the corresponding substitution of variables, we obtain the model of the SAR signal in the form

$$\dot{S}(t, k) = \int \dot{K}_R(t - \tau)\dot{\eta}(\tau, k)d\tau + \dot{v}(t, k), \qquad (2)$$

where

$$\dot{\eta}(\tau, k) = \int \dot{K}_A(kT, \theta, \Delta t^{-1}(kT - \theta, \tau)) \times \dot{\xi}(\theta, \Delta t^{-1}(kT - \theta, \tau)) \times g_A(kT - \theta, \Delta t^{-1}(kT - \theta, \tau)) \times g_R(\Delta t^{-1}(kT - \theta, \tau))\frac{\partial}{\partial \tau}\Delta t^{-1}(kT - \theta, \tau)d\theta.$$

Since $\dot{\xi}(\theta, \sigma)$ is usually described by the model of complex white noise, the quantity $\dot{\eta}(\tau, k)$ describes a complex unsteady random Gaussian process with the zero expectation and correlation function $B_\eta(\tau_1, \tau_2, k_1, k_2)$. The function $\tau = \Delta t(kT - \theta, \sigma)$ is monotonic, and the observed signal is steady in the azimuth cross section, which is typical of a normal SAR. Using these properties, one can show that, if $k = 0, 1, \ldots, N - 1$ and $N \ll N_s$ (where N_s is the interval of the aperture synthesis in readings), $\dot{\eta}(\tau, k)$ may be considered as independent realizations of a random complex Gaussian process with unsteady dispersion.

AN ALGORITHM FOR COMPENSATING DISTORTIONS OF AN SAR SOUNDING PULSE

The problem of compensating distortions of an SAR sounding pulse should be considered in the following sequence. At the first stage, the SAR radio hologram is used to estimate the pulse characteristic $\dot{K}_R(t)$ of the distant channel. At the second stage, the function $\dot{\eta}(\tau, k)$ is reconstructed. Depending on the type of distortions, the latter problem can be treated as the ill-posed problem of inverting integral convolution operator (2) and may be solved by choosing a certain regularization strategy. If there exist sounding-pulse distortions caused by the frequency dependence of the atmosphere refraction index, i.e., phase distortions, then the second-stage problem can be more correctly considered either as the problem of the resolution of reflected pulses in pulse delay or as the problem of pulse compression. In this case, the optimal processing algorithm is the correlated filtration algorithm, where the first-stage estimate of the sounding pulse is used as a reference signal. Then, denoting $\dot{h}(t) = \dot{K}_R(t)$, one can write the observed realizations of a random process $\dot{S}(t, k)$ in the form of the stochastic integral

$$\dot{S}(t) = \int_{-\infty}^{+\infty} \dot{h}(t - \tau)g_R(\tau)d\dot{\zeta}(\tau) + \dot{v}(t).$$

Here, $\dot{x}'(\tau) = d\dot{\zeta}(\tau)$ is standard complex white noise with zero mathematical expectation and unit dispersion and $\dot{\eta}(\tau) = g_R(\tau)\dot{x}'(\tau)$ is the random process with unsteady dispersion. In this case, the correlation function of the random process $\dot{S}(t)$ is of the form

$$B_S(t_1, t_2) = \mathbf{M}\{\dot{S}(t_1)S^*(t_2)\} = \int_{-\infty}^{+\infty} h(t_1 - \tau)h^*(t_2 - \tau)g_R^2(\tau)d\tau + \frac{N_0}{2}\delta(t_2 - t_1).$$

The two-dimensional Fourier transform $B_S(\omega_1, \omega_2)$ of the correlation function $B_S(t_1, t_2)$ satisfies the equality

$$B_S(\omega_1, -\omega_2) = \frac{N_0}{2}\delta(\omega_1 - \omega_2) - \dot{H}(\omega_1)H^*(\omega_2)B_x(\omega_1 - \omega_2), \qquad (3)$$

$$B_x(\omega_1 - \omega_2) = \int_{-\infty}^{+\infty} g_R^2(\tau)e^{-j(\omega_1 - \omega_2)\tau}d\tau,$$

where $\dot{H}(\omega_1)$ is the transfer function of the SAR distant channel, which is described by Eq. (2). Let us write Eq. (3) in the form of the separate equalities for the modulus and phase of the function $B_S(\omega_1, \omega_2)$:

$$\left|B_S(\omega_1, -\omega_2) - \frac{N_0}{2}\delta(\omega_1 - \omega_2)\right| = \left|\dot{H}(\omega_1)\right|\left|\dot{H}(\omega_2)\right|\left|B_x(\omega_1 - \omega_2)\right|,$$

$$\arg\left(B_S(\omega_1, -\omega_2) - \frac{N_0}{2}\delta(\omega_1 - \omega_2)\right) = \arg(\dot{H}(\omega_1)) - \arg(\dot{H}(\omega_2)) + \arg(B_x(\omega_1 - \omega_2)).$$

Fixing the difference $\omega_1 - \omega_2$, we arrive at the equations for the modulus and phase of the transfer function

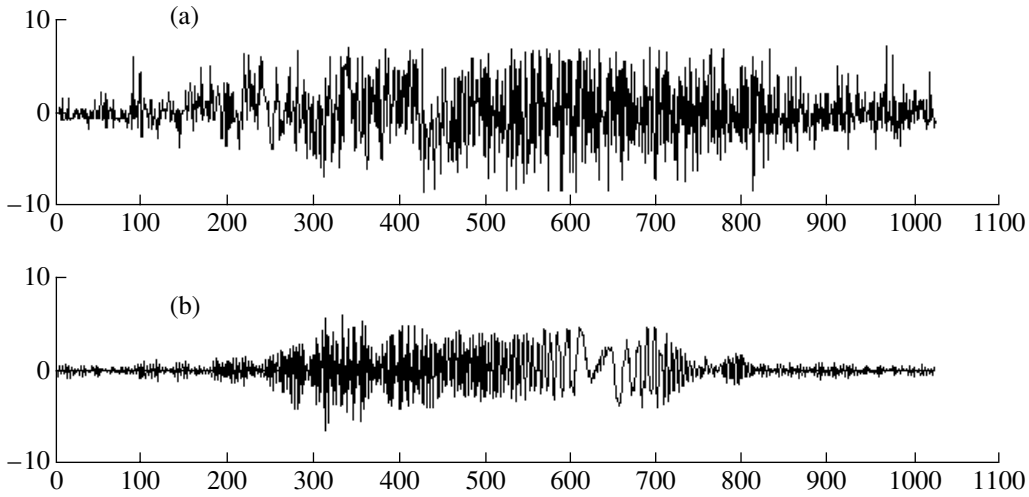

Fig. 1. Example of the reconstruction of a sounding pulse by using reflected SAR signals of the X band: (a) digital readings of an SAR signal reflected from the Earth's surface and (b) digital readings of an SAR sounding pulse reconstructed by using reflected signals.

for the SAR distant channel. These equations determine this function except for a complex factor and a certain constant time shift. For finite-length discrete sequences, the estimation algorithm for the transfer function of the SAR distant channel can be written as

$$\hat{\dot{H}}\left(\frac{m}{T}\right) = \sqrt{\left|\hat{B}_S\left(\frac{m}{T}, \frac{-m}{T}\right) - \frac{N_0}{2}\right|} \times \exp\left(j\left(\sum_{i=0}^{m} \arg\left(\hat{B}_S\left(\frac{i}{T}, \frac{i+1}{T}\right)\right)\right)\right). \quad (4)$$

Here, $m = 0, 1, \ldots, M-1$; M is the length of the discrete Fourier transform; T is the repetition period of sounding pulses; and $\hat{B}_S(\omega_1, \omega_2)$ is the sample estimate of the covariance function, which is based on N reflected pulses. As a whole, the algorithm demonstrates good noise stability, but it requires a rather high degree of unsteadiness. For a space SAR, this implies that it is necessary to take into account an additional constraint for the capture band when realizing the algorithm. This disadvantage can be compensated by increasing the number of processed realizations. A significant advantage of the algorithm (e.g., in contrast to [5]) is the independence of radar-image features (in particular, the existence of bright points in the focusing zone). In addition, the algorithm does not require *a priori* knowledge of the function g_R. To overcome the sensitivity of the algorithm to nonlinear distortions in the SAR circuit, which are caused by the low-digital signal quantization, the following correlation between the covariance function of a signal passed through an ideal limiter and that of the initial signal can be used:

$$B_S(t_1, t_2) = \Omega(t_1)\Omega(t_2)\left(\left(\sin\left(\frac{\pi}{2}r_{xx}(t_1, t_2)\right) + \sin\left(\frac{\pi}{2}r_{yy}(t_1, t_2)\right)\right) + j\left(\sin\left(\frac{\pi}{2}r_{xy}(t_1, t_2)\right) - \sin\left(\frac{\pi}{2}r_{yx}(t_1, t_2)\right)\right)\right).$$

Here, r_{xx}, r_{yy}, r_{xy}, and r_{yx} are the correlation factors of the sign sequence for the initial hologram; $\Omega(t)$ is the averaged (over the realizations) amplitude of the reflected signal in the time region under consideration; and $B_S(t_1, t_2)$ is the desired covariance function. In order to decrease the side-lobe level, novel time windows synthesized in [7] can be applied. The experimental verification of the possibility of using the algorithm to correct distortions of the SAR distant channel by utilizing information obtained with an aviation SAR operating in the X band yielded promising results. An example of reconstructing a linear frequency-modulated SAR sounding pulse by processing 1000 reflected signals is shown in Fig. 1.

Thus, the proposed method for estimating an SAR sounding signal distorted in the ionosphere reliably compensates the given effect independently of SAR image features. The application of the method provides for the realization of high-resolution radar space sys-

tems of the Earth's distant sounding in the P–VHF bands.

REFERENCES

1. N. V. Kretov, T. E. Ryzhkina, and L. V. Fedorova, Radiotekh. Élektron. (Moscow) **37**, 90 (1992).
2. N. V. Kretov, T. E. Ryzhkina, and L. V. Fedorova, Radiotekh. Élektron. (Moscow) **36**, 1 (1991).
3. O. V. Goryachkin, Komp'yuternaya Optika, No. 24, 177 (2002).
4. A. I. Efimov, A. A. Kalinkevich, and B. G. Kutuza, Radiotekhnika, No. 2, 19 (1998).
5. V. B. Shteĭnshleĭger, A. V. Dzenkevich, V. Yu. Manakov, *et al.*, Radiotekh. Élektron. (Moscow) **42**, 725 (1997).
6. A. Ishimaru, Y. Kuga, J. Liu, *et al.*, Radio Sci. **34**, 257 (1999).
7. V. F. Kravchenko, in *Lectures on Theory and Applications of Atomic Functions* (Radiotekhnika, Moscow, 2003).

Translated by G. Merzon

Doklady Physics, Vol. 49, No. 8, 2004, pp. 466–470. Translated from Doklady Akademii Nauk, Vol. 397, No. 6, 2004, pp. 767–771.

TECHNICAL PHYSICS

Investigation of the Electrophysical Properties of the Combustion Products of Hydrogen in Oxygen with Alkali Metal Additions

Academician E. P. Velikhov[1], Yu. G. Degtev[2], V. P. Panchenko[2,*], A. G. Blokh[3], V. V. Kovalenko[3], B. G. Tkachenko[3], E. P. Seleznev[4], M. I. Goldovskiĭ[4], and A. G. Galeev[5]

Received April 16, 2004

1. Search for and creation of new plasma-forming fuels for MHD energy converters are aimed at improving their characteristics and extending their functional capabilities and application domains [1, 2]. Among them is the hydrogen–oxygen fuel, treated as the basic product of hydrogen power industry [3]. In view of these circumstances and due to their features, this fuel is attracting increased attention in power generation and plasma aerospace applications [3–5]. However, when creating technical devices, the basic problem is the achievement of electric conductivity σ close to the ideal calculated value. This problem is associated with its strong dependence on temperature, composition, and other factors.

The properties of the combustion products of the hydrogen–oxygen fuel are numerically examined in the thermodynamic equilibrium approximation by a method and a software package presented in [6]. The oxidant excess coefficient α varied from 0.6 to 1.1; the mass fraction of alkali metal addition g in hydrogen, from 0.3 to 0.9; its molar fraction in the fuel, from 0.7 to 5%; the pressure p_c in the combustion chamber of the plasma generator, from 2 to 10 MPa; the expansion degree in a nozzle was up to a Mach number of 3.2; and the hydrogen temperature T_h at the entry of the plasma generator varied from 300 to 1200 K.

This investigation showed that the temperature in the combustion chamber is equal to $T_c \approx 3600$ K for p_c = 4.5 MPa and T_h = 300 K and optimum $\alpha \approx 0.9$. In this case, the maximum value σv^2 (v is the velocity) reaches (for Cs) 170 and (for K) 95 S/m (km/s)^2 when the flow expands to M ≈ 2.5, the respective σ values are equal to 20 and 12 S/m, and the electron mobility values μ_e are equal to 0.1 and 0.09 T^{-1}, respectively. An increase in pressure in the combustion chamber from 1 to 7 MPa in the range M ≈ 2.5 reduces σ and σv^2 by one-third. The optimum g value depends on the type of addition and is equal to about 0.8 and 0.5 for cesium and potassium, respectively. Deviations from the optimum g values by ±10% change σ and σv^2 by 20%. An increase in the hydrogen temperature at the entry of the combustion chamber from 300 to 1200 K increases σ and σv^2 by a factor of 1.8.

2. At the first stage, the conductivity of the combustion products of the hydrogen–oxygen fuel with Cs and KNa-eutectic additions was experimentally studied on a model device (Fig. 1). The 390-mm-long gasdynamic section of the device includes a water-cooled plasma generator with a 150-mm-long cylindrical combustion chamber (*3*) 65 mm in diameter on whose atomizer head (*2*) 18 three-component atomizers are placed. The addition was supplied in liquid form. A supersonic nozzle (*4*) 100 mm in length had a critical cross section with a diameter of 17.4 mm, which ensured the rate $\dot{m}$ = 0.3–0.9 kg/s of combustion products and heat power up to 7 MW for p_c = 2–6 MPa, as well as the acceleration of the flow up to the Mach number M ≈ 2.4 for an outlet cross-section diameter of 30 mm.

The σ values were primarily measured by a passage-type inductive sensor (*6*) (measurement error ≤12%) [7] with a 140-mm-long measuring channel (*5*) with a diameter of 31 mm at the entry and 32 mm at the exit.

[1] *Russian Research Centre Kurchatov Institute, pl. Akademika Kurchatova 1, Moscow, 123182 Russia*

[2] *Troitsk Institute for Innovation and Thermonuclear Research, Troitsk, Moscow oblast, 142092 Russia*

[3] *OAO Nizhni Novgorod Machine Building Factory, Sormovskoe sh. 21, Nizhni Novgorod, 603052 Russia*

[4] *Design Office of Chemical Machine Building, ul. Bogomolova 12, Korolev, Moscow oblast, 141070 Russia*

[5] *Research Institute of Chemical Machine Building, Sergiev Posad, Moscow oblast, 141300 Russia*

* *e-mail: panvic@triniti.ru*

1028-3358/04/4908-0466$26.00

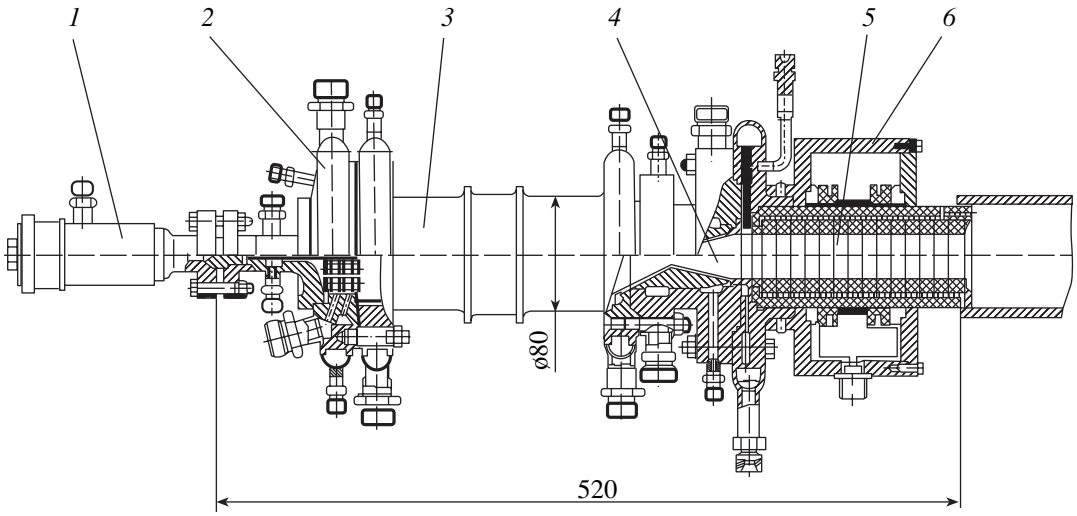

Fig. 1. Layout of the model device.

The probe technique (measurement error ≤15%) was used in some experiments.

Figure 2 shows experimental and calculated results for σ values of the combustion products of the hydrogen–oxygen fuel with cesium addition for p_c = 4.5 MPa. Table 1 presents the electrophysical properties for other pressures and Cs and KNa additions. The parameters presented in Table 1 are averaged over several tests with close p_c, α, and g values.

The parameters of the flow in the pass-flow channel were calculated in the quasi-one-dimensional approximation by using experimental p_c, α, and g values and the real properties, implying the plane boundary layer [8, 9]. The effect of boundary layers on the calculated σ_∞ value in the flow core was no more than 3% and was ignored.

Measurements of σ for the case of cesium addition corroborated the existence of optima in α ($\alpha_0 \approx 0.9$) and g ($g_0 \approx 0.8$) determined by calculations (Fig. 2). However, the best agreement between calculations and measurements is achieved for $\alpha \approx 0.7$–0.8 (Fig. 2). In this case, the experimental data differ from calculations by about 10% for the basic set of experiments for g = 0.7–0.8 and 20–30% for $g \approx 0.9$. An increase in the spread of conductivity values in the latter case is associated with the worsening of mixture formation in the plasma generator when the addition rate is high. Although temperature in the plasma generator increased as the optimum α_0 value was approached, σ did not increase in experiments, because heat losses increased in this region.

The maximum experimental values σ for Cs addition were obtained for p_c = 2.5–4.8 MPa and $g \approx 0.8$ in the range $\sigma \approx 0.8$–1.0 and were equal to 17–19 S/m; the calculated values are σv^2 = 45–170 S/m (km/s)^2 and μ_e is from 0.18 to 0.11 T^{-1}.

Experimental and calculated parameters of the combustion products of the hydrogen–oxygen fuel with KNa-eutectic addition are given in Table 1 and Fig. 3. Measurements of σ also corroborated the existence of maxima in α ($\alpha_0 \approx 0.9$) and g ($g_0 \approx 0.45$) (Fig. 3). The maximum values σ = 7–8 S/m were obtained for p_c = 2–4 MPa, g = 0.4–0.5, and α = 0.75–0.95. For these conditions, μ_e is from 0.18 to 0.14 T^{-1} and σv^2 = 70–82 S/m (km/s)^2. The difference between the measured conductivity values and calculations for the basic

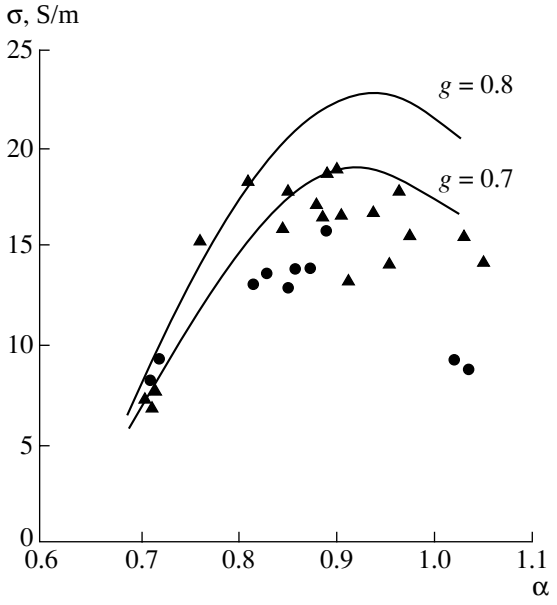

Fig. 2. Conductivity σ of the combustion products of the hydrogen–oxygen fuel with cesium addition vs. the oxidant-excess coefficient α for p_c = 4.5 MPa and M = 2.4; the circles and triangles are the experimental data for g = 0.7 and 0.78, respectively, and the lines are the calculations.

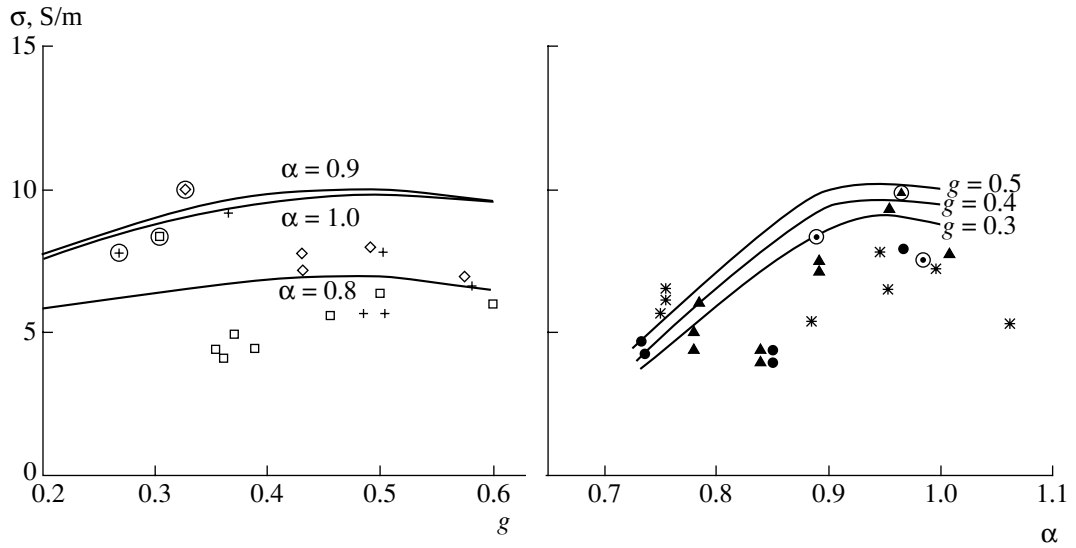

Fig. 3. Conductivity σ of the combustion products of the hydrogen–oxygen fuel with Kna-eutectic addition vs. the oxidant-excess coefficient α for p_c = 4.0 MPa and M = 2.5; the circles, triangles, and asterisks are the experimental data for g = 0.3, 0.4, and 0.5, respectively; the squares, rhombuses, and crosses are the experimental data for α = 0.8, 0.9, and 1.0, respectively; and the lines are the calculations.

set of experiments was equal to 15–20%, and their best agreement is achieved for α = 0.7–0.8. A decrease in the experimental σ value in the range α = 0.9–1.0 is also associated with an increase in the negative effect of heat losses.

3. Further investigations were carried out on a large-scale model device (rate up to 12 kg/s and power up to 150 MW) where the pass-flow channel has a characteristic size of 1950 mm. It consisted of a plasma generator, a supersonic nozzle, and a linear MHD channel, which was made in three modifications: full-scale uncooled and cooled MHD channels and the cooled diagnostic section of the MHD channel (Fig. 4). The plasma generator has a 90-mm-long cylindrical combustion chamber with a diameter of 200 mm on whose atomizer head 60 three-component atomizers are placed. A supersonic nozzle 470 mm in length had an axisymmetric subsonic part and a critical cross section with a diameter of 92.3 mm. For p_c = 2–4 MPa, the rate of combustion products was equal to 6–12 kg/s and the heat power was equal to 75–150 MW. The round cross section was smoothly transformed into a square cross section with an outlet size of 140 × 140 mm in the subsonic part of the nozzle. This transformation ensured the acceleration of the flow up to the Mach number M ≈ 2.4. The units of the plasma generator are cooled by the regenerative flow cooling by hydrogen.

Table 1. Characteristic experimental and calculated parameters for the model device

Parameter	Cs addition				KNa addition		
p_c, MPa	6.0	4.9	4.3	2.5	3.8	2.7	2.1
α	0.92	0.89	0.85	0.9	0.89	0.84	0.88
g	0.82	0.76	0.75	0.85	0.43	0.39	0.5
T_c, K	3650	3610	3600	3520	3650	3490	3470
F/F_{cr}	3.16	3.21	3.25	3.19	3.21	3.17	3.19
p, MPa	0.418	0.334	0.319	0.173	0.273	0.194	0.138
T, K	2890	2860	2830	2810	2810	2760	2750
v, m/s	2470	2520	2650	2370	2940	2990	2890
σ, S/m	22.3	21	20.5	36.5	8.75	9.09	11.6
σ_{exp}, S/m	10.2	12.2	16.2	17.5	7.27	7.2	7.4
μ_e, T^{-1}	0.079	0.099	0.104	0.175	0.094	0.135	0.166
$\sigma_{exp}v^2$, S/m(km/s)^2	62.2	96.3	114	98.1	63.2	64.3	67

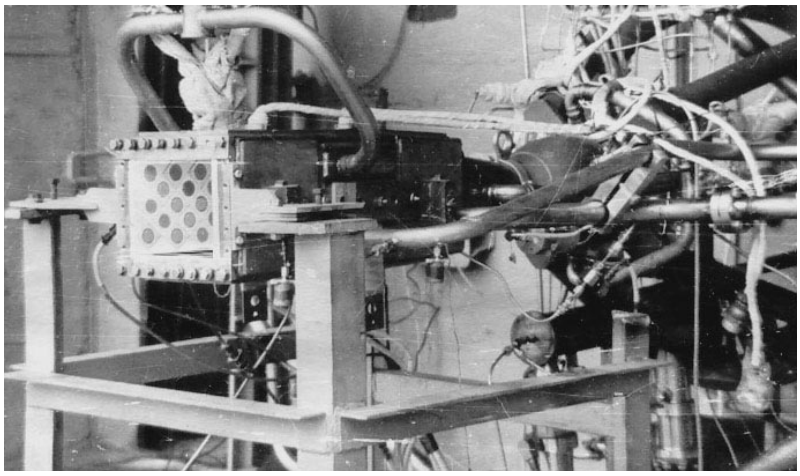

Fig. 4. General view of the large-scale model MHD device with the diagnostic section of the MHD channel.

The construction of a full-scale uncooled MHD channel is similar to that of the Pamir-1 MHD generator on solid (powder) plasma-forming fuel [1, 2], and its working zone with graphite electrodes has a length of 1000 mm. The length of the block of the full-scale cooled MHD channel was equal to 1480 mm, the length of its electrode zone was equal to 1000 mm, and its outlet cross sizes were 160 × 162 mm. The interelectrode spacing increased linearly to 260 mm at the exit. The electrode wall consisted of 20 sectioned steel electrodes 50 mm in length, which could be connected by external commutation in the Faraday or diagonal scheme. Each electrode was cooled by hydrogen flow–screen cooling. Crimped refractory-metal elements were welded to the "fire" surface of electrodes. The insulation wall was composed of 40 × 40-mm ceramic modules in whose central part a porous penetrable element of the wall with a diameter of 26 mm (relative blowing area of 0.35) was placed for screen cooling with the relative channel-average blowing rate $j_w = \dfrac{(\rho v)_w}{(\rho v)_\infty} = 0.002$.

To experimentally develop the construction of the basic units of cooled MHD channels, several diagnostic MHD channels with the electrode zone shortened to 200 mm were manufactured. All basic elements and units of electrode and insulation walls were identical for the full-scale and diagnostic MHD channels. The developed construction and technological solutions ensured the satisfaction state of the channels after three or four 100-s runs. Twenty-four probes were mounted on one of the insulation walls of uncooled MHD channels, and 20 probes were assembled in the cooled diagnostic channel to measure the longitudinal and transverse distributions of potentials.

Conductivity was measured in experiments with KNa eutectic in an applied electric field with 50–100 V voltage on electrodes and 100–400 A total current. Near-electrode voltage drop was determined by using measured current, voltage, and potentials of probes. When determining the conductivity in the flow core, behind-electrode current spread was taken into account. It was assumed that equipotential surfaces were parallel to the electrode surfaces, the real distribution of conductivity over the channel length was similar to the calculated one, and the inhomogeneities of conductivity in the cross section of the MHD channel were determined by boundary layers. The development and structure of the dynamic and thermal boundary layers, as well as the thicknesses of conductivity losses, were calculated for the electrode and insulation walls of the nozzle and MHD channel with the inclusion of the temperature of walls and their roughness and penetrability (equally distributed blowing) [9]. Figure 3 (symbols in the circles) and Table 2 present the σ values obtained by the above method for the combustion products of the hydrogen–oxygen fuel with KNa addition on the model device. The parameters in Table 2 are averaged over several tests with close values of p_c, α, and g, whereas other quantities, except for T_c, refer to the cross section in the middle of the channel.

When using uncooled channels, experimental values σ obtained on the model and large-scale model devices agree with each other. The maximum conductivity σ_∞ in the flow core under the optimum conditions reaches 9 S/m, $\sigma_\infty v^2 \approx 70$ S/m (km/s)^2, and $\mu_e \approx 0.16$ T^{-1}. In the flow-cooling section of the plasma generator, hydrogen is heated from 300 to 570 K, which ensures an increase in conductivity in experiments by a factor of about 1.3.

4. Thus, our investigations corroborated the possibility of creating supersonic flows of combustion products of the hydrogen–oxygen fuel with alkali-metal additions with the parameters σ = 10–20 S/m, μ_e = 0.1–0.2 T^{-1}, and σv^2 = 60–120 S/m (km/s)^2 acceptable for engineering applications. To reach σ values maximally close to the calculated values (conductivity coef-

Table 2. Characteristic experimental and calculated parameters for the large-scale model device

Parameter	Uncooled MHD, kcal		Cooled MHD, kcal	
p_c, MPa	4.05	2.08	3.95	2.1
α	0.96	0.89	0.88	0.95
g	0.33	0.30	0.30	0.33
T_c, K	3580	3410	3510	3420
F/F_{cr}	4.47	4.48	3.68	3.69
p, MPa	0.176	0.091	0.225	0.119
T, K	2750	2580	2680	2670
v, m/s	3110	2910	2820	2760
σ_{exp}, S/m	10.2	7.6	8.6	7.0
μ_e, T^{-1}	0.158	0.174	0.075	0.145
$\sigma_{exp}v^2$, S/m(km/s)^2	98.7	64.4	68.4	53.3

ficient $k_\sigma = \dfrac{\sigma_{exp}}{\sigma_{ideal}} > 0.8$), it is necessary to further study and optimize volume and surface processes in the plasma generator and pass-flow channel of the MHD generator.

The large-scale model device and combustion chamber can be considered as prototypes for the creation of full-scale multimegawatt MHD energy converters and high-temperature vapor generators, respectively.

Estimates and calculations show that MHD generators with electric powers 10–100 MW and linear Faraday, diagonal, and disk Hall channels on the combustion products of the hydrogen–oxygen fuel with cryoresistive or superconducting magnets with induction 4–7 T can ensure the energy transformation coefficient 7–12% and specific energy yield 1.5–2 MJ/kg for the specific mass of the MHD device from 0.3 to 0.1 ton/MW [4, 10].

REFERENCES

1. V. V. Breev, A. V. Gubarev, and V. P. Panchenko, *Supersonic MHD Generators* (Énergoatomizdat, Moscow, 1988).
2. *Encyclopedia of Low-Temperature Plasma*, Vol. 4: *Gas and Plasma Lasers*, Ed. by V. E. Fortov (Nauka, Moscow, 2000), Vol. 4.
3. *Atomic Hydrogen Power Generation and Technology: A Collection of Articles*, Ed. by V. A. Legasov (Énergoatomizdat, Moscow, 1988), Vol. 8.
4. L. K. Kovalev, Doctoral Dissertation (Mosk. Aviats. Inst., Moscow, 1996).
5. V. A. Bityurin, A. N. Bocharov, A. V. Krasilnikov, and A. V. Mikhailov, AIAA Pap., No. 2003-0377 (2003).
6. Yu. G. Chernov, B. B. Sakharov, and V. Yu. Veretenov, Preprint No. IAÉ-3522 (Institute of Atomic Energy, Moscow, 1981).
7. Yu. G. Degtev, V. P. Kuleshov, and V. R. Shevchenko, in *Thermal Engineering Problems of Direct Transformation of Energy* (Naukova Dumka, Kiev, 1975), pp. 46–51.
8. I. M. Vasenin, A. A. Glazunov, A. V. Gubarev, *et al.*, Preprint No. IAÉ-5014 (Institute of Atomic Energy, Moscow, 1990).
9. A. V. Gubarev, V. P. Panchenko, M. M. Rikenglaz, and E. K. Kholshchevnikova, Izv. Akad. Nauk SSSR, Mekh. Zhidk. Gaza, No. 3, 35 (1990).
10. L. K. Kovalev, K. L. Kovalev, S. V. Koneev, *et al.*, in *Proceedings of the 12th International Conference on MHD Electrical Power Generation, Yokohama, 1996*, Vol. 1, pp. 322–326.

Translated by R. Tyapaev

Doklady Physics, Vol. 49, No. 8, 2004, pp. 471–475. Translated from Doklady Akademii Nauk, Vol. 397, No. 4, 2004, pp. 481–485.

MECHANICS

Design of a Stable Airfoil

D. F. Abzalilov* and N. B. Il'inskiĭ**

Presented by Academician G.G. Chernyĭ April 16, 2004

Received March 19, 2004

INTRODUCTION

The problem of designing a longitudinally stable airfoil is considered in the framework of the model of an ideal incompressible fluid. A solution is constructed by the method of inverse boundary value problems of aero- and hydrodynamics. The fulfillment of the conditions of the solvability of a problem and the longitudinal stability of the airfoil is achieved by the quasisolution method for incorrect problems of mathematical physics. Such an approach involving the velocity distribution over the desired airfoil contour as input data makes it possible to find the shape of stable airfoils with quite good aerodynamic characteristics.

One of the effective methods of designing airfoils is the method based on solving an inverse boundary value problem of aero- and hydrodynamics, where the velocity distribution over the desired airfoil contour is taken as basic input data. It is difficult to solve this problem due to the presence of solvability conditions—conditions of the closeness of the desired contour and the coincidence of the velocity specified at infinity with the velocity determined by solving. Progress in overcoming these difficulties is associated with the development of the theory of quasisolutions for inverse boundary value problems of aero- and hydrodynamics [1].

When designing flying-wing airfoils, the problem of the stability of such a wing is of primary importance. In this case, the stability condition can be treated as one more solvability condition.

FORMULATION OF THE PROBLEM

In the physical $z = x + iy$ plane, the desired airfoil L_z with an infinitely thin edge is streamlined at flow trailing point B by a plane steady flow of an ideal incompressible fluid with the velocity v_∞ at infinity. We denote the flow domain as G_z (Fig. 1). The perimeter l of the airfoil contour is specified. Flow trailing point B is taken as the coordinate origin. The distribution of velocity v is specified as a function of arc abscissa s measured clockwise from point B,

$$v = v(s), \quad s \in [0, l]. \tag{1}$$

At point A ($s = s_a$) of flow splitting, the velocity vanishes, $v(s_a) = 0$. The sign of $v(s)$ is determined by the bypass direction. Therefore, $v(s) < 0$ for $s \in [0, s_a]$ and $v(s) > 0$ for $s \in (s_a, l]$.

It is known (see, e.g., [2]) that the stability of an aircraft is determined by the mutual location of the center of mass x_m and aerodynamic focus x_f. The criterion of the stability of the aircraft has the form

$$x_\mathrm{f} - x_\mathrm{m} > 0. \tag{2}$$

To find the center of mass, it is necessary to know the configuration of the aircraft as a whole. In particular, the center of mass of a tailless or flying-wing aircraft coincides with the wing pressure center x_p. For this reason, we consider x_m as either being specified or coinciding with x_p.

It is necessary to determine the shape L_z of an airfoil whose focus x_f is at a given point $x_\mathrm{f}^* > x_\mathrm{m}$ and velocity distribution over its surface differs minimally from given distribution (1).

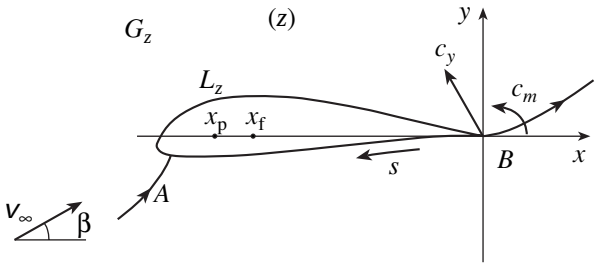

Fig. 1. Physical plane.

Chebotarev Research Institute of Mathematics and Mechanics, Kazan State University, ul. Kremlevskaya 18, Kazan, 420008 Tatarstan, Russia

** e-mail: damir.abzalilov@ksu.ru*

*** e-mail: nikolay.ilinskiy@ksu.ru*

1028-3358/04/4908-0471$26.00

SOLUTION

Let us introduce the canonical domain G_ζ that is the exterior of the unit circle $|\zeta| > 1$ in the ζ plane. The one-to-one conformal mapping of the domain G_z onto the domain G_ζ implies the correspondence between infinitely far points, as well as the transformation of the point $z = 0$ into the point $\zeta = 1$ (point B).

The complex conjugate velocity $\frac{dw}{d\zeta}$ of the stream around the unit disk has the form

$$\frac{dw}{d\zeta} = u_\infty e^{-i\beta}\left(1 - \frac{\zeta_a}{\zeta}\right)\left(1 - \frac{1}{\zeta}\right), \qquad (3)$$

where u_∞ and β are the absolute value and argument, respectively, of the velocity at infinity in the ζ plane and $\zeta_a = e^{i(\pi + 2\beta)}$ is the coordinate of point A on the circle. Passing on the boundary $\zeta = e^{i\gamma}$, we find from Eq. (3) that

$$u(\gamma) = 4u_\infty \sin\frac{\gamma}{2}\cos\frac{\gamma - 2\beta}{2},$$

$$\varphi(\gamma) = \int_{\gamma_a}^{\gamma} u(\gamma)d\gamma, \quad \gamma \in [0, 2\pi].$$

The velocity potential on the airfoil contour has the form

$$\varphi(s) = \int_{s_a}^{s} v(s)ds, \quad s \in [0, l].$$

Comparing $\varphi(s)$ and $\varphi(\gamma)$, we obtain u_∞, β, and function $s = s(\gamma)$ for $\gamma \in [0, 2\pi]$.

Let us consider the function

$$\chi(\zeta) = \ln\left(\frac{e^{i\beta}}{v_\infty}\frac{dw}{dz}\right) - \ln\left(1 - \frac{\zeta_a}{\zeta}\right) = S + iT, \qquad (4)$$

which is analytic in G_ζ and is the Michel–Joukowski function $\ln\frac{dw}{dz}$ with the excluded singularity at point A. The real part of this function $S(\gamma) = \mathrm{Re}\chi(e^{i\gamma})$ at the disk boundary $\zeta = e^{i\gamma}$ is determined by the formula

$$S(\gamma) = \ln\frac{v[s(\gamma)]}{2\cos(\gamma/2 - \beta)}, \quad \gamma \in [0, 2\pi]. \qquad (5)$$

Knowing $S(\gamma)$ on the circle, we obtain the function $\chi(\zeta)$ in the domain G_ζ by the Schwartz formula. This function is determined up to an imaginary constant corresponding to the airfoil rotation (and, correspondingly, the argument of the incident flow velocity) in the physical z plane. Setting $\mathrm{Im}\chi(\infty) = 0$, we obtain

$$\chi(\zeta) = \frac{1}{2\pi}\int_0^{2\pi} S(\gamma)\frac{\zeta + e^{i\gamma}}{\zeta - e^{i\gamma}}d\gamma,$$

i.e., the velocity argument at infinity in the z plane is also equal to β. The coordinates of the airfoil contour are determined by the formula

$$z(\zeta) = \frac{u_\infty}{v_\infty}\int_1^{\zeta} e^{-\chi(\zeta)}\left(1 - \frac{1}{\zeta}\right)d\zeta$$

for $\zeta = e^{i\gamma}$, where $\gamma \in [0, 2\pi]$.

To obtain the conditions of the closeness of the desired airfoil contour and coincidence of velocities at infinity, we expand the 2π-periodic function $S(\gamma)$ [see Eq. (5)] into the Fourier series

$$S(\gamma) = \frac{a_0}{2} + \sum_{k=1}^{\infty}(a_k\cos k\gamma + b_k\sin k\gamma). \qquad (6)$$

In this case, the expansion of the function $\chi(\zeta)$ into the Laurent series in G_ζ has the form

$$\chi(\zeta) = \frac{a_0}{2} + \sum_{k=1}^{\infty}(a_k + ib_k)\zeta^{-k}.$$

The complex conjugate velocity is expressed from Eq. (4) as

$$\frac{dw}{dz} = v_\infty e^{-i\beta}e^{\chi(\zeta)}\left(1 - \frac{\zeta_a}{\zeta}\right). \qquad (7)$$

At infinity, $\frac{dw}{dz} = v_\infty e^{-i\beta}$ and, therefore, $\chi(\infty) = 0$ or

$$a_0 = \frac{1}{\pi}\int_0^{2\pi} S(\gamma)d\gamma = 0. \qquad (8)$$

From Eqs. (3) and (7), we obtain

$$\frac{dz}{d\zeta} = \frac{u_\infty}{v_\infty}e^{-\chi(\zeta)}\left(1 - \frac{1}{\zeta}\right).$$

The closeness condition for the obtained airfoil contour has the form $\operatorname{res}_{\zeta=\infty}\frac{dz}{d\zeta} = 0$, from which it follows that

$a_1 + ib_1 = -1$. Thus, the contour closeness conditions

$$a_1 = \frac{1}{\pi}\int_0^{2\pi} S(\gamma)\cos\gamma d\gamma = -1,$$
$$b_1 = \frac{1}{\pi}\int_0^{2\pi} S(\gamma)\sin\gamma d\gamma = 0 \quad (9)$$

and condition (8) are determined by the first three coefficients of expansion (6).

The simplest method of satisfying these conditions is the substitution of necessary coefficients given by Eqs. (8) and (9) into Eq. (6). As was shown in [1], this substitution into input data provides the smallest difference between the initial and modified functions $S(\gamma)$.

To ensure the longitudinal stability of the airfoil, the above conditions of the solvability of the problem must be supplemented by the stability condition. In contrast to the solvability conditions, stability condition (2) is determined by the function $S(\gamma)$ as a whole rather than by a finite number of its expansion coefficients in series (6).

The aerodynamic force and moment acting on the airfoil are calculated by the Chaplygin formulas

$$\bar{\mathbf{R}} = -\frac{\rho i}{2}\oint_{L_z}\frac{dw}{dz}\frac{dw}{d\zeta}d\zeta,$$
$$M_z = \frac{\rho}{2}\mathrm{Re}\oint_{L_z}\frac{dw}{dz}\frac{dw}{d\zeta}z(\zeta)d\zeta, \quad (10)$$

where the bar over a symbol stands for complex conjugation. Since the flow is free of singularities, it is possible to pass from the integration over the airfoil contour to the infinite-radius circle contour L_R. In this case, in view of Eqs. (10), the dimensionless coefficients of the force and moment are written in the form

$$\bar{c}_r = \frac{2\bar{\mathbf{R}}}{\rho v_\infty^2 b} = \frac{2\pi}{v_\infty^2 b}\operatorname*{res}_{\zeta=\infty}\frac{dw}{dz}\frac{dw}{d\zeta},$$
$$c_m = \frac{2M_z}{\rho v_\infty^2 b^2} = -\frac{2\pi}{v_\infty^2 b^2}\mathrm{Im}\operatorname*{res}_{\zeta=\infty}\frac{dw}{dz}\frac{dw}{d\zeta}z(\zeta), \quad (11)$$

respectively. Substituting Eqs. (3) and (7) into Eqs. (11), we arrive at the following expression for the aerodynamic force coefficient:

$$\bar{c}_r = -\frac{u_\infty}{b v_\infty}8\pi i e^{-i\beta}\sin\beta.$$

In view of the equality $c_r = e^{i\beta}(c_x + ic_y)$,

$$c_x = 0, \quad c_y = \frac{8\pi u_\infty}{b v_\infty}\sin\beta. \quad (12)$$

The moment coefficient (with respect to the rear edge B) is expressed as

$$c_m = \frac{2\pi u_\infty^2}{b^2 v_\infty^2}[4\sin\beta(C_1\cos\beta + C_2\sin\beta) - \sin 2\beta - 2(a_2\sin 2\beta - b_2\cos 2\beta)]. \quad (13)$$

Here,

$$C = C_1 + iC_2 = \frac{v_\infty}{2\pi u_\infty}\int_0^{2\pi} z(\gamma)d\gamma$$

is a complex constant depending on the shape of the resulting airfoil.

The pressure center and aerodynamic focus is usually measured from the front edge. They are expressed in terms of the coefficients c_y and c_m as

$$x_\mathrm{p} = 1 + \frac{c_m}{c_y\cos\beta}, \quad x_\mathrm{f} = 1 + \frac{c_m^\beta}{c_y^\beta\cos\beta - c_y\sin\beta}.$$

Here, c_y^β and c_m^β are obtained by differentiating Eqs. (12) and (13) with respect to β and have the form

$$c_y^\beta = \frac{8\pi u_\infty}{b v_\infty}\cos\beta,$$

$$c_m^\beta = \frac{4\pi u_\infty^2}{b^2 v_\infty^2}[-\cos 2\beta - 2(a_2\cos 2\beta + b_2\sin 2\beta) + 2(C_1\cos 2\beta + C_2\sin\beta)].$$

Then, the problem of designing the stable airfoil can be formulated as follows. In the set

$$\mathbb{K} = \left\{S(\gamma) \in \mathbb{H}(A, \sigma): \int_0^{2\pi} S(\gamma)d\gamma = 0, \int_0^{2\pi} S(\gamma)\cos\gamma d\gamma = -\pi, \int_0^{2\pi} S(\gamma)\sin\gamma d\gamma = 0, x_\mathrm{f}(S) = x_\mathrm{f}^*\right\},$$

where $\mathbb{H}(A, \sigma)$ is the class of the Hölder functions with fixed constants $A \in (0, \infty)$ and $\sigma \in (0, 1]$, it is necessary

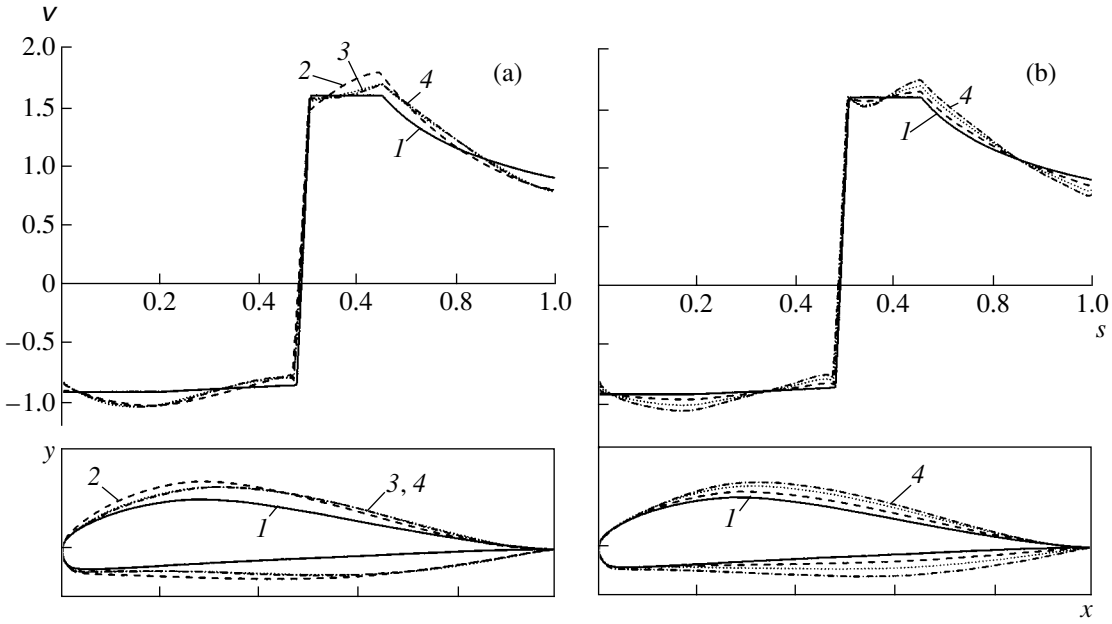

Fig. 2. Results of calculations.

to find a function $S^*(\gamma) \in \mathbb{K}$ such that

$$\|S^*(\gamma) - S(\gamma)\|_{L_2[0, 2\pi]} = \inf_{F \in \mathbb{K}} \|F(\gamma) - S(\gamma)\|_{L_2[0, 2\pi]}.$$

This problem is difficult because the relations of $S(\gamma)$ to C and, correspondingly, to x_f are nonlinear. For this reason, the problem is further solved numerically by using minimizing sequences. For a term $S_n(\gamma)$ of this sequence, the problem of seeking a minimum of a function of $2n$ variables—the coefficients a_k and b_k, $k = 2, 3, \ldots, n + 2$, of expansion (6)—is solved.

PARTICULAR CALCULATIONS

Figure 2a exemplifies the design of the airfoil with the stability condition. The initial velocity distribution (line *1*) is taken such that it satisfies conditions (8) and (9). The position of the aerodynamic focus for this airfoil is $x_f = 0.2461$. It is necessary to design an airfoil whose aerodynamic focus is located at the point $x_f^* = 0.27$. Lines *2–4* in Fig. 2 are obtained by solving this problem with variation of two, four, and six coefficients of the Fourier series, respectively. With an increase in the number of varying coefficients, the minimizing sequence converges.

Figure 2b shows the change in the velocity distribution and airfoil shape with an increase in x_f^*. With an increase in the difference between the initial x_f and desired x_f^* values, the difference between the initial and obtained velocity distributions increases and airfoils gradually take the S-like shape characteristic for stable airfoils. Lines *1–4* correspond to the rightward shift of the focus by 1–4% of the chord, respectively.

In the next example, to satisfy the stability condition, the velocity distribution is varied only on the lower surface. The initial airfoil (line *1* in Fig. 3) is designed by using a given continuous velocity distribution. At the

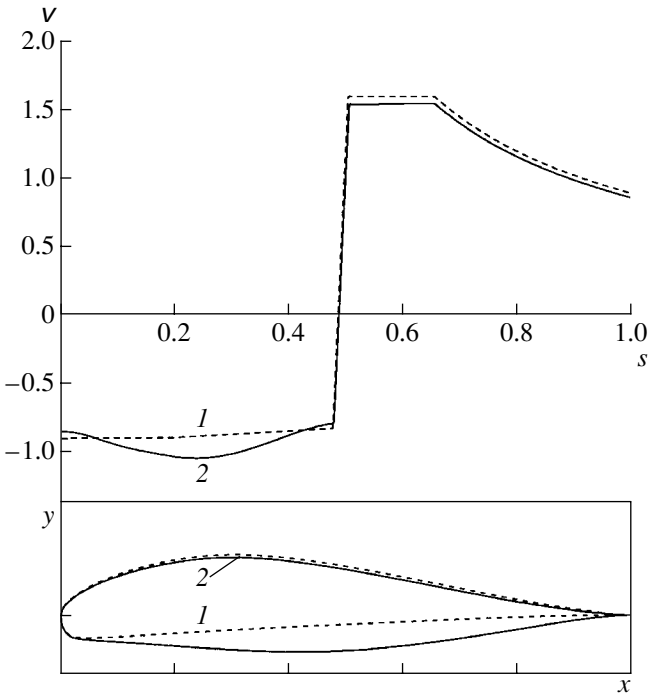

Fig. 3. Modification of velocity on the lower surface.

attack angle $\alpha = 5.6°$, the designed airfoil has $c_y = 1.01$, and the aerodynamic focus and pressure center are located at the points $x_f = 0.2461$ and $x_p = 0.3040$, respectively. Then, the problem of the minimum correction of the velocity distribution on the lower surface with the condition $x_f > x_p$ is solved numerically. The result is shown by line *2* in Fig. 3. The velocity distribution on the upper surface also changes slightly, because, to satisfy conditions (8) and (9), the velocity distribution is varied over the entire airfoil, but the flow remains continuous. For $\alpha = 5.4°$, the obtained airfoil has $c_y = 0.74$, aerodynamic focus $x_f = 0.2625$, and pressure center $x_p = 0.2556$.

ACKNOWLEDGMENTS

This work was supported by the Russian Foundation for Basic Research, project nos. 01-01-04004, 02-01-00061, and 03-01-06259.

REFERENCES

1. A. M. Elizarov, N. B. Il'inskiĭ, and A. V. Potashev, *Inverse Boundary Value Problems of Aerohydrodynamics* (Nauka, Moscow, 1994).
2. N. F. Krasnov, *Aerodynamics*, Part 1: *Fundamentals of Theory. Aerodynamics of an Airfoil and Wing* (Vysshaya Shkola, Moscow, 1980).

Translated by R. Tyapaev

Doklady Physics, Vol. 49, No. 8, 2004, pp. 476–479. Translated from Doklady Akademii Nauk, Vol. 397, No. 4, 2004, pp. 486–489.

MECHANICS

Possibility of Using Laser Action on a Celestial Body Approaching the Earth

V. V. Ivashkin

Presented by Academician T.M. Éneev March 18, 2004

Received March 23, 2004

INTRODUCTION

The possibility of preventing a collision with a celestial body approaching the Earth (near-Earth object, NEO) such as an asteroid or comet by using laser action on the body is analyzed. It is assumed that a laser is placed on a space station or on a base near the Earth, e.g., on the Moon (or near Earth's orbit), where astronomical and power stations are also present. The power station converts solar energy into electrical energy for the astronomical and laser stations. The telescopes of the observatory search for the NEO in order to detect a dangerous object that can collide with the Earth [1]. In this case, the laser acts on this object to deflect it from the Earth or to destroy it. A concept of such a station was proposed and supported in the International Symposium on Deep Space Exploration Technology and Application, Qingdao, People's Republic of China, in 2002, which initiated this work, where the problem of laser action is analyzed. Velocity impulse, energy, power, time, action distance, and the size of solar batteries are estimated.

MODEL OF LASER ACTION ON THE BODY

We assume that the body subjected to intense laser radiation is destroyed or its substance is transformed to a plasma. Due to reactive acceleration $\mathbf{j}_B$ induced by a plasma jet from the body, the body deflects from the Earth (see Fig. 1) [2].

MODEL OF MOTION OF THE DANGEROUS CELESTIAL BODY

We analyze two possible cases of motion of the celestial body under the external action [3, 4]. In the first case, the body flies near the station (at a distance of $\rho_{min} \sim 10^6$ km) and collides with the Earth on one of the next revolutions of the heliocentric orbit. In this case, we consider action on the body for its deflection from the Earth. Figure 2 shows the scheme of flying the NEO near the Earth and station based on the Moon and action on it on the arc $B_1B_2B_3$ of NEO's orbit and the arc $M_1M_2M_3$ of Moon's orbit. To estimate laser action, let us reduce it to a pulse change δV_B of the heliocentric body velocity $\mathbf{V}_B$. This change is given by the expression [5]

$$\delta V_B \approx \delta d[3(2a_B - 1)n_C T_B \sin\alpha]^{-1}, \quad \cos\alpha = \frac{\mathbf{V}_B, \mathbf{V}_\infty}{V_B V_\infty}, \tag{1}$$

where the deflection δd of the body with respect to the Earth is perpendicular to the geocentric body velocity $\mathbf{V}_\infty$, a_B (in astronomical units) is the semimajor axis of the body's orbit, T_B is the orbital period of the body, and n_C is the number of revolutions before the collision. We estimate δV_B for $n_C = 1$, δd = (for asteroids) $2R^*$ and (for comets) $5R^*$, where R^* is the critical deflection leading to the contact of the body's orbit with Earth's surface. A group of 25 asteroids approaching the Earth in the 21st century and a group of five comets [5], as well as model asteroids Athos and Aramis of the international scenario of the NEO problem [6], were analyzed. According to Eq. (1), $\delta V_B \approx 0.01$–0.19 m/s for 26 bodies, $\delta V_B \approx 0.24$–0.39 m/s for 5 bodies, and $\delta V_B \approx 0.73$ m/s for 1 body. In what follows, we analyze the case $\delta V_B = 0.2$ m/s.

In the second case, the body collides with the Earth already on the current revolution. In this case, the time to collision is small and the body must be destroyed.

CHARACTERISTICS OF LASER ACTION

We assume that the body is a spherical asteroid with radius $R_B = 0.1$–0.5 km and density $\rho_B = 3$ g/cm^3. When a body with mass M_B is deflected from the Earth with

Keldysh Institute of Applied Mathematics, Russian Academy of Sciences, Miusskaya pl. 4, Moscow, 125047 Russia
e-mail: ivashkin@spp.keldysh.ru

1028-3358/04/4908-0476$26.00

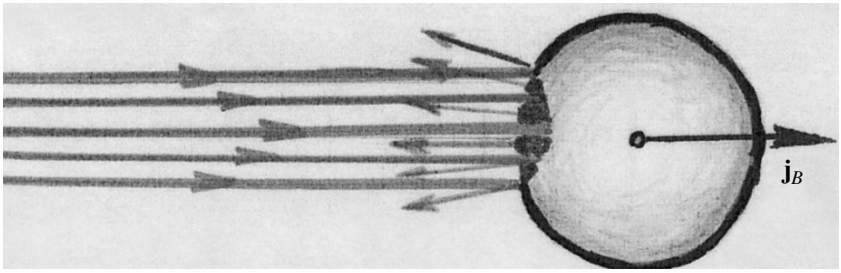

Fig. 1. Model of laser action on a celestial body.

velocity change δV_B, it acquires momentum $\delta Q_B = M_B \delta V_B$. The coefficient $c_m = \dfrac{dQ_B}{dE_Q}$ of the transformation of laser-radiation energy to momentum transferred to the body is equal to 2.1–4.8 din s/J for the radiation wavelength λ from 4 to 0.248 μm, respectively [2]. We assume that the axis of the laser beam passes through the center of the body, the cross section of the beam on the body is a disk with radius $R_f = \gamma R_B$, and a plasma jet flows from the body along its radius. Then, the deflection energy transferred to the body is determined as

$$E_Q = \frac{k\delta Q_B}{c_m} = a_E R_B^3, \quad k = \frac{2(1+c+c^2)}{3(1+c)}, \quad c = (1-\gamma^2)^{1/2}. \tag{2}$$

To estimate this energy, we consider the 3-μm infrared radiation of a deuterium fluoride (DF) laser. We take $c_m = 2.5$ din s/J. In this case, $a_E \sim 10^{17}$ J/km^3. The table presents the body's mass M_B and deflection energy E_Q given by Eq. (2). The action energy is sufficiently high and reaches several megatons of TNT.

Energy E_F necessary for the fragmentation of the body is estimated by analyzing the kinetic collision of bodies. According to [7], the critical specific energy of the fragmentation of the rock body is equal to $E_F' = \dfrac{E_F}{M_B} \sim 10^7$–$9 \times 10^8$ erg/g if the relative mass $M_F' = \dfrac{M_F}{M_B}$ of the largest fragment after fragmentation lies from 0.5 to 0.001, respectively. The energy for the fragmentation of an asteroid with a radius of 500 m upon impact action is equal to $E_F \sim 1.6 \times 10^{15}$–$1.4 \times 10^{17}$ J (0.4–33.7 megatons of TNT). For the model comet Porthos [6] with radius $R_B \sim 2.5$ km, $E_F' \sim 7 \times 10^7$ erg/g and $E_F \sim 120$ megatons of TNT for $M_F' = 0.001$. Then, we analyze the deflection of the body from the Earth.

Let us consider the deflection of the body by a pulsed laser with the radiation pulse intensity $I_f = 0.5$ GW/cm^2, pulse duration $\tau = 50$ ns, and pulsation frequency $\nu = 10$ Hz [2]. In this case, one-pulse energy E_I and average radiation power P_L are determined as

$$E_I = I_f \pi R_f^2 \tau, \quad P_L = E_I \nu = (\pi \tau \nu I_f) R_f^2 = a_P R_f^2. \tag{3}$$

This parameters determine the action time and path covered by the body (in the approximation of motion with constant velocity V_∞):

$$\Delta t_a = \frac{E_Q}{P_L} = \frac{a_E R_B^3}{a_P R_f^2} = \frac{a_E R_B}{a_P \gamma^2}, \quad \Delta s_a = V_\infty \Delta t_a. \tag{4}$$

For estimates, we take $\gamma = 0.3$–0.4 ($\gamma = 0.4$ only for $R_B = 100$ m and $\lambda = 3$ μm) and $V_\infty = 20$ km/s. The table presents the characteristics E_I and P_L given by Eq. (3), as well as Δt_a and Δs_a given by Eq. (4) and accepted maximum distances ρ_L to the target.

To estimate the geometric characteristics of action, the Gaussian beam model is taken (Fig. 3) [8]. The ini-

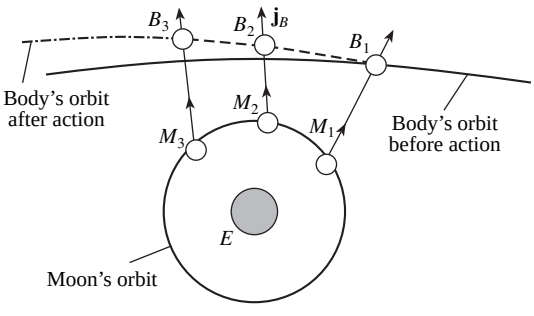

Fig. 2. Scheme of flying a celestial body *B* approaching the Earth and action on it, where *E* is the Earth and *M* is the Moon.

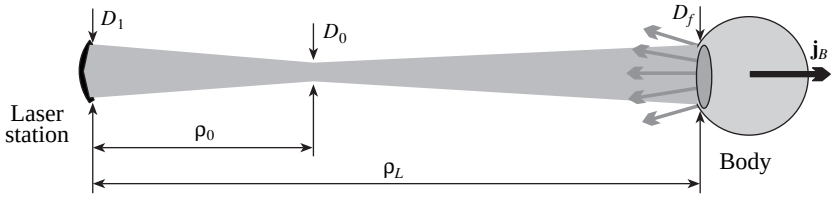

Fig. 3. Geometric model of a laser beam.

tial and minimum beam diameters D_1 and D_0 are determined in Kogelnik–Li theory [8, 2, 4] by the formulas

$$D_1^{-2} = a\left[1+\left(1-\frac{2}{c^2}\right)^{1/2}\right], \quad a = \frac{c}{b}, \quad c = 1+\frac{4R_f^2}{b}, \qquad (5)$$
$$b = \frac{8\mu\lambda\rho_L}{\pi}, \quad D_0^2 = \frac{D_1^2}{2},$$

where the beam-quality factor $\mu = 3$ is taken [2]. The table presents the values calculated for the initial beam radius $R_1 = \frac{D_1}{2}$ by Eqs. (5). As is seen, the initial radius of the infrared beam is quite large, 50 m. Current optical telescopes have much smaller apertures. However, several large telescopes are now being designed. In particular, a project of a 100-m telescope is discussed in European states. It is possible to produce several smaller lasers with the necessary total radiation cross sections. If $\lambda = 0.25$ μm (ultraviolet laser), the beam diameter is much smaller (~10–20 m), and it is easier to realize this laser. However, the initial radiation flux density is very high in this case.

CHARACTERISTICS OF THE POWER STATION

The laser-beam power P_L requires a certain electric power P_E. Let us consider a DF laser. In this case, its electrical efficiency is quite high, $\eta_E = \frac{P_L}{P_E} \approx 1$–10, due to using chemical energy [2]. If P_S is the necessary power of solar radiation and $\eta_S = \frac{P_E}{P_S}$ is the efficiency of solar batteries converting solar energy into electrical energy, then $P_E = \frac{P_L}{\eta_E}$ and $P_S = \frac{P_E}{\eta_S} = \frac{P_L}{\eta_E\eta_S}$. The necessary area F_{SP} and size a_{SP} of solar batteries are estimated as $F_{SP} = P_S/I_{S0}$, where $I_{S0} \sim 1370$ W/m^2, and $a_{SP} = F_{SP}^{1/2}$. The table presents electric power P_E, solar-radiation power P_S, and the area F_{SP} and size a_{SP} of solar batteries for $\eta_E = 1$ and $\eta_S = 0.1$. If the station is

Characteristics of the laser and power stations ($\lambda = 3$ μm)

Parameter	$R_B = 100$ m	$R_B = 300$ m	$R_B = 500$ m
M_B, kg	1.26×10^{10}	3.39×10^{11}	1.57×10^{12}
E_Q, J (megatons of TNT)	1×10^{14} (0.024)	2.7×10^{15} (0.63)	1.23×10^{16} (2.9)
R_f, m	40	90	150
E_I, GJ	1.3	6.4	17.7
P_L, P_E, GW	13	64	177
Δt_a, s (h)	7700 (2)	41700 (12)	69500 (19)
Δs_a, km	0.15×10^6	0.83×10^6	1.39×10^6
ρ_L, km	0.65×10^6	1.5×10^6	2×10^6
R_1, m	49	51	45
P_S, GW	126	636	1770
F_{SP}, km^2 (a_{SP}, km)	92 (10)	464 (22)	1290 (36)

constructed on the Moon, lunar regolith can be used for its operation [9].

CONCLUSIONS

Analysis of the laser-action system applying a velocity change of 0.2 m/s to asteroids with radii 0.1–0.5 km shows that the energy necessary for the deflection of the body is estimated as $(0.1–12.3) \times 10^{15}$ J ≈ 0.02–3 megatons of TNT. In this case, the average power of laser radiation and the electric power of the power station are equal to 13–180 GW, the action time is equal to $(8–70) \times 10^3$ s, and the maximum action distance is equal to $(0.6–2) \times 10^6$ km. The initial and final beam diameters are estimated as 10–100 and 60–300 m, respectively. The area of solar batteries is equal to 90–1300 km^2. These parameters can be optimized, or weakened, by, e.g., earlier action and decreasing velocity change. Nevertheless, it is seen that the realization of such a system is a difficult scientific and engineering problem, in particular because an intense beam, large emitting aperture, and accurate beam aiming are required. Analysis of the physical foundations of this laser-action method including the process of the formation and stable maintenance of a plasma jet (during about a day) also seems to be important. When such a system can be constructed, it will quickly prevent the collision of the Earth with not only small but also rather large celestial bodies with the acceptable forestalling time of action.

ACKNOWLEDGMENTS

I am grateful to V.A. Kochkin for stimulating discussions and useful advices, as well as to A.A. Korol'kova and A.V. Chernov for assistance in preparing the paper. This work was supported by the Russian Foundation for Basic Research (project no. 01-01-00133), Harbin Institute of Technology (People's Republic of China), and Space Age Publishing Company (United States).

REFERENCES

1. S. Isobe and M. Yoshikawa, Earth, Moon, Planets **72**, 263 (1995).
2. C. Phipps, in *Proceedings of the NASA Near Earth Object Interception Workshop, Los Alamos, 1992*, LA-UR-92-420, pp. 256–260.
3. V. V. Ivashkin, in *Proceedings of the International Lunar Conference, Waikoloa, 2003*, p. 25.
4. V. V. Ivashkin, Preprint No. 89, IPM im. M. V. Keldysha (Keldysh Institute of Applied Mathematics, Russian Academy of Sciences, Moscow, 2003).
5. V. V. Ivashkin, in *Proceedings of the Conference "Near-Earth Astronomy of the 21st Century," Zvenigorod, 2001* (GEOS, Moscow, 2001), pp. 294–304.
6. A. V. Zaitsev, V. V. Ivashkin, P. P. Kuznetsov, *et al.*, in *Book of Synopses of the Planetary Defense Conference "Protecting Earth from Asteroids," California, 2004* (AIAA, California, 2004), No. 2004-1456.
7. K. R. Housen and K. A. Holsapple, Icarus **84**, 226 (1990).
8. A. Gerrard and J. M. Burch, *Introduction to Matrix Methods in Optics* (Wiley, New York, 1975; Mir, Moscow, 1978).
9. A. Ignatiev, in *Proceedings of the International Lunar Conference, Waikoloa, 2003*, p. 93.

Translated by R. Tyapaev

Doklady Physics, Vol. 49, No. 8, 2004, pp. 480–482. Translated from Doklady Akademii Nauk, Vol. 397, No. 5, 2004, pp. 619–621.

MECHANICS

Harmonic Vibrations of a Layer with a Hollow

Corresponding Member of the RAS É. I. Grigolyuk*, L. A. Fil'shtinskiĭ, and Yu. D. Kovalev****

Received April 20, 2004

In this paper, the problem of the harmonic excitation of a layer weakened by a tunnel hollow of an arbitrary cross section is considered. Mixed dynamic problems of the theory of elasticity for the layer were investigated previously in [1]. The features of the eigenmode spectrum for a transversely isotropic disk plate near the edge resonance were studied in [2]. In the case of mixed conditions imposed on layer bases (the sliding fit of the ends or ends covered by a diaphragm rigid in its plane and flexible in the perpendicular direction), the arising boundary-value problem is simpler than the problems analyzed in [1].

The procedure for solving mixed problems of elasticity theory for steady-state vibrations of the layer with tunnel inhomogeneities was proposed in [3], where this procedure was used to represent mechanical quantities in the symmetric case. Below, similarly to [3], we consider the problem of longitudinal vibrations of a layer that has a through hollow and whose ends are covered by a diaphragm rigid in its plane and flexible in the perpendicular direction.

We analyze the elastic layer $-h \le x_3 \le h$, $-\infty < x_1, x_2 < \infty$, which is weakened by tunnel (along the Ox_3 axis) through hollows (holes) whose cross sections are rather smooth nonintersecting contours $L_j, j = 1, 2, \ldots, k$. We assume that a pulsed load $\mathrm{Re}\{(P, T, Z)\exp(-i\omega t)\}$ acts at the boundaries of the hollows. We also assume that mechanical quantities have the form

$$u_i = \mathrm{Re}(U_i \exp(-i\omega t)),$$
$$\sigma_{ij} = \mathrm{Re}(\langle\sigma_{ij}\rangle \exp(-i\omega t)). \tag{1}$$

Let the amplitudes of the components of the given load be expanded into Fourier series in the thickness coordinate x_3 within the segment $[-h, h]$ and the conditions

$$u_1(x_1, x_2, \pm h, t) = u_2(x_1, x_2, \pm h, t) = \sigma_{33}(x_1, x_2, \pm h, t) = 0 \tag{2}$$

hold true on the layer bases. We write the components of the displacement-vector amplitudes in the form

$$U_i = \sum_{k=0}^{\infty} u_{ik}(x_1, x_2)\cos\gamma_k x_3, \quad i = 1, 2,$$
$$U_3 = \sum_{k=0}^{\infty} u_{3k}(x_1, x_2)\sin\gamma_k x_3, \quad \gamma_k = \frac{(2k+1)\pi}{2h}. \tag{3}$$

Expressions (3) automatically satisfy boundary conditions (2) on the layer bases. The steady-state wave process in an isotropic cylinder is described by the equations of motion

$$\sigma \mathrm{grad}\theta + \Delta u = \frac{\rho}{\mu}\frac{\partial^2 \mathbf{u}}{\partial t^2},$$
$$\theta = \partial_k u_k, \quad \sigma = \frac{\lambda + \mu}{\mu} = \frac{1}{1 - 2\nu}, \tag{4}$$

where λ and μ are the Lame coefficients for the layer material.

Substituting Eqs. (3) into Eqs. (1) and then the latter into Eqs. (4), we exclude time and coordinate x_3 from the set of Eqs. (4) and arrive at the following equations for the Fourier coefficients u_{jk}:

$$\kappa_k^2 u_{ik} + \sigma\partial_i\theta_k = 0, \quad i = 1, 2, \quad \kappa_k^{(2)} u_{3k} - \sigma\gamma_k\theta_k = 0,$$
$$\kappa_k^{(2)} = \nabla^2 - \beta_k^2, \quad \beta_k^2 = \gamma_k^2 - \alpha_2^2, \quad \alpha_2 = \frac{\omega}{c_2}, \tag{5}$$
$$\nabla^2 = \partial_1^2 + \partial_2^2, \quad \theta_k = \partial_1 u_{1k} + \partial_2 u_{2k} + \gamma_k u_{3k}, \quad \partial_i = \frac{\partial}{\partial x_i}.$$

From the set of Eqs. (5), we immediately find

$$\kappa_k^{(1)}\theta_k = 0, \quad \kappa_k^{(1)} = \nabla^2 - \lambda_k^2,$$
$$\lambda_k^2 = \gamma_k^2 - \alpha_1^2, \quad \alpha_1 = \frac{\omega}{c_1}. \tag{6}$$

We introduce the function ψ_k by the relationship $\theta_k = \kappa_k^{(2)}\psi_k$. It follows from expressions (6) that

* *Moscow State Technical University "MAMI," Bol'shaya Semenovskaya ul. 38, Moscow, 105839 Russia*

** *Sumy State University, ul. Rimskogo-Korsakova 2, Sumy, 40007 Ukraine e-mail: Leonid@mphis.sumdu.edu.ua*

$\kappa_k^{(2)}\kappa_k^{(1)}\psi_k = 0$. With allowance for the relation between the quantities θ_k and ψ_k, the integration of system (5) yields

$$u_{ik} = -\sigma\partial_1\psi_k + \omega_{ik},$$
$$u_{3k} = \sigma\gamma_k\psi_k - \omega_{3k}, \quad \kappa_k^{(2)}\omega_{ik} = 0, \quad i = 1, 2. \tag{7}$$

Furthermore, in view of the relationship $\theta_k = \kappa_k^{(2)}\psi_k$, we arrive at the equalities

$$\omega_{1k} = \sigma\partial_2\Omega_k, \quad \omega_{2k} = -\sigma\partial_1\Omega_k,$$
$$\omega_{3k} = -\frac{1}{\gamma_k}(1-\sigma)\kappa_k^{(1)}\psi_k, \tag{8}$$

where Ω_k is an arbitrary solution of the equation $\kappa_k^{(2)}\Omega_k = 0$.

By virtue of Eqs. (7) and (8), we finally obtain

$$u_{ik} - iu_{2k} = 2\sigma\frac{\partial}{\partial z}(i\Omega_k - \Omega_k^{(1)} - \Omega_k^{(2)}),$$
$$\theta_k = (\alpha_2^2 - \alpha_1^2)\Omega_k^{(1)}, \tag{9}$$
$$u_{3k} = \sigma\gamma_k\Omega_k^{(1)} + \sigma\left[\gamma_k + \frac{1+\sigma}{\sigma\gamma_k}(\alpha_1^2 - \alpha_2^2)\right]\Omega_k^{(2)}.$$

Here, $\Omega_k^{(i)}$ is an arbitrary solution of the equation $\kappa_k^{(i)}\varphi = 0$. The functions Ω_k define the rotation of an element with respect to the Ox_3 axis.

Formulas (9) represent the homogeneous solutions of the formulated boundary-value problem for the layer. Based on the structure of these homogeneous solutions, we write the integral representation of field quantities. To do this, we take the metaharmonic functions entering into Eqs. (9) in the form of the simple-layer potentials

$$\Omega_k^{(1)} = \int_L p_k^{(1)}K_0(\lambda_k r)ds, \quad \Omega_k^2 = \int_L p_k^{(2)}K_0(\beta_k r)ds,$$
$$\Omega_k = \int_L p_k^{(3)}K_0(\beta_k r)ds, \tag{10}$$
$$r = |\zeta - z|, \quad \zeta = \xi_1 + i\xi_2 \in L = \cup L_1, \quad z = x_1 + ix_2,$$

where $K_0(\gamma r)$ is the zeroth-order modified Bessel function of the second kind; ds is an element of the contour L; and $p_k^{(1)}(\zeta)$, $p_k^{(2)}(\zeta)$, and $p_k^{(3)}(\zeta)$ are the densities to be determined.

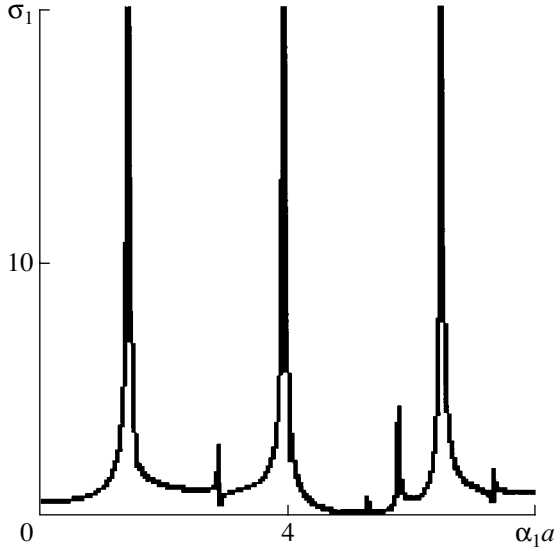

Fig. 1.

Using Hooke's law and formula (9), we can write the boundary conditions in the contour L as

$$\frac{1}{\mu}(N_k - iT_k) = [\Lambda(\sigma-1) - \sigma\lambda_k^2]\Omega_k^{(1)}$$
$$-\sigma\beta_k^2\Omega_k^2 + 4\sigma e^{2i\psi}\partial_{zz}^2(i\Omega_k - \Omega_k^{(1)} - \Omega_k^{(2)}),$$
$$\frac{1}{\mu}(N_k + iT_k) = [\Lambda(\sigma-1) - \sigma\lambda_k^2]\Omega_k^{(1)} - \sigma\beta_k^2\Omega_k^{(2)}$$
$$+ 4\sigma e^{-2i\psi}\partial_{zz}^2(-i\Omega_k - \Omega_k^{(1)} - \Omega_k^{(2)}), \tag{11}$$
$$\frac{1}{\mu}Z_k = e^{i\psi}\partial_z(b_k^0\Omega_k^{(2)} + ic_k^0\Omega_k) + e^{-i\psi}\partial_z(b_k^0\Omega_k^{(2)} - ic_k^0\Omega_k),$$
$$\Lambda = \alpha_2^2 - \alpha_1^2, \quad b_k^0 = -\frac{1+\sigma}{\sigma\gamma_k}\Lambda, \quad c_k^0 = \sigma\gamma_k,$$

where ψ is the angle between the outer normal to the contour L and the Ox_1 axis. A usual procedure reduces boundary value problem (11) with allowance for representations (10) to a set containing three singular integro-differential equations (for each fixed k), which is not presented here because of its cumbersome form.

As an example, we consider the layer weakened by the hollow with the elliptic cross section

$$\xi_1 = R_1\cos\varphi, \quad \xi_2 = R_2\sin\varphi, \quad 0 \le \varphi \le 2\pi.$$

In order to characterize the stress concentration in the layer with the hollow, we calculate the amplitude of the quantity

$$\sigma_{\theta\theta} = \sigma_{11}\sin^2\theta + \sigma_{22}\cos^2\theta - 2\sigma_{12}\cos\theta\sin\theta \tag{12}$$

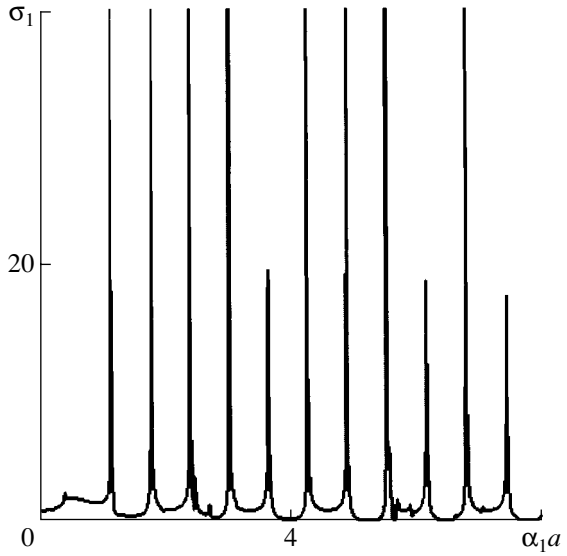

Fig. 2.

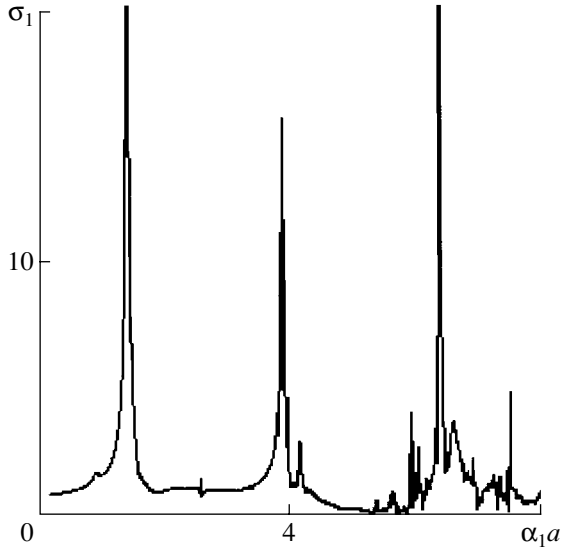

Fig. 3.

at the contour point $\varphi = \frac{\pi}{2}$, $x_3 = 0$ for the pulsed pressure $\mathrm{Re}(\exp(-i\omega t)P)$, where P = const, that is constant along the contour. In the numerical realization of the algorithm, the set of integral equations is reduced to a linear set of algebraic equations by the mechanical-quadrature method [4]. The sequence of the calculations is the following. Initially, the set of integral equations is numerically solved. Afterwards, we determine the Fourier coefficients $\sigma_{ij}^{(k)}$ of the stress tensor and stresses themselves. Then, using formula (12), we determine the desired quantities on the hollow surface.

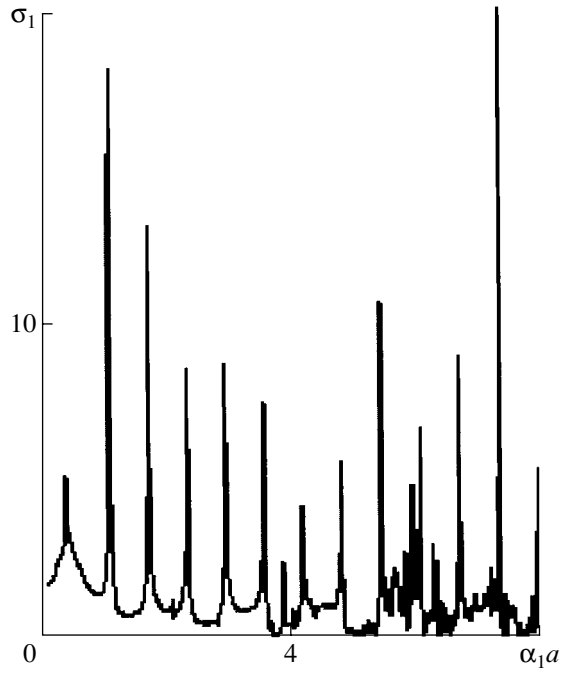

Fig. 4.

Figures 1 and 2 show the quantity $\sigma_1 = \left|\frac{\langle\sigma_{\theta\theta}\rangle}{P}\right|$ as a function of the variation of the dimensionless wave number $\alpha_1 a$ ($a = 1$ is the characteristic linear size) for the circular hollow ($R_1 = R_2 = 1$) for $\frac{h}{R_1} = 1$ and $\frac{h}{R_1} = 4$, respectively. In Figs. 3 and 4, similar results are shown for the elliptic hollow ($R_1 = 1$, $R_2 = 1.5$) with $\frac{h}{R_1} = 1$ and 4, respectively. The calculations were performed for Poisson's ratio $\nu = 0.28$.

Thus, the developed analytical and numerical procedures make it possible to efficiently study both the dynamic stress of thick plates with holes under the conditions of longitudinal vibrations and spectra of eigenfrequencies for various excitations.

REFERENCES

1. I. I. Vorovich and V. A. Babeshko, *Mixed Dynamic Problems of Elasticity Theory for Nonclassical Regions* (Nauka, Moscow, 1979).
2. V. I. Storozhev, Yu. V. Mysovskiĭ, and O. D. Sokolova, in *Theoretical and Applied Mechanics: Collection of Papers* (Osnova, Kharkov, 2003), No. 37, pp. 184–189.
3. L. A. Fil'shtinskiĭ, in *Theoretical and Applied Mechanics: Collection of Articles* (Osnova, Kharkov, 1990), No. 21, pp. 13–20.
4. S. M. Belotserkovskiĭ and I. K. Lifanov, *Numerical Methods in Singular Integral Equations* (Nauka, Moscow, 1985).

Translated by G. Merzon

Doklady Physics, Vol. 49, No. 8, 2004, pp. 483–487. Translated from Doklady Akademii Nauk, Vol. 397, No. 5, 2004, pp. 622–626.

MECHANICS

Averaging Algorithms and the Support-Operator Method for Poroelasticity Problems

Academician V. P. Myasnikov†, M. Yu. Zaslavsky, and A. Kh. Pergament

Received March 25, 2004

In this paper, we propose a mixed algorithm of solving uncoupled poroelasticity problems with double permeability and double porosity. An uncoupled poroelasticity problem breaks down into two different problems solved sequentially. The first one is a filtration problem with double permeability, which should be solved for an irregular-shaped collector. Then, an elasticity problem is considered, with the pore pressure gradient serving as a force source. Such a filtration problem is solved by the support-operator method on a curvilinear grid conforming to the medium structure. For solving the corresponding elasticity problem, we develop here an averaging method on grids nonconforming to discontinuity surfaces. As a result of the averaging of an isotropic medium, its elements having irregular internal structure can be described by an anisotropic model. In other words, the effective elastic modulus tensor is defined in such a way that the energy functional is exact for a certain class of functions. In order to define the elastic modulus tensor, we use specific basis functions describing medium properties. As a result, we succeed in constructing finite difference schemes whose conditionality on rectangular grids is better than that for schemes on grids conforming to the medium structure. We also present our test calculation results.

1. All natural layers are known to be fairly fractured media. Therefore, such fractured porous media are described by the filtration equation with double porosity and double permeability. Because the permeability of fractures is very high, pressure in them comes to a stable state more quickly than that in pores and, therefore, can be described by a quasistationary equation. Moreover, because the volume of fractures can be assumed to be negligible, the fluid content in fractures can be ignored. As a result, we come to a model that differs from the Biot model for porous media only by an equation for pressure in fractures if the generalization of Hooke's law in the Biot model remains valid. In what follows, we use the uncoupled version of the model proposed by Nikolaevskiĭ [3].

In the case of media with piecewise constant characteristics, projective methods (e.g., the finite element method and superelement method [4–7]) ensure the strong convergence of solutions of such problems and, hence, are most widespread.

However, both these methods use grids conforming to the medium structure. The poroelasticity problem is characterized by a number of scales, and the sizes of the porous collector are much smaller than the actual dimensions of the medium. Therefore, when solving the poroelasticity problem, one should use grids with cells larger than the characteristic sizes of the collector, with some cells having a fairly irregular structure. Therefore, it is necessary to evaluate average coefficients in such a cell so that the resulting mathematical model includes the properties of the original medium. In [1], we proposed an algorithm of averaging the elastic modulus tensor for stationary elasticity problems. The averaging algorithm is of particular interest for poroelasticity problems with sources caused by filtration processes.

In this paper, the averaging algorithm is constructed for the above problem and the convergence rate is estimated. We prove that the filtration problem is strongly convergent even in the case of piecewise constant coefficients and the corresponding elasticity problem is weakly convergent.

2. The mathematical model of a poroelasticity problem for fractured media describes the evolution of a stress–strain state and change in the pressures p_1 and p_2 in fractures and pores, respectively. In this case, permeability k_1 in fractures is assumed to be much greater than permeability k_2 in pores. The equations of the uncoupled model in a two-dimensional square domain Ω has the form

$$-\left(\frac{k_1}{\mu}p_{1,i}\right)_{,i} + \frac{\alpha}{\mu}(p_1 - p_2) = 0, \tag{1}$$

$$\beta\frac{\partial p_2}{\partial t} - \left(\frac{k_2}{\mu}p_{2,i}\right)_{,i} + \frac{\alpha}{\mu}(p_2 - p_1) = 0, \tag{2}$$

$$\sigma_{ij,j} = 0, \tag{3}$$

† Deceased.

Keldysh Institute of Applied Mathematics, Russian Academy of Sciences, Miusskaya pl. 4, Moscow, 125047 Russia

1028-3358/04/4908-0483$26.00

$$\sigma_{ij} = \Lambda_{ijkl}\epsilon_{kl} - \zeta p_2 \delta_{ij}, \quad (4)$$

$$\epsilon_{kl} = \frac{1}{2}(u_{k,l} + u_{l,k}). \quad (5)$$

The kinematic boundary condition $u|_{\Gamma'} = 0$ is imposed at the lower boundary Γ', and the free surface condition $\sigma_{ij}n_j|_{\Gamma''} = 0$ is imposed at the upper and lateral boundaries Γ''. The medium is assumed isotropic but inhomogeneous:

$$\Lambda_{ijkl} = \lambda\delta_{ij}\delta_{kl} + \mu(\delta_{ik}\delta_{jl} + \delta_{il}\delta_{jk}).$$

We assume that the Lamé coefficients are positive: $\mu > 0$ and $\lambda > 0$. In this case, filtration occurs in a fairly narrow domain Ω', and boundary conditions are imposed at its boundary.

We employ the support-operator method with adapted grids only in the domain Ω'. In the domain Ω, we use the averaging algorithm on a uniform rectangular grid. As was shown in [1], change in the description of the medium is a characteristic property of the averaging method. Indeed, small elements that include structural irregularities become anisotropic in this method.

In contrast to [1], we consider here elasticity equations with sources produced by pore pressure gradients having singularities at the boundaries between the collector and surrounding medium. Therefore, the basis functions described in [1] are insufficient to construct the averaging algorithms. It is necessary to find an approximate solution of the corresponding inhomogeneous problem whose singularities coincide with those of the exact solution.

3. In order to approximate the operator $\mathrm{div}(k\nabla p)$, where k is either $\frac{k_1}{\mu}$ or $\frac{k_2}{\mu}$ and p is either p_1 or p_2, we employ the support-operator method. In this method, the finite difference divergence and gradient operators

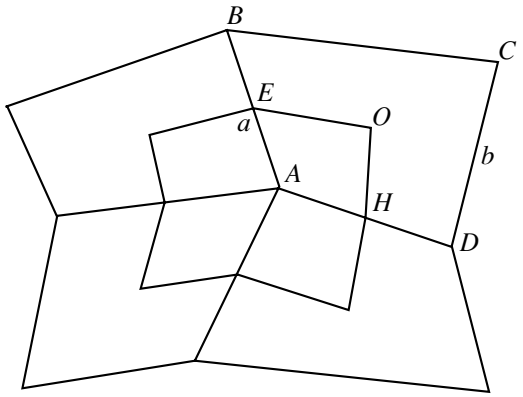

Fig. 1. Cells of a curvilinear grid.

are defined by using the finite-difference analogue of the well-known integral identity

$$\int_{\Omega'} k\nabla p\nabla r + \int_{\Omega'} r\,\mathrm{div}k\nabla p = \int_{\partial\Omega'} k\frac{\partial p}{\partial n}r. \quad (6)$$

This equality must be valid for arbitrary functions r, i.e., on explicitly defining one of these operators (referred to as a support operator), another operator is found as the operator conjugate to the former.

We assign the unknowns to the nodes of a rectangular grid M given in the domain Ω'. It is assumed that a positive direction on its edges is fixed and the coefficient k is constant in each cell. In this case, it is natural to take the gradient as the support operator. We approximate the first integral on the left-hand side of Eq. (6) by the sum $\sum_M g^{ab} Q_a S_b$ over all cells of the grid M. The summation is performed over all edges a and b of the grid. For the edges shown in Fig. 1,

$$Q_a = -p(B) + p(A), \quad S_b = r(C) + r(D).$$

For simplicity, we impose the zero-flux condition $\frac{\partial p_i}{\partial n} = 0$ ($i = 1, 2$) at the boundary of the domain Ω'. Approximating the second integral on the left-hand side of Eq. (6) by the expression

$$\sum_i V_i (\mathrm{div}(k\nabla p))_{h,i} r_i,$$

where the sum is taken over all nodes of the grid M, we find the difference operator div at the ith node: $(\mathrm{div}(k\nabla p))_{h,i} = \frac{\sigma_a Q^a}{V_i}$, where the summation is extended over the edges with one end coinciding with the ith node. Here, $\sigma_a = 1$ for the edges from the node i; otherwise, $\sigma_a = -1$ and $Q^a = g^{ab}Q_b$, where the summation is taken over the edges of all cells containing the edge a.

Let l_a be the vector directed along the positive direction on the edge a and its length be equal to the length of the edge. We then define

$$g^{ab} = k\sum_\phi S_\phi (l'_a; l'_b)_\phi$$

for each cell of the grid M. Here, the summation is extended over all nodes ϕ of the cell, $(l'_a; l'_b)_\phi$ is the Euclidean inner product of the vectors conjugate to the vectors l_a and l_b with the common node ϕ, and S_ϕ is an area associated with the node ϕ. For the cell $ABCD$ shown in Fig. 1, S_A is half the area of triangle ABD, S_B is half the area of triangle ABC, and so on.

Finally, we define area V_i associated with the ith node. To do this, each node ϕ of each cell of the grid M

is attributed by area V'_ϕ. In particular, V'_A is the area of the rectangular *AEOH* shown in Fig. 1, where *E* and *H* are the midpoints of the edges *AB* and *AD*, respectively, and *O* is the center of mass of the cell. Then, V_i is the sum of V'_i taken over all cells with the common node *i*.

The further approximation of the spatial operators of the filtration problem is evident. Because the problem under consideration involves both parabolic and elliptic equations, we employ implicit difference schemes.

4. An algorithm of solving elasticity problems without singular volume sources was presented in [1]. However, elasticity equations (3)–(5) include volume forces $\nabla(\zeta p_2)$ having δ-function singularities. Indeed, the quantity ζp_2 vanishes outside the collector but can be nonzero inside it. Such a problem is solved on a uniform rectangular grid $S = \{(ih_1;\ jh_2)\}_{i,j=1}^{N}$. The unknowns are referred to nodes.

We assume that discontinuity lines are smooth enough to be approximated inside each cell *H* by a straight line and that the Lamé coefficients vary locally along only one direction: $\lambda = \lambda(\mathbf{nr})$ and $\mu = \mu(\mathbf{nr})$. For elasticity problems that could involve fractures without their opening, the quantities $\sigma_{ij} n_j$ and $u_{i,j} m_j$ are continuous functions. Here, **n** and **m** are the unit normal and unit tangent vectors of a discontinuity line, respectively. Therefore, the displacements, as well as forces applied to an area tangent to the discontinuity line, are continuous functions. As a consequence, the corresponding distortion tensor components are also continuous functions. We will require that these quantities be smooth enough to be locally approximated by constants in a certain norm.

As is known, solutions obtained in the collector can be locally approximated by constants if k_1 and k_2 are piecewise continuous functions and ζ is constant in the collector. Therefore, the quantity ζp_2 inside each cell varies only along **n**.

For each cell *H*, we define the linear span

$$L(H) = \operatorname{span}\left\{ U^1 = \mathbf{m}\int_0^{\mathbf{nr}} \frac{ds}{\mu},\ U^2 = \mathbf{n}\int_0^{\mathbf{nr}} \frac{ds}{\lambda+2\mu},\right.$$

$$U^3 = \mathbf{m}(\mathbf{mr}) - \mathbf{n}\int_0^{\mathbf{nr}} \frac{\lambda ds}{\lambda+2\mu},$$

$$\left. U^4 = -\mathbf{m}(\mathbf{nr}) + \mathbf{n}(\mathbf{mr}),\quad U^5 = \mathbf{m},\quad U^6 = \mathbf{n} \right\}.$$

Due to the above assumptions, an exact solution of the inhomogeneous elasticity problem can be approximated inside the cell *H* by a vector of the manifold $M(H) = L(H) + \mathbf{f}$, where the vector

$$\mathbf{f} = \mathbf{n}\int_0^{\mathbf{nr}} \frac{\xi p_2 ds}{\lambda+2\mu}$$

is defined by the source entering into Eqs. (3)–(5).

Our goal is to approximate the integrals $\int_H \sigma_{ij}(U)\epsilon_{ij}(V)$ for each cell *H*. Indeed, using an equality similar to Eq. (6), we can find an approximation of σ_{ijj}. Let us approximate this integral by the expression $\sum_\phi V_\phi \sigma_{h,ij,\phi}(U)\epsilon_{h,ij,\phi}(V)$. Here, the sum is taken over all nodes of the cell *H* and $\epsilon_{h,ij,\phi}(V)$ is a strain-tensor approximation that depends on two finite differences at the node φ of the cell *H*:

$$\sigma_{h,ij,\phi}(H) = \Sigma^{H,\phi}_{ijkl}\epsilon_{h,kl,\phi}(U) - M^{H,\phi}_{ij},$$

where $\Sigma^{H,\phi}_{ijkl}$ is the effective elastic modulus tensor and $M^{H,\phi}_{ij}$ is the effective pressure tensor. Pressure is described by a tensor, because the Pascal law is not valid for anisotropic media.

In order to determine the six components of the effective elastic modulus tensor $\Sigma^{H,\phi}_{ijkl}$, we equate the continuous energy to the discrete energy for the vectors of $L(H)$ at the node φ of the cell *H*. Because U^5 and U^6 define the motion of the body as a whole and U^4 describes its rotation about the *z* axis, they correspond to zero strains. Therefore, we arrive at the six equations for the six components $\Sigma^{H,\phi}_{ijkl}$:

$$\int_H \Lambda_{ijkl}\epsilon_{ij}(U^\alpha)\epsilon_{kl}(U^\beta)dV = |H|\Sigma^{H,\varphi}_{ijkl}\epsilon_{h,ij,\phi}(U^\alpha)\epsilon_{h,kl,\phi}(U^\beta), \quad \alpha,\beta = 1,2,3. \tag{7}$$

The left-hand side of Eqs. (7) is the symmetric 3×3 matrix

$$\begin{pmatrix} \int_H \frac{dV}{\mu} & 0 & 0 \\ 0 & \int_H \frac{dV}{\lambda+2\mu} & 0 \\ 0 & 0 & \int_H \frac{4\mu(\lambda+\mu)dV}{\lambda+2\mu} \end{pmatrix}.$$

The effective pressure tensor is found from the equations

$$\int_H (\zeta p_2 \epsilon_{ii}(U^\alpha) - \Lambda_{ijkl}\epsilon_{ij}(\mathbf{f})\epsilon_{kl}(U^\alpha))$$

$$= |H|(M_{ij}^{H,\phi}\epsilon_{h,ij,\phi}(U^\alpha) - \Sigma_{ijkl}^{H,\phi}\epsilon_{h,ij,\phi}(\mathbf{f})\epsilon_{h,kl,\phi}(U^\alpha)).$$

The further procedure of calculating the approximation of the divergence of the stress tensor is evident.

5. We now analyze the convergence of the above algorithm. Let

$$p_i \in H^{L,1}\left(\frac{k_i}{\mu}, \Omega'\right), \quad (U;\ p_2) = (u_1, u_2;\ p_2) \in H^{L,2}(\Omega)$$

at arbitrary time, where

$$H^{L,1}(k, \Omega')$$

$$= \{p:\ p \in H^1(\Omega'), k p_{,j} n_j \in H^1(\Omega'), p_{,j} m_j \in H^1(\Omega')\},$$

$$H^{L,2}(\Omega)$$

$$= \{(U;\ p_2):\ u_i \in H^1(\Omega), \sigma_{ij} n_j \in H^1(\Omega), u_{i,j} m_j \in H^1(\Omega)\}.$$

These spaces are equipped with the norms

$$\|p\|^2_{H^{L,1}(k,\Omega)} = \|p\|^2_{H^1(\Omega')} + |p|^2_{H^{L,1}(k,\Omega')},$$

$$\|(U;\ p_2)\|^2_{H^{L,2}(\Omega)} = \|U\|^2_{H^1(\Omega)} + |(U;\ p_2)|^2_{H^L(\Omega)},$$

where

$$\|p\|^2_{H^1(\Omega')} = \int_{\Omega'} p^2 + \left(\frac{\partial p}{\partial x}\right)^2 + \left(\frac{\partial p}{\partial y}\right)^2,$$

$$|p|^2_{H^{L,1}(k,\Omega')} = \|p_{,j} m_j\|^2_{H^1(\Omega')} + \|k p_{,j} n_j\|^2_{H^1(\Omega')},$$

$$\|U\|^2_{H^1(\Omega)} = \|u_1\|^2_{H^1(\Omega)} + \|u_2\|^2_{H^1(\Omega)},$$

$$|(U;\ p_2)|^2_{H^{L,2}(\Omega)} = \|u_{i,j} m_j\|^2_{H^1(\Omega)} + \|\sigma_{ij} n_j\|^2_{H^1(\Omega)}.$$

It is assumed that a curvilinear coordinate system with unit vectors **m** and **n** tangent to its coordinate lines is specified in the whole domain, with discontinuities directed along the coordinate line orthogonal to **n**.

Let h_1 and h be characteristic scales of the grids in Ω' and Ω, respectively, and τ be a time step in the time interval $[0, T]$, where the problem is considered. We introduce the following finite difference analogues of the norm in $L_2(\Omega')$, the energy norm, and the energy inner product in Ω:

$$\|p_i\|^2_{L_2,h_1(\Omega')} = \sum_i V_i p^2(i),$$

$$\|p_i\|^2_{E_{h_1}(\Omega')} = \sum_M g^{ab}(\nabla p_i)_{h_1,a}(\nabla_{p_i})_{h_1,b},$$

$$(U, V)_\Sigma = \sum_H \sum_\phi V_\phi \Sigma_{ijkl}^{H,\phi}\epsilon_{h,kl,\phi}(V)\epsilon_{h,ij,\phi}(U).$$

Using these assumptions and notation, we can prove that the filtration problem is strongly convergent and the elasticity problem is weakly convergent.

Theorem. *Let p_i and $U = (u_1; u_2)$ be an exact solution of Eqs.* (1)–(5), *with $p_{2,tt} \in L_2(\Omega') \cap C[0; T]$ and for arbitrary t $p_i(t) \in H^{L,1}\left(\frac{k_i}{\mu}, \Omega'\right)$ and $U(t) \in H^{L,2}(\Omega)$. Let $p_{h_1,i}$ and U_h be a solution of the finite difference problem under consideration. Then, there exists a constant C such that, for all $(V; p_2) \in H^{L,2}(\Omega)$, the following estimates are valid:*

$$\max_t |(U - U_h, \delta V)_\Sigma| \le Ch \max_t (\|U;\ p_2\|_{H^{L,2}(\Omega)}$$

$$+ \|\zeta p_{h_1,2}(t = 0)\|_{H^1_{h_1}(\Omega')} \|(\delta V;\ 0)\|_{H^{L,2}(\Omega)},$$

$$\max_t \|p_1 - p_{h_1,1}\|_{L_{2,h_1}(\Omega')} \le Ch_1 \left(\max_t \|p_1\|_{H^{L,1}\left(\frac{k_1}{\mu}, \Omega'\right)}\right.$$

$$\left. + \max_t \|p_2\|_{H^{L,1}\left(\frac{k_2}{\mu}, \Omega'\right)}\right) + C\tau \max_t \|p_{2,tt}\|_{L_{2,h_1}(\Omega')},$$

$$\max_t \|p_2 - p_{h_1,2}\|_{L_{2,h_1}(\Omega')} \le Ch_1 \left(\max_t \|p_1\|_{H^{L,1}\left(\frac{k_1}{\mu}, \Omega'\right)}\right.$$

$$\left. + \max_t \|p_2\|_{H^{L,1}\left(\frac{k_2}{\mu}, \Omega'\right)}\right) + C\tau \max_t \|p_{2,tt}\|_{L_{2,h_1}(\Omega')}.$$

6. The above algorithm was extended to the three-dimensional case. The following problem was analyzed as a test. We considered a 10-km cube domain containing a τ-shaped collector with 6.25-km height and 0.25-km characteristic transverse dimension. The permeability coefficients in fractures and pores were 1.0 and 0.1 darcy, respectively. We take the following values of the parameters: compressibility $\beta = 2.5 \times 10^{-6}$ atm^{-1}, Lamé coefficients for the collector $\lambda_1 = 3.4 \times 10^{10}$ Pa and $\mu_1 = 1.33 \times 10^9$ Pa, those for the surrounding medium $\lambda_2 = 3.678 \times 10^{10}$ Pa and $\mu_2 = 1.292 \times$

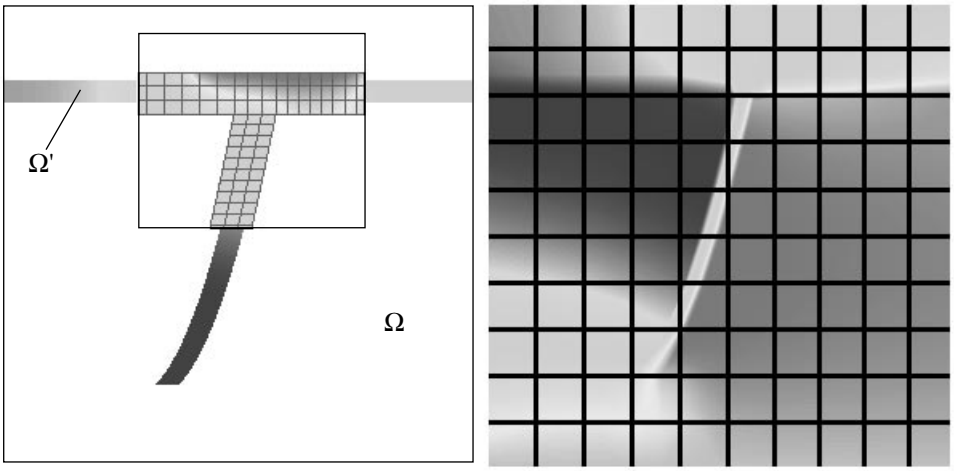

Fig. 2. Distributions of (left panel) p_2 and (right panel) u_x.

10^{10} Pa, coefficient $\alpha = 10^{-18}$ m^2, and viscosity $\mu = 0.0004$ Pa s. We imposed the geostatic initial conditions $p_1 = p_2 = 0$ and the zero-flux condition for p_1 and p_2 at the entire boundary, except for the upper section of the collector, where the flux for p_2 is given by the expression

$$25 \times 10^5\left(1 + 0.05\sin\left(2\pi\left(\frac{x}{1\text{ km}} - \frac{t}{10^6\text{ s}}\right)\right)\right)\text{ Pa},$$

for $\frac{x}{1\text{ km}} \in \left[\frac{t}{10^6\text{ s}}; 2\pi + \frac{t}{10^6\text{ s}}\right]$, and vanishes otherwise. Here, a kilometer and 10^6 seconds are taken as the units of distance and time, respectively.

The solution at $z = 5$ km and $t = 2$ months is illustrated in Fig. 2, where the distributions of (left panel) pressure in pores and (right panel) displacements along the x axis are shown.

Our calculations indicate that the flow along the descending branch of the collector is essentially one-dimensional and represents diffusion along the break. As was to be expected, displacements reach their maximum values near the boundaries and along the break. It is the interpolation by vectors from $M(H)$ inside cells that allows us to describe the break so precisely.

ACKNOWLEDGMENTS

This work was supported by the Russian Foundation for Basic Research, project no. 03-01-00641.

REFERENCES

1. V. P. Myasnikov, M. Yu. Zaslavskiĭ, and A. Kh. Pergament, Dokl. Akad. Nauk **394**, 332 (2004) [Dokl. Phys. **49**, 58 (2004)].
2. S. Moskow, V. Druskin, T. Habashy, *et al.*, SIAM (Soc. Ind. Appl. Math.) J. Numer. Anal. **36**, 442 (1999).
3. V. N. Nikolaevskiĭ, *Geomechanics and Fluid Dynamics* (Nedra, Moscow, 1996).
4. P. G. Ciarlet, *The Finite Element Method for Elliptic Problems* (North-Holland, Amsterdam, 1978; Mir, Moscow, 1980).
5. I. Babuska, G. Caloz, and J. E. Osborn, SIAM (Soc. Ind. Appl. Math.) J. Numer. Anal. **31**, 945 (1994).
6. R. P. Fedorenko, *Introduction to Computer Physics* (MFTI, Moscow, 1994).
7. V. T. Zhukov, N. D. Novikova, L. G. Strakhovskaya, *et al.*, Preprint No. 8, IPM im. Keldysha (Keldysh Institute of Applied Mathematics, Russian Academy of Sciences, Moscow, 2001).
8. A. A. Samarskiĭ, A. V. Koldoba, Yu. A. Poveshchenko, V. V. Tishkin, and A. P. Favorskiĭ, *Finite Difference Schemes on Irregular Grids* (Minsk, 1996).
9. A. V. Koldoba, A. Kh. Pergament, Yu. A. Poveshchenko, and N. A. Simus, Math. Model. **11** (10), 3 (1999).
10. O. A. Dremov, A. V. Koldoba, A. Kh. Pergament, *et al.*, Preprint No. 131, IPM im. Keldysha (Keldysh Institute of Applied Mathematics, Russian Academy of Sciences, Moscow, 1995).

Translated by V. Chechin

Doklady Physics, Vol. 49, No. 8, 2004, pp. 488–490. Translated from Doklady Akademii Nauk, Vol. 397, No. 6, 2004, pp. 772–775.

MECHANICS

Variational Method of Creep Theory with Allowance for Damaging and Corrosion

A. N. Alizade* and R. Yu. Amenzade**

Presented by Academician E.I. Shemyakin February 23, 2004

Received February 27, 2004

The problem of determining a stress–strain state in creep media with allowance for damaging and corrosion is attracting increasing attention of researchers. First, this is due to high requirements to the quality and reliability of metallic constructions or their individual elements under the conditions of long-term high-temperature loading and in aggressive environment [1, 2]. However, it is very difficult and sometimes even impossible to obtain analytical solutions due to mathematical problems associated with the need to solve nonlinear boundary value problems. Therefore, it is necessary to develop effective approximate methods of solution, including variational methods, and to apply them to such problems.

The viewpoint on variational methods in the mechanics of deformable solids has changed considerably in recent years. The possibilities of developing different variational principles, i.e., finding functionals for which the equations of a problem are Euler differential equations, turned out to be much wider than it previously seemed. The possibility of a rather free choice of independent functional arguments was revealed [3].

In this work, a mixed-type variational principle is formulated for creeping with simultaneous allowance for corrosion and damaging.

1. We assume that instantaneous elastoplastic strain ε_{ij}^M and creep strain p_{ij} simultaneously arise in a material such that the total strain is given by the formula

$$\varepsilon_{ij} = \varepsilon_{ij}^M + p_{ij} \text{ or } \dot{\varepsilon}_{ij} = \dot{\varepsilon}_{ij}^M + \dot{p}_{ij}.$$

In the three-dimensional Euclidean space with coordinates x^k, we consider an elastoplastic anisotropic medium that satisfies the flow-theory equations of state[1]

$$\dot{\varepsilon}_{ij}^M = H_{ijkl}\dot{\sigma}^{kl},$$

where $\dot{\varepsilon}_{ij}$ is the strain rate tensor, $\dot{\sigma}^{kl}$ is the stress rate tensor, and H_{ijkl} are mechanical characteristics independent of strain and stress rates. Thus, the total strain rate tensor is written as

$$\dot{\varepsilon}_{ij}^M = H_{ijkl}\dot{\sigma}^{kl} + \dot{p}_{ij}.$$

There are many variants for simulating processes of unsteady corrosion, long-term strength, and their correlations. Following Rabotnov [4], we have the relation

$$\dot{p}_{ij} = \dot{p}_{ij}(\varepsilon_{\alpha\beta}, \sigma^{\alpha\beta}, \omega, c),$$

the diffusion kinetic equation

$$\dot{c} = \operatorname{div}(D\nabla c)$$

and the damage kinetic equation

$$\dot{\omega} = \varphi(\sigma^{\alpha\beta}, \omega, c).$$

Here, ω is the damaging parameter, c is the parameter characterizing the concentration of an aggressive medium, and $D = D(\sigma^{\alpha\beta}, \omega, c)$ is the corrosion coefficient. We now consider the equilibrium of the described body (dynamic effects are assumed to be negligible) with volume V bounded by a rather smooth surface S. In geometrically linear theory, this body is described by the boundary value problem

$$\nabla_j\sigma^{ij} = 0, \tag{1}$$

$$\dot{\varepsilon}_{ij} = H_{ijkl}\dot{\sigma}^{kl} + \dot{p}_{ij}, \tag{2}$$

$$2\varepsilon_{ij} = \nabla_i u_j + \nabla_j u_i, \tag{3}$$

$$\bar{T}^i = \sigma^{ij}n_j, \quad \forall x^k \in S_\sigma, \tag{4}$$

$$\bar{u}_i = u_i, \quad \forall x^k \in S_u, \tag{5}$$

$$\dot{c} = \operatorname{div}(D\nabla c), \tag{6}$$

* *Azerbaijan Technical University, Hussein Javid av. 25, Baku, 370073 Azerbaijan*

** *Baku State University, Z. Khalilov st. 23, Baku, 370148 Azerbaijan*

[1] Hereinafter, the common accepted notation is used.

1028-3358/04/4908-0488$26.00

$$\dot{\omega} = \varphi(\sigma^{\alpha\beta}, \omega, c), \tag{7}$$

where $S = S_\sigma \cup S_u$. In terms of variational theorem, the problem under consideration is formulated as follows. The stationary value of the functional ($\delta J = 0$)

$$J = \int_V \left\{ \dot{\sigma}^{ij}\dot{\varepsilon}_{ij} - \frac{1}{2}(\dot{\varepsilon}_{ij}^M + 2\dot{p}_{ij})\dot{\sigma}^{ij} + \lambda_\omega\left(\frac{1}{2}\dot{\omega}^2 - \dot{\omega}\varphi\right) \right.$$

$$\left. + \lambda_c\left[\frac{1}{2}\dot{c}^2 - \dot{c}\,\mathrm{div}(D\nabla c)\right] \right\} dV \tag{8}$$

$$- \int_{S_\sigma} \dot{\bar{T}}^i \dot{u}_i dS - \int_{S_u} \dot{T}^i(\dot{u}_i - \dot{\bar{u}}_i) dS$$

under conditions (2) and (3) as Euler differential equations leads to equilibrium condition (1), boundary conditions (4) and (5), and kinetic equations (6) and (7). Here, $\dot{\sigma}^{ij}$, $\dot{u}^i$, $\dot{\omega}$, and $\dot{c}$ are independent varying quantities and $\lambda_\omega = \lambda_\omega(\sigma^{\alpha\beta}, \varepsilon_{\alpha\beta})$ and $\lambda_c = \lambda_c(\sigma^{\alpha\beta}, \varepsilon_{\alpha\beta})$ are weight functions selecting in dependence of the form of interpolation functions for the refinement of approximations. Functional (8) is based on both the variational principle by Sanders, McComb, and Schlechte in creep theory [4] and the variational theorem in creep theory including damaging [5]. Then, taking into account that the variation operator δ acts on the rates of the quantities and in view of Eq. (3) and equalities

$$H_{ijkl}\dot{\sigma}^{kl}\delta\dot{\sigma}^{ij} = H_{ijkl}\dot{\sigma}^{ij}\delta\dot{\sigma}^{kl},$$

$$\dot{\sigma}^{ij}\nabla_i\delta\dot{u}_j = \dot{\sigma}^{ij}\nabla_j\delta\dot{u}_i$$

we determine the first variation of the functional J in the form

$$\delta J = \int_V \{\dot{\sigma}^{ij}\nabla_j\delta\dot{u}_i + \dot{\varepsilon}_{ij}\delta\dot{\sigma}^{ij} - (H_{ijkl}\dot{\sigma}^{kl} + \dot{p}_{ij})\delta\dot{\sigma}^{ij}$$

$$+ \lambda_\omega(\dot{\omega} - \varphi)\delta\dot{\omega} + \lambda_c[\dot{c} - \mathrm{div}(D\nabla c)]\delta\dot{c}\}dV \tag{9}$$

$$- \int_{S_\sigma} \dot{\bar{T}}^i \delta\dot{u}_i dS - \int_{S_u} [(\dot{u}_i - \dot{\bar{u}}_i)\delta\dot{T}^i + \dot{T}^i\delta\dot{u}_i] dS.$$

Applying the divergence theorem, we represent the first term in the volume integral as

$$\int_V \dot{\sigma}^{ij}\nabla_j\delta\dot{u}_i dV = \int_S \dot{\sigma}^{ij}n_j\delta\dot{u}_i dS - \int_V \nabla_j\dot{\sigma}^{ij}\delta\dot{u}_i dV. \tag{10}$$

Substituting Eq. (10) into Eq. (9) and making certain manipulations, we rewrite the expression for δJ in the form

$$\delta J = \int_V \{[\dot{\varepsilon}_{ij} - (H_{ijkl}\dot{\sigma}^{kl} + \dot{p}_{ij})]\delta\dot{\sigma}^{ij} - \nabla_j\dot{\sigma}^{ij}\delta\dot{u}_i$$

$$+ \lambda_\omega(\dot{\omega} - \varphi)\delta\dot{\omega} + \lambda_c[\dot{c} - \mathrm{div}(D\nabla c)]\delta\dot{c}\}dV$$

$$+ \int_S \dot{\sigma}^{ij}n_j\delta\dot{u}_i dS - \int_{S_\sigma} \dot{\bar{T}}^i\delta\dot{u}_i dS - \int_{S_u} [\dot{T}^i\delta\dot{u}_i + (\dot{u}_i - \dot{\bar{u}}_i)\delta\dot{T}^i] dS.$$

Then, in view of boundary conditions (4) and (5), i.e., $\delta\dot{T}^i = 0$ for $x^k \in S_\sigma$ and $\delta\dot{u}^i = 0$ for $x^k \in S_u$, the first variation takes the final form

$$\delta J = \int_V \{[\dot{\varepsilon}_{ij} - (H_{ijkl}\dot{\sigma}^{kl} + \dot{p}_{ij})]\delta\dot{\sigma}^{ij} - \nabla_j\dot{\sigma}^{ij}\delta\dot{u}_i$$

$$+ \lambda_\omega(\dot{\omega} - \varphi)\delta\dot{\omega} + \lambda_c[\dot{c} - \mathrm{div}(D\nabla c)]\delta\dot{c}\}dV \tag{11}$$

$$- \int_{S_\sigma} (\dot{\bar{T}}^i - \dot{T}^i)\delta\dot{u}_i dS - \int_{S_u} (\dot{u}_i - \dot{\bar{u}}_i)\delta\dot{T}^i dS.$$

To find the stationary value of functional (8), variation (11) is equated to zero. Then, due to the fundamental lemma of variational calculus, we obtain Euler differential equations in the form

$$\nabla_j\dot{\sigma}^{ij} = 0, \tag{12}$$

$$\dot{\varepsilon}_{ij} = H_{ijkl}\dot{\sigma}^{kl} + \dot{p}_{ij}, \tag{13}$$

$$\dot{\omega} = \varphi, \tag{14}$$

$$\dot{c} = \mathrm{div}(D\nabla c), \tag{15}$$

$$\dot{\bar{T}}^i = \dot{T}^i, \quad \forall x^k \in S_\sigma, \tag{16}$$

$$\dot{\bar{u}}_i = \dot{u}_i, \quad \forall x^k \in S_u. \tag{17}$$

After the partial integration of Eqs. (12) with boundary conditions (16) and (17) with respect to t, we write

$$\nabla_j\sigma^{ij} = 0, \quad \dot{\varepsilon}_{ij} = H_{ijkl}\dot{\sigma}^{kl} + \dot{p}_{ij},$$

$$\dot{\omega} = \varphi, \quad \dot{c} = \mathrm{div}(D\nabla c),$$

$$\forall x^k \in V;$$

$$\bar{T}^i = T^i, \quad \forall x^k \in S_\sigma; \quad \bar{u}_i = u_i, \quad \forall x^k \in S_u.$$

The above statement follows from these relations. For the case of the chemically active medium, diffusion equation (15) takes the form

$$\dot{c} = \mathrm{div}(Dc) - kc,$$

where k = const is the characteristic rate of a chemical reaction and kc is the rate of the breaking of chemical bonds in the aggressive chemical medium. It is seen

that the last term of volume integral (8) in this variational formulation must be replaced by

$$\lambda_c\left[\frac{1}{2}\dot{c}^2 - \dot{c}\,\mathrm{div}(Dc) - kc\dot{c}\right].$$

We note that, to solve particular problems by, e.g., the Rayleigh–Ritz method, it is necessary to specify the initial condition for ω and the initial and corresponding boundary conditions with respect to c.

2. The mixed variational principle was proposed above in the geometrically linear formulation. However, in the problems of stability and swelling, it is insufficient to consider derivatives with respect to displacements to be small and to retain only linear terms in expressions for the strain tensor components in terms of displacements. It is necessary to take into account the finite strain tensor components given by the formulas

$$2\varepsilon_{ij} = (\nabla_i u_j + \nabla_j u_i + \nabla_i u^k \nabla_j u_k).$$

In this case, derivatives with respect to time are calculated as

$$2\dot{\varepsilon}_{ij} = (\nabla_i \dot{u}_j + \nabla_j \dot{u}_i + \nabla_i \dot{u}^k \nabla_j u_k + \nabla_i u^k \nabla_j \dot{u}_k),$$

and we arrive at the nonlinear equilibrium equations

$$\nabla_j S^{jk} = \nabla_j[\sigma^{ij}(\delta_i^k + \nabla_i u^k)] = 0 \qquad (18)$$

and the nonlinear boundary conditions

$$\bar{T}^k = \sigma^{ij} n_j(\delta_i^k + \nabla_i u^k) = S^{jk} n_j. \qquad (19)$$

In the above notation, the functional for geometrically nonlinear problems has the form

$$J = \int_V \left\{ \dot{\sigma}^{ij}\dot{\varepsilon}_{ij} + \frac{1}{2}\sigma^{ij}\nabla_i \dot{u}^k \nabla_j \dot{u}_k - \frac{1}{2}(\dot{\varepsilon}_{ij}^M + 2\dot{p}_{ij}) \right.$$

$$\left. + \lambda_\omega\left(\frac{1}{2}\dot{\omega}^2 - \dot{\omega}\varphi\right) + \lambda_c\left[\frac{1}{2}\dot{c}^2 - \dot{c}\,\mathrm{div}(Dc) - kc\dot{c}\right]\right\} dV \qquad (20)$$

$$- \int_{S_\sigma} \dot{\bar{T}}^i u_i dS - \int_{S_u} \dot{T}^i(\dot{u}_i - \dot{\bar{u}}_i) dS.$$

The proof that the condition of the zero variation of functional (20) is equivalent to the satisfaction of equilibrium equations (18), boundary conditions (19), constraints (2), and kinetic equations (6) and (7) is the same as the above proof. Additional terms in Eq. (20) do not involve stress change rates. Therefore, a difference is present only in the δJ part that corresponds to change in the velocity field. This part has the form

$$\delta J_1 = \int_V \left\{ \dot{\sigma}^{ij}\frac{1}{2}(\delta\nabla_i \dot{u}_j + \delta\nabla_j \dot{u}_i \right.$$

$$+ (\nabla_j u_k \delta\nabla_i \dot{u}^k + \nabla_i u^k \delta\nabla_j \dot{u}_k)$$

$$\left. + \frac{1}{2}\sigma^{ij}(\nabla_i \dot{u}^k \delta\nabla_j \dot{u}_k + \nabla_j \dot{u}_k \delta\nabla_i \dot{u}^k) \right\} dV$$

$$- \int_{S_\sigma} (\dot{\bar{T}}^i - \dot{T}^i)\delta\dot{u}_i dS.$$

Transforming volume integrals according to the divergence theorem, from the condition $\delta J_1 = 0$, we obtain

$$\nabla_j \dot{S}^{jk} = 0, \quad \dot{S}^{jk} n_j = \dot{T}^k \qquad (21)$$

or

$$\nabla_j S^{jk} = 0, \quad S^{jk} n_j = T^k.$$

The latter equations are obtained by integrating Eqs. (21) with respect to time.

When mass forces F^i are taken into account, the volume integral in functional (18) and (20) must be supplemented by $\dot{F}^i \dot{u}_i$ terms. In conclusion, we note that the proposed variational method can also be applied in the nonlinear theory of elasticity [6].

REFERENCES

1. *Properties of Creep and Long-Term Strength*, Ed. by S. A. Shesterikov (Mashinostroenie, Moscow, 1983).
2. A. M. Lokoshchenko, Usp. Mekh. **1** (4), 90 (2002).
3. Yu. N. Rabotnov, *Mechanics of Deformable Solids* (Nauka, Moscow, 1979).
4. Yu. P. Rabotnov, *Creep Behavior of Structural Elements* (Nauka, Moscow, 1966).
5. M. V. Sergeev, Izv. Akad. Nauk SSSR, Mekh. Tverd. Tela, No. 6, 112 (1982).
6. R. Yu. Amenzade, Dokl. Akad. Nauk **330**, 194 (1993) [Phys. Dokl. **38**, 200 (1993)].

Translated by R. Tyapaev